

Quantifying spatial uncertainties in structure-from-motion snow depth mapping with drones in an alpine environment

Dissertation

(kumulativ)

zur Erlangung des akademischen Grades
doctor rerum naturalium
(Dr. rer. nat.)

vorgelegt dem Rat der Chemisch-Geowissenschaftlichen Fakultät der
Friedrich-Schiller-Universität Jena

von **Jason Goetz, MSc**
geboren am 25. April 1985 in Kanada

Dissertation, Friedrich-Schiller-Universität Jena, 2019

Gutachter:

1. Prof. Dr. Alexander Brenning, Friedrich-Schiller-Universität Jena
2. PD. Dr. Christian Thiel, Deutsches Zentrum für Luft- und Raumfahrt (DLR)
3. Prof. Dr. Bernhard Höfle, Universität Heidelberg

Tag der Verteidigung: 4. Dezember 2019

Selbständigkeitserklärung

Ich erkläre, dass ich die vorliegende Arbeit selbständig und unter Verwendung der angegebenen Hilfsmittel, persönlichen Mitteilungen und Quellen angefertigt habe.

Ort, Datum

Unterschrift der Verfasserin/des Verfassers

Declaration on authorship and copyright in a cumulative doctoral thesis

Reprint permissions have been obtained for all manuscripts used as a part of the doctoral thesis.

The co-authors of the manuscripts used in the present cumulative doctoral thesis have been informed about the use of the manuscripts and about the declared individual contributions; they have given their consent.

The declared individual contributions of the doctoral candidate and the other doctoral candidates participate as co-authors in the publications are listed in the attachment.

Jason Goetz

Name of doctoral candidate	Date	Place	Signature
----------------------------	------	-------	-----------

I give my consent to the submission of a cumulative doctoral thesis and confirm the correctness of the information provided above.

Prof. Dr. Alexander Brenning

Name of supervisor	Date	Place	Signature
--------------------	------	-------	-----------

Declaration on authorship and copyright in a cumulative doctoral thesis

Publication #1:						
<p>Goetz, J., Brenning, A., Marcer, M., & Bodin, X. (2018). Modelling the precision of structure-from-motion multi-view stereo digital elevation models from repeated close-range aerial surveys. <i>Remote Sensing of Environment</i>, 210, 208-216.</p>						
Status: Published manuscript						
Involved in						
	Jason Goetz	Alexander Brenning	Marco Marcer	Xavier Bodin		
Conceptual research design	X	X				
Planning of research activities	X	X	X	X		
Data collection	X		X	X		
Data analysis and interpretation	X					
Manuscript writing	X	X				
Suggested publication equivalence value	1.0					

Publication #2:						
<p>Goetz, J., & Brenning, A. (2019). Quantifying uncertainties in snow depth mapping from structure-from-motion photogrammetry in an alpine area. <i>Water Resources Research</i>, 2019WR025251.</p>						
Status: Submitted manuscript (Water Resources Research, 29 March 2019)						
Involved in						
	Jason Goetz	Alexander Brenning				
Conceptual research design	X	X				
Planning of research activities	X					
Data collection	X					
Data analysis and interpretation	X					
Manuscript writing	X	X				
Suggested publication equivalence value	1.0					

Publication #3:

Goetz, J., Fieguth, P., Kasiri, K., Bodin, X., Marcer, M., & Brenning, A. (2019). Accounting for permafrost creep in high-resolution snow depth mapping by modelling sub-snow ground deformation. *Remote Sensing of Environment*, 231, 111275.

Status: Published manuscript

Involved in						
	Jason Goetz	Paul Fieguth	Keyvan Kasiri	Xavier Bodin	Marco Marcer	Alexander Brenning
Conceptual research design	X	X	X			X
Planning of research activities	X	X	X	X	X	
Data collection	X			X	X	
Data analysis and interpretation	X					
Manuscript writing	X					X
Suggested publication equivalence value	1.0					

Acknowledgements

There are many people who have helped get me here, who I want to thank.

I would first like to express my gratitude to Prof. Dr. Alexander Brenning. Alex, you have always encouraged me to push the limits of my knowledge, supported me in exploring my own ideas and have provided me with opportunities to explore the world. I have enjoyed the many years of our work together. Thank you.

I thank my geomorphology team in France, Dr. Xavier Bodin and Marco Marcer. Xavier, you and Alex got me hooked-on mountain research. I also thank you for your continuous support throughout this thesis. Marco, I could not have asked for a better a person to work with in the field. Thank you for all your help.

Thanks to Dr. Paul Fieguth and Dr. Keyvan Kasiri for introducing me to the world of image registration. Our collaboration led me to explore new and exciting technologies for monitoring changes in mountain geomorphology. Also thank you for teaching me the importance of carefully defining a problem.

Thank you to Dr. Richard Kelly for your long-time guidance, encouragement and support of my academic ventures. Your teaching while I was a bachelor student got me excited for remote sensing of snow.

I would like to thank our GIScience Team in Jena. Helene Goetz, Yanjun Shen, Patrick Schratz, Franziska Zander, José Cortés, Sven Kralisch, Bettina Böhm, Manfred Fink, Raphael Knevels, Jannes Münchow, Marco Peña, Sophie Biskop, Annika Künne, Markus Meinhardt, Miga Magenika Julian, Juliana Santos and Anita Martin, you provided support, guidance, inspiration, simply gave an ear to listen when it was needed and made it fun to study in Jena. Thank you everyone.

This research was done with the funding support of the Natural Sciences and Engineering Research Council of Canada, Carl Zeiss Foundation, Friedrich Schiller University Jena and Erasmus Plus.

Dedication

To my wife Helene, son Jonas, mom Cindy, dad Nick, Erin, Jon, Chris, and the rest of my family, friends, and the teachers that I have had along the way.

Thank you for all your love, encouragement and support over the years.

Abstract

Quantifying spatial uncertainties in structure-from-motion snow depth mapping with drones in an alpine environment

Due to the heterogeneous nature of alpine snow distribution, advances in hydrological monitoring and forecasting for water resource management require an increase in the frequency, spatial resolution and coverage of field observations. Such detailed snow information is also needed to foster advances in our understanding of how snowpack affects ecology and geomorphology including the occurrence of natural hazards. Recently, the use of structure-from-motion multi-view stereo (SFM-MVS) 3D reconstruction techniques have shown promising potential to provide higher spatial and temporal resolution snow depth data for snowpack monitoring. The combination of SFM-MVS with images collected from unmanned aerial vehicles (UAVs), or commonly known as drones, seems to be emerging as a cost-effective approach for snow depth mapping compared to traditional surveying techniques such as airborne light detection and ranging (lidar).

Much of the recent research exploring how SFM-MVS snow depth mapping performs compared to traditional techniques has illustrated that although it can provide similar results as the other measurement techniques, there remain challenges to produce high-quality snow depth data. These challenges, which include differentiating observations from noise and overcoming biases in the elevation data, are inherent in digital elevation model (DEM) differencing. A key issue to address these challenges is our ability to quantify measurement uncertainties in the SFM-MVS snow depths. Furthermore, a detailed understanding of the uncertainties is required to determine the limits and suitability of SFM-MVS mapping for specific applications. The aim of this thesis is to enhance our understanding of the spatial uncertainties in high-resolution (≤ 10 cm) mapping of snow depth using SFM-MVS and drones. It is comprised of three main contributions that focus on developing methods for spatially quantifying, characterizing and reducing uncertainties in SFM-MVS snow depth mapping using a case study at the Combe de Laurichard, located in the southern French Alps.

To understand the quality of SFM-MVS snow depth measurements, the uncertainty in the individual DEMs needs to be described. In the first part of this work, several models to define the spatial distribution of DEM error depending on the available validation data were presented. These models were based on three scenarios: (1) having a single DEM and check points or a reference DEM; (2) having multiple DEMs from repeat observations and check points; and (3) having multiple DEMs from repeat observations and a reference DEM. Additionally, the spatial uncertainty in SFM-MVS DEMs was quantified using in-situ field measurements and repeated drone surveys. The multiple elevation models were used to estimate the precision for each grid cell of the DEMs. To determine the effect of survey and field conditions on DEM quality, a generalized additive model (GAM) was applied to model the precision of the SFM-MVS derived elevations. Overall, by accounting for the effects of multiple variables using the GAM, it was found that the image height above the ground,

ground control network and image overlap have the strongest effect on the spatial distribution of DEM precision, respectively. Field site conditions, such as slope angle, and shading were only slightly important for spatially modelling precision.

In the second part of this work, a new method for quantifying and visualizing SFM-MVS snow depth uncertainties from DEM differencing was illustrated. Spatially varying snow depth precision, which was estimated from repeated drone surveys of the snow-free and snow-covered DEMs, was determined using an error propagation model that was applied to each grid cell. This error propagation model was used to express uncertainty with spatially varying detection limits for a given confidence level using a Student's t distribution. It was found for the given flying height (~60 m above ground level), camera and survey design that snow depths as shallow as 1 cm to 5 cm could be detected with high confidence for most of the study area. Areas of high uncertainties were generally related to where the extent of the GCP coverage did not match, and in areas with high surface roughness. Applying the detection limits as thresholds was found to be a useful approach for identifying potential biases in the snow depths; for example, errors due to poor SFM-MVS reconstruction and changes in topography between DEM acquisition dates could be observed.

This work additionally explored the effect of spatial resolution on snow depth errors. It was found for this study area, that the snow depth errors were more sensitive to the spatial resolution of the snow-free DEM than the snow-covered DEM. Errors related to poorer spatial resolution of the snow-cover DEM tended to only increase for resolutions coarser than 5 m. This result indicates the need for highly detailed surveying of the snow-free conditions in complex alpine terrain to minimize snow depth errors.

In the third part of this work, a method for correcting snow depth errors caused by changes occurring to the surface topography in the time between the acquisitions of the DEMs is presented. Using a case study of mapping snow depth over an active rock glacier, a novel method for kinematic modelling of surface displacements using an open-source solution for non-rigid registration is applied to DEMs, scaled and then used to transform the snow-free DEM to represent the sub-snow ground conditions at the time of the snow-covered DEM. In-situ snow depth measurements, and snow-free areas (e.g. rock debris and boulders) were used to constrain the transformation and to account for seasonal variations in displacement rates of permafrost creep. It was found that on-going slope deformation processes can be a considerable source of error in high-resolution snow-depth mapping, and that the applied method was able to reduce snow depth errors up to 33%.

Performing a detailed error analysis is essential for providing strong support for the quality of snow depth data or any corresponding geoscientific analysis based on SFM-MVS DEMs. The work in this thesis has developed a framework for conducting quality assurance of SFM-MVS DEMs based on repeated drone surveys and non-linear regression modelling. Also, since the repeated-based spatial uncertainty method can be applied to any SFM-MVS solution, it provides a standardized approach to benchmark the performance of SFM-MVS algorithms.

The spatial distribution of uncertainties can result from the SFM-MVS survey design and random sub-procedures in the SFM-MVS processing. Therefore, as illustrated in this thesis, applying the Student's t distribution to SFM-MVS DEM precision estimates is an effective

approach for determining if SFM-MVS snow depths are real observations or measurement errors. The work in this thesis was also the first to combine uncertainties in both the snow-free and snow-covered SFM-MVS DEMs to quantify the spatial distribution of SFM-MVS snow depth uncertainties. This analysis shows how uncertainties in SFM-MVS snow depths can be highly spatially heterogeneous. However, given a strong image and ground control network, the distribution of these uncertainties can be controlled. Furthermore, by modelling hillslope deformation processes, errors in high-resolution snow depths can be reduced.

Overall, this thesis contributes to the growing support of SFM-MVS combined with imagery acquired from drones as a suitable surveying technique for local scale snow distribution monitoring. Future work can focus on the application of SFM-MVS snow depth data for modelling local snow conditions, for example, by fusing data with numerical snowpack models. The error propagation technique, as presented in this thesis, can be applied to ensure the quality of snow depth data. This thesis also illustrated how characterizing factors influencing uncertainties in SFM-MVS DEMs can be used to improve SFM-MVS snow depth mapping. Further advances using this technique will likely result from benchmarking SFM-MVS algorithms for optimal performance under different snow cover conditions.

Zusammenfassung der Dissertation

Quantifizierung der räumlichen Unsicherheiten der Schneedeckenhöhenkartierung mittels Structure-from-Motion mit Drohnen Daten in einem alpinen Gebiet

Besonders aufgrund der hohen Heterogenität der alpinen Schneeverteilung ist eine Steigerung der Frequenz, der räumlichen Auflösung und der Abdeckung von Geländebeobachtungen notwendig, um Fortschritte im hydrologischen Monitoring und daraus abgeleiteten Vorhersagen für verbessertes Wasserressourcenmanagement zu erreichen. Detaillierte Informationen zur Schneedeckenhöhe bieten neue Anhaltspunkte zur Analyse und zum besseren Verständnis der Effekte der Schneedecke auf die lokale Ökologie und Geomorphologie, inklusive dem Auftreten von Naturgefahren. In den letzten Jahren haben Studien ein hohes Potential der Structure-from-Motion (SFM) multi-view stereo (MVS) 3D Rekonstruktion als Datenquelle zur Ermittlung der Schneedeckenhöhe mit höherer räumlicher und zeitlicher Auflösung für das Schneedecken-Monitoring gezeigt. Im Vergleich zu traditionelleren Vermessungsmethoden (wie z.B. flugzeuggestütztes Laserscanning (lidar)) entwickelt sich die Kombination von SFM-MVS Methoden angewandt auf Bildern, die mit unbemannten Flugsystemen, oder kurz oft auch Drohnen genannt, aufgenommen wurden, zu einem kosteneffizienten Ansatz.

Jüngste Studien, die SFM-MVS Schneedeckenhöhenkartierung mit traditionellen Methoden vergleichen, zeigten, dass die Ergebnisse zwar vergleichbar sind, aber dass immer noch Herausforderungen bezüglich der Erstellung von hoch qualitativen Schneedeckenhöhendaten mittels der neuen Methoden bestehen. Diese Herausforderungen sind inhärent im Bereich der Differenzbildung von digitalen Höhenmodellen (DHM) und liegen im Bereich der Unterscheidung von Signal (tatsächliche Schneedeckenhöhe) und Rauschen (Artefakt der DHM). Um diesen Herausforderungen zu begegnen ist es von großer Bedeutung Messunsicherheiten der SFM-MVS Schneehöhenkartierung quantifizieren zu können. Zusätzlich, ist ein detailliertes Verständnis der Unsicherheiten notwendig, um die Limitierungen und Eignung der SFM-MVS Kartierung für spezifische Anwendungen abschätzen zu können. Die Zielsetzung der vorliegenden Dissertation ist das Verbessern unseres Verständnisses der räumlichen Unsicherheiten in hoch aufgelösten (<10 cm) Schneedeckenhöhenkartierungen mittels SFM-MVS von Drohnenbildern. In dieser Dissertation wurden drei Teilbereiche dieser Problematik genauer bearbeitet, um neue Methoden für die räumliche Quantifizierung, Charakterisierung und Reduktion von Unsicherheiten in SFM-MVS Schneedeckenhöhenkartierungen zu entwickeln. Diese Methoden wurden am Beispiel des alpinen Untersuchungsgebiets Combe de Laurichard, in den südlichen französischen Alpen entwickelt und getestet.

Der erste Teil dieser Dissertation widmete sich der besseren Beschreibung der Unsicherheiten der einzelnen DHM die zur Berechnung der Schneehöhe herangezogen werden, um die Qualität der SFM-MVS Schneehöhenkartierung besser verstehen zu können. Mehrere Modelle

wurden zur Beschreibung der räumlichen Verteilung von Fehlern der entsprechenden DHM, abhängig von den verfügbaren Validierungsdaten erstellt. Diese Modelle basierten auf drei Szenarien: (1) ein einzelnes DHM und vermessene Punkte (mittels GNSS) oder ein Referenz DHM (z.B. aus lidar Daten) ist verfügbar; (2) mehrere DHM aus wiederholten Drohnenbefliegungen am selben Tag und vermessene Punkte sind verfügbar; und (3) mehrere DHM aus wiederholten Drohnenbefliegungen am selben Tag und ein Referenz DHM sind verfügbar. Zusätzlich wurde die räumliche Unsicherheit der SFM-MVS DHM der verschiedenen Zeitpunkte (schneebedeckt und schneefrei) mittels dem Vergleich der vermessenen Punkte und den wiederholten Drohnenbefliegungen am selben Tag quantifiziert. Die Abweichungen zwischen den DHM aus wiederholten Drohnenbefliegungen am selben Tag wurden verwendet um die Präzision der Höhe in jeder einzelnen Rasterzelle des entsprechenden DHM zu schätzen. Der Einfluss der Vermessungsmethode und der Geländebedingungen auf die DHM Qualität wurde mittels eines generalisierten additiven Modells (GAM) abgeschätzt. Das GAM wurde verwendet, um die Präzision der mittels SFM-MVS abgeleiteten Geländehöhen zu modellieren. Während mittels dem GAM die Effekte von vielen Variablen berücksichtigt wurden, wurde für die Höhe aus der das Bild aufgenommen wurde, die Verteilung der Passpunkte im Untersuchungsgebiet und das Ausmaß der Überlappung zwischen den einzelnen Bildern der größte Einfluss auf die räumliche Verteilung der Präzision des DHM festgestellt. Geländebedingungen wie Hangneigung und Schattenwurf hatten nur wenig Einfluss auf die räumliche Verteilung der Präzision des DHM.

Im zweiten Teil dieser Dissertation, wurde eine neue Methode zur Quantifizierung und Visualisierung von Unsicherheiten der SFM-MVS Schneedeckenhöhenkartierung basierend auf der Differenzbildung von zwei DHM entwickelt. Die räumlich variable Präzision der Schneedeckenhöhe, welche auf Schätzungen aus den wiederholten Drohnenbefliegungen während schneefreien und schneebedeckten Bedingungen basiert, wurde durch ein auf jede Rasterzelle angewendetes Modell der Fehlerfortpflanzung bestimmt. Dieses Modell der Fehlerfortpflanzung wurde verwendet um Unsicherheiten mit räumlich variablen Erfassungsgrenzen innerhalb eines gegebenen Konfidenzintervalls mittels der Student's t Verteilung zu beschreiben. Für die gegebene Flughöhe (~ 60 m über dem Boden), Kameraeigenschaften und das Vermessungsdesign wurde festgestellt, dass Schneehöhen von nur 1 cm bis 5 cm für den größten Teil des Untersuchungsgebiets mit hoher Konfidenz erfasst werden konnten. Bereiche mit hohen Unsicherheiten hingen im Allgemeinen mit dem Ausmaß der Passpunkt-Abdeckung und mit Bereichen mit hoher Oberflächenrauheit zusammen. Die Anwendung der ermittelten Erfassungsgrenzen als Schwellenwerte erwies sich als nützlicher Ansatz zur Identifizierung potenzieller Verzerrungen in den Schneehöhen. Beispielsweise konnten Fehler aufgrund einer schlechten SFM-MVS-Rekonstruktion und Änderungen der Topographie zwischen den DHM-Erfassungsterminen beobachtet werden.

In dieser Arbeit wurde zusätzlich der Effekt der räumlichen Auflösung auf Schneehöhenfehler untersucht. Für dieses Untersuchungsgebiet wurde festgestellt, dass die Schneehöhenfehler empfindlicher auf die räumliche Auflösung des schneefreien DHM reagieren als auf die räumliche Auflösung des schneebedeckten DHM. Fehler in Bezug auf eine schlechtere räumliche Auflösung des schneebedeckten DHM nahmen nur bei Auflösungen zu, die größer als 5 m waren. Dieses Ergebnis zeigt, dass die schneefreien Bedingungen in komplexem

alpinem Gelände sehr detailliert untersucht werden müssen, um Schneehöhenfehler zu minimieren.

Im dritten Teil dieser Arbeit wird eine Methode zur Korrektur von Schneehöhenfehlern vorgestellt, die durch Änderungen der Oberflächentopographie in der Zeit zwischen den Erfassungszeitpunkten der DHM verursacht werden. Anhand einer Fallstudie zur Kartierung der Schneehöhe über einem aktiven Blockgletscher wird eine neuartige Methode zur kinematischen Modellierung von Oberflächenverschiebungen unter Verwendung einer Open-Source-Lösung zur Bildregistrierung mittels elastischer Modelle (non-rigid image registration) auf digitale Geländemodelle angewendet, skaliert und dann zur Transformation des schneefreien DHM verwendet, um die Darstellung der Untergrundverhältnisse zum Zeitpunkt des schneebedeckten DHM zu generieren. In-situ-Schneehöhenmessungen und schneefreie Bereiche (z. B. Gesteinsschutt und Felsbrocken) wurden verwendet, um die Transformation zu begrenzen und saisonale Schwankungen der Bewegungsmuster und -raten des Permafrostkriechens zu berücksichtigen. Es wurde festgestellt, dass fortlaufende Hangdeformationsprozesse eine erhebliche Fehlerquelle bei der hochauflösenden Schneehöhenkartierung darstellen können und dass mit der angewendeten Methode Schneehöhenfehler um bis zu 33% reduziert werden können.

Eine detaillierte Fehleranalyse ist unerlässlich, um die Qualität der Schneehöhendaten oder eine entsprechende geowissenschaftliche Analyse auf der Grundlage von SFM-MVS-DHM zu gewährleisten. In der vorliegenden Arbeit wurde ein Rahmenwerk für die Qualitätssicherung von SFM-MVS-DHMs entwickelt, das auf Bildaufnahmen aus wiederholten Drohnenbefliegungen und nichtlinearen Regressionsmodellen basiert. Da die Methode zur Ermittlung der räumlichen Unsicherheit basierend auf wiederholten Drohnenbefliegungen auf jede SFM-MVS-Lösung angewendet werden kann, bietet diese neue Methode einen standardisierten Ansatz für das Benchmarking der Leistung von verschiedenen SFM-MVS-Algorithmen.

Die räumliche Verteilung von Unsicherheiten kann sich aus dem SFM-MVS Vermessungsdesign und zufälligen Unterprozeduren in der SFM-MVS-Prozessierung ergeben. Wie in dieser Arbeit gezeigt, ist die Anwendung der Student-t-Verteilung auf SFM-MVS-DHM Präzisionsschätzungen daher ein wirksamer Ansatz, um festzustellen, ob es sich bei SFM-MVS Schneehöhen um echte Beobachtungen oder Messfehler handelt. Mit dieser Arbeit wurden auch zum ersten Mal die Unsicherheiten sowohl in den schneefreien als auch in den schneebedeckten SFM-MVS-DEMs kombiniert, um die räumliche Verteilung der Unsicherheiten in SFM-MVS Schneehöhen zu quantifizieren. Diese Analyse zeigt, wie Unsicherheiten in SFM-MVS-Schneehöhen räumlich sehr heterogen sein können. Über gut verteilte Passpunkte und eine gute Überlappung der Drohnenbilder kann jedoch die Verteilung dieser Unsicherheiten gut kontrolliert werden. Darüber hinaus können durch die Modellierung von Deformationsprozessen der Topographie (wie z.B. Permafrostkriechen) mittels elastischer Bildregistrierungsmodelle Fehler in hochauflösenden Schneehöhen reduziert werden.

Insgesamt trägt diese Arbeit zur wachsenden Unterstützung von SFM-MVS von Drohnenbildern als geeignete Vermessungstechnik für die Kartierung und Überwachung der

Schneeverteilung im lokalen Maßstab bei. Zukünftige Arbeiten können sich auf die Anwendung von SFM-MVS-Schneehöhendaten zur Modellierung lokaler Schneebedingungen konzentrieren, beispielsweise durch Zusammenführen von Daten mit numerischen Schneedeckenmodellen. Die in dieser Arbeit vorgestellte Methode Berücksichtigung von Fehlerfortpflanzung in den DHM kann angewendet werden, um die Qualität der Schneehöhen-Daten sicherzustellen. Diese Arbeit zeigte auch, wie charakteristische Faktoren, welche die Unsicherheiten in SFM-MVS-DHMs beeinflussen, zur Verbesserung der SFM-MVS-Schneehöhenkartierung verwendet werden können. Weitere Fortschritte bei der Verwendung dieser Technik werden wahrscheinlich aus dem Benchmarking von verschiedenen SFM-MVS-Algorithmen für eine optimale Leistung unter verschiedenen Schneebedeckungsbedingungen resultieren.

Contents

Acknowledgements.....	i
Abstract.....	iii
Contents	xi
List of Figures.....	xv
List of Tables	xviii
List of Acronyms.....	xx
List of Symbols	xxi

Chapter 1

General introduction	1
1.1 Motivation	1
1.2 Research objectives.....	3
1.3 Thesis outline	4

Chapter 2

Structure-from-motion multi-view stereo 3D reconstruction.....	6
2.1 Introduction.....	6
2.2 Structure from motion	6
2.3 Multi-view stereo.....	8
2.4 Georeferencing.....	8
2.4.1 Artificial ground control points.....	9
2.4.2 Direct georeferencing.....	10
2.5 Reconstruction quality	10
2.5.1 Image and network quality	11
2.5.2 The ‘doming’ effect.....	12
2.6 SFM-MVS applied for snow depth mapping	13

Chapter 3

Modelling the precision of structure-from-motion multi-view stereo digital elevation models from repeated close-range aerial surveys	15
Abstract.....	15
3.1 Introduction.....	15
3.1.1 Describing DEM measurement error.....	16

3.1.2	Single DEM with check points or a reference DEM	18
3.1.3	Multiple DEMs from repeat aerial surveys with check points	19
3.1.4	Multiple DEMs from repeat aerial surveys with a reference DEM.....	20
3.2	Data and methods	20
3.2.1	Study site and elevation surveys.....	20
3.2.2	DEM processing and error estimation.....	22
3.2.3	Modelling the spatial distribution of precision.....	22
3.3	Results	23
3.3.1	Spatial variation in precision	23
3.3.2	Estimated error	26
3.4	Discussion.....	27
3.4.1	Spatial variation in precision	27
3.4.2	Investigating measurement bias.....	29
3.5	Conclusion.....	29
3.6	Acknowledgements.....	30

Chapter 4

Quantifying uncertainties in snow depth mapping from structure-from-motion photogrammetry in an alpine area	31
Abstract.....	31
4.1 Introduction.....	31
4.2 Materials and Methods	33
4.2.1 Study site and data collection	33
4.2.2 DEM processing and computing snow depths	35
4.2.3 Mapping snow depth uncertainties	36
4.2.4 DEM resolution and snow depth accuracy	36
4.3 Results	37
4.3.1 DEM accuracy and precision	37
4.3.2 SFM-MVS snow depth uncertainty.....	38
4.3.3 Snow depth accuracy and spatial resolution.....	40
4.4 Discussion.....	41
4.4.1 Mapping snow depth uncertainties	41
4.4.2 Reducing SFM-MVS snow depth uncertainties	42
4.4.3 The effects of spatial resolution on snow depth accuracy	43

4.5	Conclusions	43
4.6	Acknowledgements.....	44

Chapter 5

Accounting for permafrost creep in high-resolution snow depth mapping by modelling sub-snow ground deformation		45
	Abstract	45
5.1	Introduction.....	46
5.2	Methods	48
5.2.1	Study site and data	48
5.2.2	Mapping snow depth from DEMs	50
5.2.3	Finding an optimal scale factor	51
5.2.4	Modelling surface deformation	52
5.2.5	Applying sub-snow topography estimates.....	53
5.2.6	Error analysis	54
5.3	Results	55
5.3.1	Mapped surface deformations.....	55
5.3.2	Optimal scale factors.....	56
5.3.3	Performance of estimated DEMs.....	56
5.4	Discussion.....	62
5.4.1	Performance of the deformation model	62
5.4.2	Finding the optimal the scale factor.....	63
5.4.3	Snow depth errors	64
5.5	Conclusion.....	65
5.6	Acknowledgements.....	65

Chapter 6

General discussion and conclusions.....		66
6.1	Uncertainties in SFM-MVS DEMs.....	66
6.1.1	Characterizing SFM-MVS DEM error.....	68
6.1.2	Uncertainties in SFM-MVS reconstruction of snow-covered surfaces.....	69
6.2	Quantifying SFM-MVS snow depth uncertainties.....	70
6.2.1	Spatially varying snow depth uncertainty.....	71
6.2.2	Co-registration errors.....	71
6.2.3	SFM-MVS DEM spatial resolution.....	72

6.2.4	Errors from vegetation.....	72
6.3	Correcting SFM-MVS snow depths in active alpine terrain.....	73
6.3.1	In-situ measurements to constrain snow depth corrections.....	75
6.4	Future work.....	75
6.4.1	Benchmarking SFM-MVS algorithms.....	75
6.4.2	Applying SFM-MVS snow depths for snow modelling.....	76
6.5	Conclusions.....	76
References.....		79
Appendix.....		88
	Detailed UAV flight and SFM-MVS processing information.....	88
	Overview of digital elevation model registration settings.....	90

List of Figures

Figure 1. Location of the surveyed rock glacier in the Combe de Laurichard catchment including the extent of the study area and position of ground control points (i.e. artificial targets). The background topographic data is a hillshaded DEM derived from a terrestrial lidar survey performed in 2012 (data courtesy of *Station Alpine Joseph Fourier*, CNRS / Univ. Grenoble-Alpes)..... 21

Figure 2. Orthomosaics of the snow covered landscape from the set of images obtained from each flight. These are the UAV surveyed scenes used for processing the DEMs (Table 2). The scene numbers correspond to the time each UAV survey began. 21

Figure 3. Maps of the distribution of values for each variable used for modelling precision (a-g), and map of DEM error calculated from standard deviation which represents the spatial variation in measurement precision ($\hat{\sigma}^2$ in Equation 7, calculated from repeat aerial surveys; h). 24

Figure 4. Box plots of measurement precision (SD in elevation per pixel) for classes of each variable used to model precision with the GAM. These observations are based on the sample used for the GAM. The width of each box plot is proportional to the size of the group. 25

Figure 5. A spline function for non-parametric smoothing of the variables in the GAM.s..... 25

Figure 6. Bubble plot of estimated mean error between GNSS surveyed check points and SFM-MVS derived DEMs. 26

Figure 7. A terrain map illustrating the study site and UAV surveyed area (a). Ground-based (b,c) and UAV (d,e) images of the rock glacier taken on the survey dates in 2017. 34

Figure 8. Bubble plots of GNSS measured accuracies and orthomosaics obtained from UAV imagery (a,b). Maps of DEM precision calculated from repeat DEM observations (c,d)..... 38

Figure 9. SFM Snow depth map and bubble plot of snow depth accuracies based on snow-probed observations (a), and an SFM snow depth precision map (b). 39

Figure 10. Areas where the SFM-MVS snow depth level was determined to be significant based a t-test applied for each grid cell at a 0.05 significance level. The snow-free area was mapped from an orthomosaic of the UAV imagery. 40

Figure 11. Histograms of the spatially varying snow depth detection limit at a 95% confidence level (a), and SFM-MVS snow depths (b)..... 40

Figure 12. The impact of SFM-DEM spatial resolution on snow depth accuracy (RMSE). (a) the snow-on DEM was resampled to lower resolutions, (b) the snow-off DEM was sampled to lower resolutions, and (c) both DEMs were sampled to lower resolutions. 41

Figure 13. Orthomosaics of the snow-covered scenes on 22-Feb-2017 (a) and 2-Jun-2017 (c). Distribution of field surveyed GNSS points of snow-free areas and snow-probed measured. An outline of the stable and active terrain areas overlays the hillshade models of the Feb-2017 and Jun-2017 DEMs. The winter Feb-2017 DEM covers about half the area of the spring Jun-2017 DEM..... 49

Figure 14. A flowchart outlining the processes involved in estimating the sub-snow topography using non-rigid registration. The source and target snow-free DEMs used to model the general surface deformation pattern related to permafrost creep were the Oct-2017 and Aug-2012 DEMs, respectively. The optimal scale factor \hat{c} was obtained from mapped surface displacements, snow-free areas or in-situ snow-depth measurements. \hat{c} was optimized for the corresponding snow-cover date: either February 22, 2017 or June 2, 2017..... 54

Figure 15. A map of the study site terrain illustrated using a hillshade map and a 5 m contour interval (a), and the 2D (b) and 3D (c) displacement fields obtained from a free-form deformation model based on B-splines. The displacements magnitudes are shown here as the mean annual surface velocities (m/yr) from 2012-2017. The size of the arrows depicting the direction of the rock glacier movement is proportional to the magnitude of the displacements. 55

Figure 16. The performance of scaled values for est. Jun- and Feb-2017 DEMs based on optimization using snow-free elevation grid cells (Jun-2017) and in-situ snow-depth measurements (Jun-2017 and Feb-2017)..... 56

Figure 17. Estimated scale factor c compared to expected weeks 56

Figure 18. Elevation errors of the Jun-2017 DEMs based on GNSS surveyed elevations of snow-free areas. The errors have been grouped into active (i.e., on the rock glacier) and stable terrain. The est. Jun-2017 DEMs where $\hat{c}=0.07$ were obtained from the expected scale factor on 2-Jun-2017, and $\hat{c}=0.08$ was obtained from optimization of the elevation and in-situ snow-depth measurements. The Oct-2017 and Aug-2017 were untransformed DEMs. 58

Figure 19. Maps of the difference in elevations for the est. Jun-2017 ($\hat{c}=0.08$), Oct-2017 and Aug-2012 DEMs from the snow-free areas in the Jun-2017 DEM. 59

Figure 20. Box plots of the error between snow-probed measured and the DEM-derived snow depths for 2-Jun-2017 (a) and 22-Feb-2017 (b). The snow depth error has been grouped by active (i.e., on the rock glacier) and stable terrain. Est. Jun-2017 DEMs where $\hat{c}=0.07$ was obtained from the expected scale factor on 2-Jun-2017, and $\hat{c}=0.08$ was obtained from optimization of the elevation and in-situ snow-depth measurements. The est. Feb 2017 DEMs where $\hat{c}=0.12$ obtained from the expected scale factor on 22-Feb-2017, $\hat{c}=0.13$ from the optimization of the in-situ snow depth measurements, and $\hat{c}=0.14$ from the manually mapped displacements. The Oct-2017 and Aug-2017 were untransformed DEMs. 61

Figure 21. Snow depth maps derived from the est. Jun-2017 DEM ($\hat{c}=0.08$) (a) and the Oct-2017 DEM (b) for 2-Jun-2017, as well as a map of the difference in snow depth estimated by these DEMs (c). Positive values in the difference map indicate areas where the est. Jun-2017 DEM derived snow depths were deeper than the Oct-2017 DEM derived snow depths. 61

Figure 22. Snow depth maps derived from the est. Feb-2017 DEM ($\hat{c}=0.13$) (a) and the Oct-2017 DEM (b) for 22-Feb-2017, as well as a map of the difference in snow depth estimated by these DEMs (c). Positive values in the difference map indicate areas where the est. Feb-2017 DEM derived snow depths were deeper than the Oct-2017 DEM derived snow depths. 62

Figure 23. Profile of the rock glacier front illustrating transformed snow-free surfaces represented by (a.) scaling a model of only the vertical of displacements over time and (b.) by scaling a model of the 3D displacements over time. The transition colours from red to blue represent the modelled change in the snow-free rock glacier surface from 2012 (red) to 2017 (blue) obtained by scaling the modelled displacements using factors from 0 to 1 with a step of 0.1. The dotted line represents the snow-cover surface on 22-Feb-2017. The first plot (a.) shows that scaling only the vertical displacements does not capture the transition in elevations over time due to the movement of the rock glacier. The second plot (b.) shows how scaling modelled 3D displacements more realistically represents the elevation changes over time. 74

List of Tables

Table 1. Estimated proportion of deviance explained by each variable in the GAM. The higher proportion indicates a higher contribution to spatial variation in DEM precision.....	25
Table 2. Global statistics describing error estimated from GNSS check points for each UAV surveyed DEM, and the root mean square (RMS) reprojection errors corresponding to the image alignment within each DEM scene.....	26
Table 3. Summary of UAV flights used to derive SFM-DEMs for computing snow depth....	35
Table 4. Accuracy of DEMs calculated from GNSS surveyed checkpoints. June represents the snow-on DEM, and October the snow-off DEM.....	37
Table 5. SFM Snow depth accuracy based on snow-probed observations calculated for the entire area (overall), active terrain (i.e. on the rock glacier) and stable terrain.....	38
Table 6. Summary of data sets used for estimating snow depth. The vertical accuracy is based on a set of GNSS observations (N) surveyed for each date.....	49
Table 7. Error in elevations relative to the snow-free GNSS measurements in the Jun-2017 DEM. The errors have been grouped into active (i.e., on the rock glacier) and stable terrain. The est. Jun-2017 DEM where $\hat{c}=0.07$ was obtained from the expected scale factor on 2-Jun-2017 DEMs, and $\hat{c}=0.08$ was obtained from optimization of the elevation and in-situ snow-depth measurements. The Oct-2017 and Aug-2017 were untransformed DEMs. The median and mean error are reported as measures of bias.....	57
Table 8. Differences in elevations relative to the snow-free areas in the Jun-2017 DEM, and the errors in snow-depth estimation for 2-Jun-2017 based on the comparison of snow-probed measurements and DEM-derived snow depths. The errors have been grouped into active (i.e., on the rock glacier) and stable terrain. The est. Jun-2017 DEMs where $\hat{c}=0.07$ was obtained from the expected scale factor on 2-Jun-2017, and $\hat{c}=0.08$ was obtained from optimization of the elevation and in-situ snow-depth measurements. The Oct-2017 and Aug-2017 were untransformed DEMs. The median and mean error are reported as measures of bias.	59
Table 9. Errors in snow-depth estimation for 22-Feb-2017 based on the comparison of snow-probed measurements and DEM-derived snow depths. The errors have been grouped into active (i.e., on the rock glacier) and stable terrain. The est. Feb 2017 DEMs where $\hat{c}=0.12$ obtained from the expected scale factor on 22-Feb-2017, $\hat{c}=0.13$ from the optimization of the in-situ snow depth measurements, and $\hat{c}=0.14$ from the manually mapped displacements. The Oct-2017 and Aug-2017 were untransformed DEMs. The median and mean error are reported as measures of bias.....	60
Table 10. Summary of Agisoft PhotoScan processing settings.....	88
Table 11. Summary of survey details for October 5, 2017 (13 GCPs) and PhotoScan processing results	89
Table 12. Summary of survey details for June 2, 2017 (19 GCPs) and PhotoScan processing results	89

Table 13. Summary of survey details for Feb 22, 2017 (15 GCPs) and PhotoScan processing results	89
Table 14. Summary of UAV survey conditions	90
Table 15. Summary of bUnwarpJ processing settings using ImageJ for image registration...	90

List of Acronyms

AGL	Above ground level
ASL	Above sea level
CP	Checkpoint
DEM	Digital elevation model
GAM	Generalized additive model
GCP	Ground control point
GCV	Generalized cross-validation
GIS	Geographical information system
GNSS	Global navigation satellite system
GPS	Global positioning system
ICP	Iterative closest point
IMU	Inertial measurement unit
INS	Inertial navigation system
IQR	Interquartile range
k-NN	k -nearest neighbor
Lidar	Light detection and ranging
MAE	Mean absolute error
MVS	Multi-view stereo
PPK	Post processing kinematic
RAE	Relative absolute error
RANSAC	Random sample consensus
RGB	Red, green and blue optical bands
RMSE	Root mean squared error
RMS	Root mean squared
RTK	Real-time kinematic
SFM	Structure from motion
SIFT	Scale invariant feature transform
SRTM	Shuttle radar topography mission
UAV	Unmanned aerial vehicle (drone)

List of Symbols

$a(x)$	Grid cell displacements between two digital elevation models
c	Scale factor describing the magnitude of displacements
\hat{c}	An estimate of an unknown scale factor
D	Digital elevation model domain
$\hat{D}(x)$	Estimated snow depths for a continuous surface
e	Measurement error
ε	Random error
i	A checkpoint location
k	Number of repeat digital elevation model observations
j	Location of grid cell in repeat digital elevation model observations
μ	Bias or systematic error
$\hat{\mu}$	Estimated bias
n	Number of checkpoint locations
N	Number of elevation values in a digital elevation model
Ω_D	A set of snow-probed recorded depths
Ω_Z	A set of snow-free cell locations
p	Repeat elevation measurements at checkpoint locations n
$S(x)$	Digital elevation model of a snow-covered surface
σ	Standard deviation / precision
$\hat{\sigma}$	Estimated standard deviation / estimated precision
t_0	Time of observation
$T_a(x)$	A known transformation between two digital elevation models
$T_u(x)$	An unknown transformation function for a digital elevation model
$\hat{T}_u(x)$	An estimate of an unknown transformation
$v(x_i)$	Displacements mapped from locations in a snow-free DEM
x	A grid cell location
y	Observed elevation value
\bar{y}	Mean observed elevation value
z	'True' elevation value
\bar{z}	Mean reference elevation value

$Z(\mathbf{x})$ A digital elevation model of a snow-free surface
 $\hat{Z}(\mathbf{x})$ An estimate of an unknown digital elevation model

Chapter 1

General introduction

1.1 Motivation

Mountain snowpack is a crucial water resource in many regions of the World. A warming climate has resulted in a decline of seasonal snowpack in some mountain areas (Barnett et al., 2005; Mote et al., 2005; Lemke et al., 2007), which makes accurate monitoring, modelling and prediction of the seasonal snowpack vital to support water resource management strategies.

Detailed snow depth mapping using high-resolution elevation models has led to better predictions of snowmelt and its impact on the local hydrology (Painter et al., 2016; Brauchli et al., 2017), helped to design better snow depth sampling strategies (Deems et al., 2006; López-Moreno et al., 2011), and has improved modelling of how terrain and wind influence local snow accumulation patterns (Schirmer and Lehning, 2011; Grünewald et al., 2014; López-Moreno et al., 2015). Accurate snowpack data is also important for improving our understanding of mountain environmental processes including vegetation patterns (Palacios and Sánchez-Colomer, 1997; Jonas et al., 2008; Litaor et al., 2008), changes in ground temperature (Luetsch and Haeberli, 2007; Apaloo et al., 2012), landslides (Matsuura et al., 2003; Okamoto et al., 2018), rock falls (Haberkorn et al., 2016), avalanches (Bühler et al., 2011), glacier dynamics (Immerzeel et al., 2014; Rossini et al., 2018), and permafrost creep (Ikeda et al., 2008).

With recent advances in structure from motion (SfM) multi-view stereo (MVS) 3D reconstruction (or SfM photogrammetry) techniques, we have seen encouraging developments in high resolution elevation modelling that can help tackle a classical problem in snow research: How can we better capture snow patterns to improve our understanding of snow depth distribution (Sturm, 2015)? In general, SfM-MVS techniques can create a 3D reconstruction of a surface from a collection of images. By differencing co-registered snow-covered and snow-free elevation models derived from SfM-MVS, high-resolution snow depths can be computed. Snow depth mapping using SfM-MVS can improve our ability to collect data with better resolution, frequency and spatial coverage.

Due to the low-cost of operation and ability to obtain good coverage, unmanned aerial vehicles (UAVs), commonly known as drones, have become a popular method to collect images for SfM-MVS processing (Colomina and Molina, 2014; Smith et al., 2015). This combination of SfM-MVS with UAVs has an excellent potential to provide detailed snow depth observations in challenging mountain terrain.

Snow depth at the basin, catchment or slope scale can be estimated by manual surveying, lidar (light detection and ranging) and digital photogrammetry (Tedesco et al., 2015; Marti et al., 2016). Although manual probing of snow combined with real-time-kinematic (RTK) or differential global navigation systems (GNSS) surveying is the most accurate and precise way to obtain quality snow depth observations, it can be expensive, time consuming and potentially dangerous depending on the site conditions (Deems et al., 2013). Additionally, it suffers from poor spatial coverage, which makes it difficult to observe true snow distributions where snow depth is highly spatially heterogeneous (Elder et al., 1991; Hiemstra et al., 2006).

Lidar snow depth estimates have generally overcome the issues of spatial coverage and survey dangers. Typically, airborne vertical accuracies of lidar estimates are at the decimeter scale and are spread out (horizontally) at 1 m point spacing (Hodgson and Bresnahan, 2004; Deems et al., 2013). Although lidar remains one of the most accurate techniques for remote sensing of snow depth, in particular in forested areas, recent works by Nolan et al. (2015), Bühler et al. (2015; 2016a), Vander Jagt et al. (2015), Michele (2016), Harder et al. (2016), and Avanzi et al. (2018) have demonstrated the potential for high-resolution snow depth mapping using optical imagery collected from airborne surveys using SFM-MVS.

The SFM-MVS approach may have some advantages over lidar. A comparison of airborne lidar and SFM-MVS snow depth estimations conducted by Nolan et al. (2015) found for their study conditions that SFM-MVS had twice the precision of lidar and about the same accuracy. SFM-MVS can produce a colour orthoimage co-registered with the derived digital elevation model (DEM). This orthoimage makes it easy to identify what is snow covered and what is not, which can be useful for depth estimation in thin snowpack conditions. Additionally, acquisition and processing of SFM-MVS data is substantially less expensive than using lidar (Nolan et al., 2015; Vander Jagt et al., 2015).

A challenging aspect of snow depth mapping with high-resolution elevation models is overcoming issues of measurement uncertainty, especially in areas of shallow snowpack (Hopkinson et al., 2012; Harder et al., 2016). The major challenge being, what can we detect as real snow depths from noise? This measurement uncertainty is ingrained in elevation model differencing. It is generally controlled by the elevation model quality (Wechsler and Kroll, 2006; Wheaton et al., 2010) and co-registration accuracy (Nuth and Kääb, 2011; Marti et al., 2016; Bernard et al., 2017; James et al., 2017b). In snow depth mapping with elevation models, any changes in the topography beneath the snow cover occurring in the time between the elevation model acquisition dates can be an additional source of uncertainty (Nolan et al., 2015; Bernard et al., 2017; Avanzi et al., 2018).

Although SFM-MVS has already been widely applied in the geosciences (Smith et al., 2015), there is a need to better understand the quality and uncertainties in SFM-MVS elevation models. Elevation model error is in general difficult to model because the error can be spatially nonstationary, heteroscedastic and spatially autocorrelated (Carlisle, 2005). Research in geosciences has been trying to spatially quantify uncertainty in topographic surveying for quite some time (Brasington et al., 2000; Lane et al., 2003; Wheaton et al., 2010; Lague et al., 2013; Schaffrath et al., 2015).

The most basic approach to modelling uncertainties related to differencing elevations is to assume that errors in the elevation models are spatially uniform (Brasington et al., 2000; Passalacqua et al., 2015). Nolan et al. (2015) and Michele et al. (2016) found that SFM-MVS snow depth errors vary not only from site to site, but also spatially within a scene. Thus, making such assumptions may lead to misinterpretation of what snow depths or changes in depths are detected (Wheaton et al., 2010). A detailed uncertainty analysis that accounts for the spatial variation in errors is therefore necessary to verify the quality and usability of snow depths mapped using SFM-MVS 3D reconstruction.

1.2 Research objectives

The goal of this thesis is to enhance our understanding of measurement uncertainties related to SFM-MVS mapping of snow depth using UAV imagery and field-based measurements collected in an alpine environment. To achieve this goal, this thesis focuses on the following research questions and objectives:

What main UAV survey design and environmental factors characterize the spatial variation in SFM-MVS derived DEM uncertainty?

Since SFM-MVS snow depths are computed from differencing elevations models, the first step to quantifying snow depth mapping uncertainties is to describe and model how SFM-MVS elevation model errors vary spatially.

The objectives of this research questions are to:

- Describe and define SFM-MVS DEM error
- Develop an approach to spatially estimate the precision of SFM-MVS DEMs
- Characterize the influence of UAV survey design and field site conditions on SFM-MVS DEMs using regression modelling

How do the uncertainties in the snow-covered and snow-free SFM-MVS DEMs affect the spatial distribution of uncertainties in the computed snow depths?

Using spatially varying estimates of SFM-MVS DEM precision, the precision of the snow depths can be determined using a model of error propagation. Snow depth detection limits can be determined using the precision of the snow depths. This detection limit (or margin of error) can communicate where and how much random sampling error can be expected for a particular SFM-MVS survey.

The objective to this research question is to:

- Calculate the spatially varying precision of SFM-MVS snow depths using an error propagation model
- Statistically determine spatially varying snow depth detection limits using SFM-MVS DEM precision estimates

What effect does the spatial resolution of the SFM-MVS elevations models (snow-covered and snow-free) have on the accuracy of computed snow depths?

Although SFM-MVS techniques combined with UAV imagery can capture very high-resolution data, such fine detail may not be required for a particular application. This research question explores the issue of the spatial resolution of observations and its impact on the quality of SFM-MVS snow depths.

The objective to this research question is to:

- Model the effect of the snow-covered and snow-free DEMs spatial resolution on snow depth accuracy using in situ snow depth measurements and image resampling methods

What is the effect of on-going slope deformation processes on the quality of SFM-MVS snow depths? And how can changes in the sub-snow ground surface be corrected to reduce errors in SFM-MVS snow depths?

In addition to errors in SFM-MVS elevation models, snow depth errors in alpine areas can be caused by on-going ground deformation processes, such as permafrost creep. Accounting for such errors is important to link the impact of snowpack properties to local environmental processes.

The objectives of these research questions are to:

- Assess the influence of permafrost creep on SFM-MVS snow depth errors by comparing in situ snow depth measurements on stable and actively deforming terrain to SFM-MVS snow depths.
- Determine and apply a method to correct snow depth errors caused by on-going slope deformation processes.

Overall, these research questions and objectives are aimed at quantifying, characterizing and reducing uncertainties in SFM-MVS snow depths mapped in alpine areas.

1.3 Thesis outline

This cumulative doctoral thesis is organized as follows. This first chapter introduces the motivation, main research questions and objectives of this thesis. Chapter 2 provides a general overview of elevation modelling using SFM-MVS 3D reconstruction techniques, and a summary of previous applications for snow depth mapping.

Chapter 3 describes how definitions of error in SFM-MVS derived DEMs may vary depending on the available validation data, presents a method to estimate the spatial variation in DEM uncertainty, and characterizes the main survey design and environmental factors influencing uncertainty for a case study of snow-covered terrain in the French Alps.

Chapter 4 explores measurement uncertainties in SFM-MVS snow depth mapping for a case study in the French Alps. It describes how spatially varying estimates of SFM-MVS snow

depth precision can be obtained using a model of error propagation, and how the Student's t distribution can be used to determine spatially varying snow depth detection limits from repeat observations. Additionally, the effect of DEM spatial resolution on SFM-MVS snow depth accuracy is explored.

Chapter 5 addresses the issue of measurement errors that can occur in SFM-MVS snow depth mapping, and in general in snow depths estimated from DEM differencing, due to on-going slope deformations in alpine terrain (i.e., permafrost creep). A novel method to reduce errors in the SFM-MVS snow depths based on surface deformation modelling is presented for a case study in an alpine environment.

Chapter 6 discusses the main contributions of this study, limitations, provides suggestions for future research, and presents a summary of the main conclusions.

Chapter 2

Structure-from-motion multi-view stereo 3D reconstruction

2.1 Introduction

Structure from motion (SFM) combined with multi-view stereo (MVS) is a method for image-based 3D reconstruction. The geometry of a scene can be resolved from a series of overlapping images taken from different viewpoints. The major difference from conventional photogrammetry is being able to solve for camera positions and orientation automatically without prior knowledge (Verhoeven, 2011; Westoby et al., 2012). The images can be collected using ground-based (i.e. terrestrial) and aerial observations – UAVs being one of the most used methods for image collection in geosciences.

A 3D model is constructed using SFM by first applying an algorithm that automatically aligns overlapping images and detects matching feature points or key points (Lowe, 2004). Next, a bundling adjustment algorithm is used to refine SFM estimated camera parameters (Favalli et al., 2012). This unscaled, sparse 3D point cloud can then be georeferenced using either ground control points (GCPs), geolocations of the camera position or a combination of both. The last step utilizes MVS image matching algorithms to generate a dense 3D point cloud from the computed camera positions and additional parameters, which can be interpolated into a mesh and subsequently a grid to create a digital elevation model (DEM; Smith et al., 2015).

2.2 Structure from motion

The recent success of SFM-MVS is for a large part due to the improvements of SFM algorithms. In particular, developments in image feature detection (Harris and Stephens, 1988; Lowe, 2004; Rosten and Drummond, 2006), and descriptors (Lowe, 2004; Leutenegger et al., 2011; Rublee et al., 2011; Alahi et al., 2012). Altogether, these improvements have contributed to enhancing the quality of tracks derived from unstructured datasets consisting of images with very different pose and illumination (Furukawa and Hernández, 2015; Micheletti et al., 2015b).

Structure from motion algorithms are commonly used to produce (1) the camera parameters for every image, and (2) to compute a set of 3D points visible in the images, referred to as tracks, from unordered sets of images. Both products are a requirement to run MVS algorithms for producing more detailed 3D reconstruction models.

The camera parameters are a set of extrinsic and intrinsic properties (or values) describing the camera configuration corresponding to each image. The extrinsic properties relate to the

camera pose information consisting of the camera orientation and location, where the intrinsic properties refer to internal camera properties such as focal length and pixel size (Furukawa and Hernández, 2015). A track consists of the 3D coordinates of a feature and a list of the 2D coordinates for the corresponding matches in other images.

The SFM pipeline can be generalized into the following steps (Snavely et al., 2008; Furukawa and Hernández, 2015):

1. Feature correspondence

- Detect 2D features in each image
- Match the 2D features between pairs of images
- Organize matches into tracks

2. Structure from motion

- Produce an SFM solution from the tracks
- Apply the bundle adjustment to iteratively refine the SFM model

Lowe's (2004) Scale Invariant Feature Transform (SIFT) is one of the most popular image descriptors used for feature correspondence (Snavely, 2008). SIFT has good invariance to image transformations; that is, it performs well to detect and describe 2D image features from a set of images with variation in viewpoints and illumination (Lowe, 2004). SIFT works by first identifying features of an object within an image by searching over multiple scales and locations. Once these candidate features are identified, a model of the scale and location is combined with the computed orientation and the image gradient (corresponding to local cell neighbours) to produce a descriptor. This highly distinctive descriptor is subsequently used to identify matching features in overlapping images.

Matching features in multiple images is typically done using the approximate nearest neighbour (ANN; Arya et al. 1998), and applying the Random Sample Consensus (RANSAC; Fischler and Bolles, 1981) algorithm usually filters out any incorrect correspondences. The tracks produced from these algorithms are used as input to the bundle adjustment, which recovers and refines the camera parameters and outputs a sparse 3D point cloud.

The bundle adjustment is used to improve estimates of camera parameters by minimizing the distance between a projected/estimated point location and a measured one (i.e. the reprojection error; Granshaw, 1980; Triggs et al., 2000). This minimization is performed using a non-linear least squares method – usually the Levenberg-Marquardt minimization algorithm (Zhang et al., 2006). The accuracy of this estimation is commonly expressed using the root mean square error (RMSE), which is measured in pixels. After a bundle adjustment the RMSE should be sub-pixel; normally, before the bundle adjustment the RMSE is in the order of several pixels (Furukawa and Hernández, 2015).

There are generally two methods for initialisation of the bundle adjustment, sequential and factorisation algorithms: sequential being the most popular (Robertson and Cipolla, 2009). The sequential algorithms work by including each image (or view) one at a time. As each image is added, a partial reconstruction is extended, and triangulation is applied to estimate the

positions of the 3D points visible in overlapping images. In contrast, factorisation algorithms work by computing the scene geometry and camera pose all at once. A major problem of this method is it requires every 3D point to be visible in every image; that is, it does not deal well with missing data (Robertson and Cipolla, 2009).

2.3 Multi-view stereo

After the camera intrinsic and extrinsic parameters have been solved, MVS algorithms can be applied to compute a detailed 3D reconstruction of a scene. MVS algorithms can create a 3D model by representing the geometry of a scene in different ways such as depth maps, point clouds, voxels or meshes.

In depth map reconstruction, depth maps are computed for each image and merged to into a single 3D model (Szeliski, 1999; Seitz et al., 2006; Li et al., 2010; Furukawa and Hernández, 2015). A depth map is an image where the distances to a viewpoint are computed for all pixels.

Point cloud reconstruction or patch-based surface representation computes a single point-cloud 3D model using all images. Spatial consistency assumptions are used to allow the point cloud to expand across the reconstructed scene. Patch-based Multi-View Stereo (PMVS) is a widely used approach to point cloud reconstruction (Furukawa and Hernández, 2015), and works by matching features, expanding patches and then filtering incorrect matches (Carrivick et al., 2016).

Voxel reconstruction or volumetric scene modelling is based on dividing the 3D space into a set of voxels (Seitz and Dyer, 1999), projecting the voxel and matching voxels based on a photo-consistency measure (e.g. sum of absolute squared difference or normalized correlation coefficient). Edges of features in the images can also be used to segment the voxels into features. The boundary of the segments are then used to extract a surface model (Seitz and Dyer, 1999; Furukawa and Hernández, 2015)

Mesh reconstruction or surface evolution models work by building a conservative bounding box around the scene, and then iteratively reshaping the surface to fit a point cloud until some cost function is minimized (Kazhdan et al., 2006; Tagliasacchi et al., 2011; Carrivick et al., 2016). These methods are robust to noisy real-world data, and are useful for reconstructing the surface in a scene where small holes or patches of no data are present in the point cloud (Kazhdan et al., 2006; Tagliasacchi et al., 2011).

In general, there are a variety of MVS algorithms available (Seitz et al., 2006; Furukawa and Hernández, 2015), and they are often combined to achieve optimal results for a given scene.

2.4 Georeferencing

The SFM procedure estimates only the relative positions of cameras/images. To make absolute measurements, and to be able to compare with SFM-MVS reconstructions with other spatial datasets, these positions must be projected into a georeferenced coordinate system (Snavely et al., 2006). In contrast to traditional photogrammetry, not every image is required to have

ground control points (GCPs) for georeferencing (Fonstad et al., 2013). Instead, georeferencing requires either a minimum of three GCPs for the entire image network or knowing the exact camera position for each image.

Ground control is in general required to orient data derived from remotely sensed imagery to a referenced coordinate system. SFM-MVS surveys can generally be transformed into a coordinate system by direct measurement of camera positions determined from RTK-GNSS and inertial navigation systems (INS), surveying natural and artificial ground targets, or by registering to a previously controlled image. Similar to traditional photogrammetry, GCPs for SFM should cover the full extent of the study area and be well distributed (James and Robson, 2012; Javernick et al., 2014).

Depending on the project, the number and distribution of GCPs can vary. It is generally better to be redundant and include more GCPs to avoid possible mistakes, such as having poor quality GNSS positioning measurements (James et al., 2017b). Tonkin et al. (2016) observed that using a minimum of four GCPs could more than double the vertical accuracy of SFM-MVS DEMs compared to using only three. Additionally, the distribution of GCPs strongly influences the accuracy and precision of georeferencing (Tonkin and Midgley, 2016; James et al., 2017a).

Poorly distributed GCPs, such as clustered in isolated portions of a survey site may result in doubling the RMS error (Harwin and Lucieer, 2012; James and Robson, 2012). Also, the vertical error in the SFM-MVS DEMs appears to be spatially correlated to the position of GCPs. For example, Tonkin et al. (2016) found that the vertical accuracies followed a strong polynomial trend where accuracies decrease for locations further away from the GCPs. For best results, the GCPs should be evenly distributed throughout the survey (James and Robson, 2012; James et al., 2017b). It is also recommended to increase the sampling density of GCPs when surveying steeper terrain to adequately capture the variation in position estimates (Harwin and Lucieer, 2012; James et al., 2017a). Using well-distributed and clearly visible GCPs, it is possible to achieve a magnitude of accuracy similar to RTK-GNSS/differential GPS measurements (< 5 cm) when flying a UAV at a height between 40-50 m (Harwin and Lucieer, 2012), as well as strengthen the precision (i.e., repeatability) of the survey (James et al., 2017b).

2.4.1 Artificial ground control points

Natural landscapes do not always have the most suitable features useful for ground control. It may be difficult to identify natural features that stand out in the imagery (e.g. coastal sand dunes; Brunier et al., 2016), or it may be difficult to survey features that stand out due to challenging terrain (e.g. rugged mountain terrain; Barrand et al., 2009). Direct georeferencing or using control points obtained from laser scanned imagery are some examples of how to overcome this challenge; however, the most accurate and common technique in natural landscapes is the use of highly visible (i.e. a clearly defined centroid) artificial ground targets (Westoby et al., 2012). Ground targets may not always be necessary. It is also an option to produce the SFM point cloud, identify surface features that stand out clearly, revisit the site and survey these features (e.g. Fonstad et al., 2013).

2.4.2 Direct georeferencing

In theory, SFM-MVS point clouds can be georeferenced without ground control if the exact location of the camera is known. Determining this exact position in space can be challenging with UAVs. Some factors that need to be considered are the precision of the quality of the onboard GNSS receiver, the quality and position of the GNSS antenna, and the geotagging accuracy.

The navigation grade single frequency GNSS receivers, which are commonly used on consumer UAVs, have a low positional accuracy (2-5 m) that alone is not accurate enough to be used for georeferencing the camera position. However, differentially correcting the GNSS positions (e.g., applying post processing kinematic corrections – PPK) can greatly improve the measurement of camera position (Turner et al., 2014). With the correct setup a spatial error of ± 10 -20 cm for a SFM derived elevation model can be achieved (Turner et al., 2014). This level of error was achieved for a generally flat surface, and higher errors would be expected for more complex topography (e.g. higher variation in point density). The spatial error can therefore be further reduced by the integration of dual frequency receivers on a UAV platform, which has been seen to achieve a level of accuracy < 10 cm (Vander Jagt et al., 2015). Also, direct georeferencing with a strong positional accuracy can result in survey precisions similar to using a well-distributed network of GCPs (James et al., 2017a).

2.5 Reconstruction quality

How SFM-MVS algorithms perform under different physical conditions is not very well known. SFM-MVS algorithms can perform differently under different conditions, and there is a need for researchers, through good experimental design, to explore this behaviour to improve SFM-MVS algorithms (Oliensis, 2000; Snavely et al., 2008). In particular, ground validation is required to determine the most accurate SFM-MVS techniques.

Many recent applications of SFM-MVS in geosciences do a good job of ground validation. For example, Javernick et al. (2014) compare their SFM-MVS modelling results of a braided river channel to just over 10 000 RTK-GNSS surveyed check points (CPs). In doing so, they managed to uncover a systematic broad-scale error in the estimation of surface elevation. This systematic error has also been observed by James and Robson (2012) and can be seen in the results in Rosnell and Honkavaara (2012). Observing this systematic error has resulted in research focused on SFM-MVS model optimizations and UAV survey designs to mitigate this error and improve the quality of the 3D point cloud (James and Robson, 2014; Tonkin and Midgley, 2016; James et al., 2017a; James et al., 2017b).

This kind of research is excellent for progressing the field of SFM-MVS applied to geosciences; however, as mentioned before, it is complicated by the many different SFM-MVS algorithms (or software) available. That is, it can be at times uncertain if this error also occurs when other SFM-MVS algorithms are applied (Smith et al., 2015). Therefore, given the current state of SFM-MVS research, experiments benchmarking different algorithms under different

environmental conditions remains critical for enhancing our practical understanding of the SFM-MVS approach to 3D reconstruction (Seitz et al., 2006; Snavely et al., 2008).

In geosciences, quality of SFM-MVS 3D reconstructions has been observed to be affected by the camera and its lens (Micheletti et al., 2015a; Niederheiser et al., 2016; James et al., 2017a), the resolution and number of images acquired (James and Robson 2014; Micheletti et al. 2015a), the viewing directions of those images (i.e., the image network; James and Robson, 2014), the SFM-MVS processing software/workflow (James and Robson, 2012; Ouédraogo et al., 2014; Turner et al., 2014; Niederheiser et al., 2016), the georeferencing approach (i.e., the distribution and quality of ground control points; Tonkin and Midgley, 2016; James et al., 2017a), having the appropriate scale for a particular application (Smith et al., 2015), the presence of vegetation cover (Westoby et al., 2012; Hugenholtz et al., 2013; Micheletti et al., 2015b; Nolan et al., 2015), and image texture (Seitz et al., 2006; Fonstad et al., 2013; Micheletti et al., 2015b; Nolan et al., 2015)

2.5.1 Image and network quality

Since SFM is a geometric problem, the image network, which is made up of the number of images, their overlap and viewing angles, plays a key role in the quality of the SFM-MVS reconstruction results. For SFM to perform best, multiple images must view matching features from multiple viewpoints. Although technically only two overlapping images are required, more robust 3D coordinate estimates can be obtained when a minimum of three images are used (Furukawa and Hernández, 2015). In general, SFM performs better with more images (Furukawa and Hernández 2015).

It is not always necessary to have a large set of images for good results as long as the image geometry remains strong (Micheletti et al., 2015b). Additionally, there are different image requirements for SFM and MVS solutions. MVS algorithms typically perform extremely well with a large number of high-resolution images. That is, they can create a detailed reconstruction without being heavily influenced by ambiguous feature matches. In contrast, these ambiguities, which usually correspond to high-resolution imagery, can become a problem for SFM algorithms (Furukawa and Hernández, 2015).

SFM performs well when the viewing angle difference between images ranges between 5-15 degrees (Furukawa and Hernández, 2015). Angular changes greater than 25-30 degrees between overlapping images can lead to poor performance of the automatic feature matching algorithms (Moreels and Perona, 2007). Matching in this case may be prevented because the surface texture appears too dissimilar in the images from different viewpoints (Micheletti et al., 2015b).

Higher resolution imagery has the potential to improve the detection of unique pixels (i.e. features) that may be identifiable in multiple images. The quality of the lens is also important. For example, imagery taken from a high-resolution camera with a poor lens may worsen the SFM estimated camera positions, which subsequently will lead to poorer results of the MVS derived dense point cloud (Furukawa and Hernández, 2015). Additionally, it is also critical to

ensure that the camera exposure is set ideally to capture the required detail (Micheletti et al., 2015a), and the images are in focus (Furukawa and Hernández, 2015).

Although many MVS algorithms can handle illumination variations in multiple images, best results are obtained when these variations are stable. That means making sure that the lighting (e.g., shadings and shadowing effects) is well balanced within and across multiple images (Furukawa and Hernández, 2015). MVS algorithms can perform well on smooth surfaces, as long as subtle shading variations on the surface are present for feature matching (Seitz et al., 2006).

Some common feature matching issues are related to surveying in natural conditions include (Bemis et al., 2014):

- Homogenous surface textures, such as due to reflections, flat surfaces with little variation in texture, and deep shadows.
- Changes in the feature appearances between images due to wind moving vegetation, or the movement of animals, people and vehicles.
- Changes in the illumination, e.g., caused by a variable cloud cover, or changes in the sun position.

2.5.2 The 'doming' effect

One of the major impacts on the quality of the SFM-MVS reconstructions is poor modelling of the radial distortion in a camera lens (i.e. intrinsic camera parameters; Magri and Toldo, 2017). An inaccurate camera-lens distortion model can result in a systematic broad-scale error in SFM-MVS elevation models. These errors are expressed in the elevation models as a vertical 'doming' (deformation) of the surface. A poor image network caused by collecting the images at near-parallel directions to the ground, which is common in UAV surveying, can produce an unreliable camera calibration for correction of any radial lens distortions (James and Robson, 2014). The easiest way to uncover such an error is to compare the 3D model reconstruction with well distributed ground control data.

This 'doming' effect can be mitigated by designing the aerial survey to allow for variety of camera inclination, by providing an accurate camera model for the bundle adjustment procedure (James and Robson, 2014), or by allowing the camera model to vary during the bundle adjustment (Javernick et al., 2014). For example, a fixed wing UAV could obtain oblique images by adding a gently curved overpass to the survey, or by having a system where the camera can be inclined (James and Robson, 2014).

A 'metric' survey camera, which is designed for photogrammetry, can help minimize the 'doming' effect. They have a well-defined camera model where radial distortions are minimal. This contrasts with consumer grade cameras. They have a less accurate camera model, which may need to be automatically calibrated during the bundle adjustment (James and Robson, 2014). If no accurate camera model is available for a consumer grade camera, Javernick et al. (2014) found that allowing the bundle adjustment to optimize camera model parameters with ground control can considerably reduce the 'doming' error pattern. This works by re-running the bundle adjustment using the external information provided by the ground control, which

minimizes the sum of the re-projection error and the georeferencing error (Smith et al., 2015). This approach improves the error locally where ground control is located, and the overall precision of the model is also improved (James and Robson, 2014; Javernick et al., 2014).

2.6 SFM-MVS applied for snow depth mapping

Most research using SFM-MVS for snow depth mapping has focused on testing the reliability of UAV and SFM-MVS methods for producing quality high-resolution snow depth data. With the exception of Harder et al. (2016) and Fernandes et al. (2018), few studies have used SFM-MVS methods for hydrological and general environmental analysis. This is mainly due to the need to better understand the limitations of SFM-MVS snow depth mapping (Bühler et al., 2016a; Bernard et al., 2017).

In general, snow depth from SFM-MVS 3D reconstruction can be obtained by differencing two co-registered elevation models, one of snow-free and the other of snow-covered conditions. Additionally, snow accumulation or ablation can be calculated by differencing two snow-covered scenes. The difference between two scenes can be calculated from either DEMs interpolated from the dense point cloud or raw point cloud elevations.

Accuracies of snow depth (i.e., RMSE) estimation using SFM-MVS have been observed to vary from 4 cm to 30 cm (Nolan et al., 2015; Vander Jagt et al., 2015; Bühler et al., 2016a; Harder et al., 2016; Michele et al., 2016; Avanzi et al., 2018). These accuracies are in general comparable to snow depths calculated from terrestrial lidar surveys (Piermattei et al., 2016; Avanzi et al., 2018). Nolan et al. (2015) suggests the accuracy limitation for measuring snow depth is around ± 10 cm when using GCPs for controlling geolocation accuracy. When using highly accurate RTK-GNSS measurements (direct georeferencing) for camera locations and no GCPs, reliable measurements may be obtained for snow depths greater than 20 to 30 cm (Nolan et al., 2015; Vander Jagt et al., 2015).

The biggest challenges to obtaining quality snow depth maps using SFM-MVS are snow and lighting conditions. Fresh snow creates a smooth surface texture, which makes it difficult to detect unique features for performing image matching (Nolan et al., 2015; Bühler et al., 2016b; Cimoli et al., 2017). Flat-diffused light can hide subtle features in the snow cover surface due to a lack of contrast in the surface texture (Bühler et al., 2016b; Cimoli et al., 2017). These sources of error usually cause large data gaps in the reconstructed snow-covered surface (Bühler et al., 2016b). This problem can usually be resolved by just waiting for optimal lighting conditions (Nolan et al., 2015; Gindraux et al., 2017), by pre-processing the images to enhance contrast or by using near infrared (NIR) imaging (Bühler et al., 2016b). The worst case in this scenario may result in a reduced point cloud density, which may be handled by either reducing the resolution of the elevation model or marking these locations as having no data (Nolan et al., 2015; Gindraux et al., 2017).

In general, temporal influences on surface conditions may lead to errors that are difficult to estimate; e.g., lighting conditions (Bühler et al., 2016b; Harder et al., 2016; Gindraux et al., 2017), vegetation compaction (Nolan et al., 2015; Vander Jagt et al., 2015), frost heave (Nolan et al., 2015), and on-going erosion processes (Bernard et al., 2017). The influence of vegetation

on surface elevation estimation may be systematic and therefore corrected, but this hypothesis needs further investigation (Hugenholtz et al., 2013). Accounting for the errors from frost heave potential is not very feasible, considering you can only observe such effects under snow-free conditions (Nolan et al., 2015).

In addition to these temporal influences, cases can occur where obtaining matched points in an imagery set can be difficult (James and Robson, 2012), such as observed by Piermattei et al. (2016) who had difficulties reconstructing a 3D sparse point cloud for parts of a glacier which was covered by fine debris. Substantial error in snow depth estimation can also potentially occur from small errors in the georeferencing and/or co-registration of snow-free and snow-covered scenes (Nuth and Kääb, 2011; Tinkham et al., 2014; Cimoli et al., 2017). These errors can be exacerbated in areas of high slope (Hopkinson et al., 2012; Marti et al., 2016).

In summary, there is much room for improving the understanding of the uncertainty in SFM-MVS snow depth mapping. Before performing large scale applications of this approach, it is important to thoroughly know its limitations to avoid producing poor quality data that may not be suitable for analysis or may lead to erroneous results.

Chapter 3

Modelling the precision of structure-from-motion multi-view stereo digital elevation models from repeated close-range aerial surveys

Abstract

The accuracy of digital elevation models (DEMs) derived from structure-from-motion (SFM) multi-view stereo (MVS) 3D reconstruction is commonly computed for a single realization of model elevations. This approach may be adequate to estimate an overall measure of systematic error; however, it cannot provide a good estimation of measurement precision. Knowing measurement precision is crucial for measuring elevation surface changes observed by DEM comparisons. In this paper, we illustrate an approach to characterize spatial variation in the precision for SFM-MVS derived DEMs. We use a snow-covered surface of an active rock glacier located in the southern French Alps as the case study. A spatially varying precision estimate is calculated from repeated close-range aerial surveys for a single acquisition period by calculating the standard deviation per grid cell between the DEMs created for each flight repetition. Regression analysis using a generalized additive model (GAM) is performed to model the estimated precision and provide insights regarding how sensor, survey design and field site conditions may spatially influence the measurement precision. Additionally, we define how DEM error can be described differently depending on the available validation data. In our study image height above ground level and distance to ground control points had the greatest explanatory power for spatial variation in DEM precision. Image overlap mean reprojection error and saturation were also useful for explaining spatially varying measurement precision of the DEMs. Field site characteristics, such as slope angle and shading, had the least importance in our model of precision. From a practical point of view, regression-modeled relationships between precision and image and site characteristics can be utilized to design future surveys with similar sensing platforms and site conditions for improved DEM precision.

3.1 Introduction

One of the most recent developments in digital elevation model (DEM) generation methods is the use of structure-from-motion (SFM) and multi-view stereo (MVS) 3D reconstruction techniques (James and Robson, 2012; Westoby et al., 2012; Micheletti et al., 2015b; Smith et al., 2015; Carrivick et al., 2016). In general, these techniques can create a 3D reconstruction of a surface from a collection of images for a given feature taken from a variety of viewing angles (Snavely et al., 2006). It has become vastly popular for geosciences applications (see (Carrivick

et al., 2016) for an extensive list). As with the use of any DEM, it is crucial to understand the quality of the SFM-MVS derived DEMs to ensure the suitability for a particular application.

The quality of DEMs can be described by analyzing its errors (Fisher, 1998). In general, all DEMs inherently contain some error (Fisher and Tate, 2006), and systematic and random error structures can vary between different sensors and survey designs (Wilson 2010). These errors will propagate to DEM derivatives, such as slope, aspect and the hydrologic or geomorphic models that utilize these derivative products (Walker and Willgoose, 1999; Holmes et al., 2000). As a result, DEM error can contribute to the uncertainties related to monitoring Earth surface changes (Brasington et al., 2000; Burns et al., 2010; Wyrick and Pasternack, 2016). A model of DEM error can be developed to characterize DEM uncertainty for a particular survey technique and site (Holmes et al., 2000; Wheaton et al., 2010; Tinkham et al., 2014; Bangen et al., 2016). Such a model can be used to not only determine possible sources of errors, but also to improve methods of DEM production (Fisher, 1998; Carlisle, 2005; James and Robson, 2014; James et al., 2017b).

The most common approach to modelling the spatial variation in DEM errors has typically been to stochastically simulate DEM error distributions (Fisher, 1998; Kyriakidis et al., 1999; Holmes et al., 2000; Fisher and Tate, 2006; Wechsler and Kroll, 2006). Recently, such an approach has been applied to assess error in SFM-MVS elevation models using Monte Carlo simulation; in particular, the authors evaluated how survey design may influence the distribution of precision in a DEM (James et al., 2017a; James et al., 2017b). Since there are numerous factors that can lead to errors in the SFM-MVS DEM (Smith and Vericat, 2015), it is possible that the simulation approach could potentially overlook factors, such as field conditions (Favalli et al., 2012), that may affect the distribution of error in DEMs derived from SFM-MVS 3D reconstruction.

The purpose of this study is to assess DEM error by estimating measurement precision of SFM-MVS derived DEM values to characterize how precision may spatially vary and to explain this variability. Repeat aerial surveys from an unmanned aerial vehicle (UAV) can be used to create multiple DEMs for estimating precision. This approach computes the precision for individual grid cells of the DEM image of surface elevations. That is, we estimate the precision corresponding to each grid cell. In this way, we are treating each grid cell as a separate measurement, and we are using a model of error that allows for the values of precision to vary spatially. Additionally, a generalized additive model (GAM), a nonlinear statistical regression technique, is used for characterizing the spatial variation in precision by modelling the respective influences of sensor, survey and field site conditions.

3.1.1 Describing DEM measurement error

Typically, analysis of the spatial pattern of errors in DEMs focuses on the difference between the measured values and some 'true' value that is perceived as more accurate (Kyriakidis et al., 1999; Smith and Vericat, 2015); *i.e.* where the reference data used for validation is considered as the 'truth'. In this paper, we focus on measurement bias, the mean difference between measured values and some 'true' value, to describe the pattern of error. Bias can be used to describe the presence of systematic error, which is the tendency of measurements to,

on average, under- or overestimate the 'true' values. Additionally, we define precision of a measurement as the variability in values between multiple observations. It can be used to describe random error and can be assessed in terms of reproducibility or repeatability.

Most SFM-MVS studies in the geosciences have focused on reproducibility (Smith and Vericat, 2015; Clapuyt et al., 2016). Reproducibility can be defined as how measurements vary using different sensors under different conditions, including different periods (Bartlett and Frost, 2008). These studies are popular for good reasons: they seek to optimize experimental parameters to produce the best 3D reconstruction results for a variety of sensor and field conditions (e.g., (Clapuyt et al., 2016)); they also demonstrate the capability of the SFM-MVS approach to produce high resolution and high quality DEMs suitable for studies of Earth surface processes and landforms. There are many factors that affect elevation modelling results, some examples of reproducibility include comparisons of: SFM-MVS pipelines from different software (Ouédraogo et al., 2014; Dandois et al., 2015; Micheletti et al., 2015a; Smith et al., 2015; Stumpf et al., 2015); sensors/cameras (Dandois et al., 2015; Micheletti et al., 2015a), camera settings and calibration (Harwin et al., 2015; Clapuyt et al., 2016; James et al., 2017b), flight plans (James and Robson, 2014; Dandois et al., 2015; Smith and Vericat, 2015), the distribution of ground control (Clapuyt et al., 2016; Tonkin and Midgley, 2016; James et al., 2017a), different field sites (Dandois et al., 2015; Nolan et al., 2015; Bühler et al., 2016a; Harder et al., 2016); variable field site conditions (Harwin and Lucieer, 2012; Westoby et al., 2012; Dandois et al., 2015; Harder et al., 2016) and georeferencing approaches (Carbonneau and Dietrich, 2017).

Repeatability can be defined as how a measure varies for a particular sensor and involves conducting repeat measurements of the same object with the same sensor under similar conditions within a short period (Bartlett and Frost, 2008). That is, repeatability investigates what would be the expected variation in elevation measurement for a given UAV survey for a given camera, survey design and field site conditions. Using repeat observations for determining measurement precision is a well-known approach for assessing measurement uncertainty, but has yet to be commonly applied for DEMs, in particular for SFM-MVS DEMs. This study focuses on repeatability.

Throughout this section, we define several models that can be used to describe the distribution of DEM error. Each error model is based on a scenario that depends on the data collected or available for error analysis. These scenarios are, (i.) single DEM from an aerial survey with surveyed check points or a reference DEM; (ii.) multiple DEMs from repeat aerial surveys with surveyed check points; or (iii.) multiple DEMs from repeat aerial surveys with a reference DEM. The error models mathematically characterize and define the error components for each of these different situations and subsequently define estimators for the bias and precision. In doing so, we present characterizations of bias and precision that are allowed to vary spatially depending on the surveying scenario and thus data availability. The error models presented here are not meant to be a comprehensive list; we acknowledge that there are other approaches to error analysis of SFM-MVS DEMs such as those based on simulations (James et al., 2017b). Instead, we present the most commonly applied error model (i.e., i.) and demonstrate how we can afford more complex descriptions of error by providing additional repeat survey data (i.e., ii. and iii.).

The elevation value $y(x)$ of a surface (e.g. a SFM-MVS derived DEM) within domain D can be described as,

$$y(x) = z(x) + e(x) \quad (1)$$

where $z(x)$ is the 'true' elevation value and $e(x)$ is the measurement error at location x . Typically, $e(x)$ is determined by comparing $y(x)$ to a reference data set to represent $z(x)$ at a higher accuracy, where the number n of reference elevations $(z(x))_{x \in D}, i = 1, \dots, n$ can either be a set of check points, for example from a Global Navigation Satellite System (GNSS) survey, or elevations from another DEM (Kyriakidis et al., 1999).

3.1.2 Single DEM with check points or a reference DEM

The most common approach for describing measurement error in DEMs, both classically and within SFM-MVS studies, is the use of global statistical measures, such as root mean square error (RSME), mean error and the standard deviation (SD) of error at check point locations (Fisher and Tate, 2006; Wilson, 2010; Smith et al., 2015). These statistics describe the overall measurement error of a DEM and, given a spatially distributed set of reference data, can provide a visualization of spatial error patterns. Usually, these statistics are calculated for the scenario where a close-range aerial survey is used to produce a single SFM-MVS DEM to measure the elevations of a surface, and some sort of reference data has been collected.

We describe the measurement error $e(x)$ in this situation by decomposing it into a constant bias or systematic error, μ , and a random error, $\varepsilon(x)$:

$$e(x) = \mu + \varepsilon(x). \quad (2)$$

The random error in this conceptual model has a mean of 0 and standard deviation σ , and it is often observed or assumed to be normally distributed (Kyriakidis et al., 1999; Fisher and Tate, 2006; James et al., 2017b).

The standard deviation, or precision, is estimated as the standard deviation σ of measurement error, or the square root of the measurement error variance σ^2 ,

$$\sigma^2 = \frac{1}{n-1} \sum_{i=1}^n (e(x_i) - \hat{\mu})^2 \quad (3)$$

where $e(x_i)$ is the difference between the elevation surface and reference data, $y(x_i) - z(x_i)$, at locations for $x_i \in D, i = 1, \dots, n$. That is, the measurement precision is based on an estimate of the standard deviation of random errors calculated across all check points or all grid cells of a reference DEM. The estimate of the mean error or bias $\hat{\mu}$ is

$$\hat{\mu} = \frac{1}{n} \sum_{i=1}^n e(x_i) = \bar{y} - \bar{z}. \quad (4)$$

where \bar{y} and \bar{z} are the mean values of the DEM and the reference data height values, respectively, calculated from locations $x_i, i = 1, \dots, n$. The measurement error variance can therefore also be expressed as

$$\sigma^2 = \frac{1}{n-1} \sum_{i=1}^n ((y(x_i) - \bar{y}) - (z(x_i) - \bar{z}))^2. \quad (5)$$

Although this approach does provide quick statistics to summarize DEM error, it only provides limited insights into error distribution because, with a spatially constant $\hat{\mu}$ and σ^2 , it does not describe its spatial distribution (Fisher, 1998; Kyriakidis et al., 1999). The spatial distribution of errors can either be modelled through simulation (James et al., 2017b) or by obtaining more observations of the individual elevation values in a DEM.

3.1.3 Multiple DEMs from repeat aerial surveys with check points

By obtaining multiple DEMs from repeated aerial surveys, the DEM error can be described with more complexity by allowing precision to vary spatially across the entire DEM grid. That is, the random error corresponding to each DEM measurement (i.e. grid cell) can be characterized. We will demonstrate this in the case study presented in Section 3 of this paper.

The data available in this situation contains multiple overlapping DEMs representing p repeat measurements of the elevation surface, and each DEM is comprised of N elevation values $y_{(k)}(x_j), k = 1, \dots, p$, distributed throughout a grid $x_j \in D, j = 1, \dots, N$. Additionally, a set of check points $z(x_i), i = 1, \dots, n$, is available as reference data. In this situation, DEM error in the k^{th} DEM can be represented as,

$$e_{(k)}(x) = \mu + \varepsilon_{(k)}(x), \quad (6)$$

And we can now afford to allow the precision $\sigma^2(x)$ of $e_{(k)}(x)$ to vary spatially. Since the p repeat DEMs represent only a sample of all possible realizations of DEMs that could be generated using the same process, precision at a location x can now be estimated from the corresponding measurement error variance,

$$\hat{\sigma}^2(x) = \frac{1}{p-1} \sum_{k=1}^p (y_{(k)}(x) - \bar{y}(x))^2 \quad (7)$$

where $\bar{y}(x)$ is the mean elevation value averaged over all repeat DEMs. Compared to Equation 5, the reference elevation data has been replaced with the cellwise mean over all k DEMs from repeat surveys.

In terms of estimating bias, the general representation is similar as Equation 4; however, it can now be estimated from p repeat measurements at the n check point locations. As a result, the bias $\hat{\mu}$ is estimated as

$$\hat{\mu} = \frac{1}{np} \sum_{k=1}^p \sum_{i=1}^n e_{(k)}(x_i). \quad (8)$$

3.1.4 Multiple DEMs from repeat aerial surveys with a reference DEM

In addition to using repeat DEMs, having spatially continuous reference data or a reference DEM can further expand the complexity of the error description by allowing the bias to vary spatially continuous across the DEM grid. In this situation, the locations x_i of elevation values of the reference data and DEMs are the same, and therefore $n = N$. Here, we can afford to decompose DEM errors into spatially varying systematic and random components,

$$e_{(k)}(x) = \mu(x) + \varepsilon_{(k)}(x) \quad (9)$$

where the bias $\mu(x)$ can be estimated for each grid cell x as

$$\hat{\mu}(x) = \frac{1}{p} \sum_{k=1}^p e_{(k)}(x) = \frac{1}{p} \sum_{k=1}^p (y_{(k)}(x) - z(x)). \quad (10)$$

3.2 Data and methods

3.2.1 Study site and elevation surveys

This study was conducted for the surface of a snow-covered section of an active rock glacier in the Combe de Laurichard catchment, Écrins National Park, located in the southern French Alps at 45.01°N, 6.37°E (Figure 1). The rock glacier dynamics of this site have been monitored in detail for well over 30 years (Francou and Reynaud, 1992; Bodin et al., 2009), and it is currently being used as a test site for new methods for mapping rock glacier displacements based on airborne laser scanning, terrestrial laser scanning and SFM-MVS derived surface elevation models (Bodin et al., 2008).

Multiple (5) UAV surveys of the frontal part of the rock glacier were completed on the 22 February 2017 using a DJI Phantom quadcopter. The UAV survey covered an area of 0.04 km². These 5 flights all started within a 30-minute period (13:57 to 14:28) to maintain generally similar lighting between each surveyed set of images. Each flight was flown in parallel paths with the camera in a nadir position, with a 75% side and top overlap between images and a maximum flying speed of 9 m/s. The repeated flight paths were programmed using the MapPilot iOS app. This was a close-range survey with a flying height of approximately 60 m above ground level (agl). A feature within MapPilot allowed the flights to follow the terrain based on approximately 30 m × 30 m resolution Shuttle Radar Topography Mission (STRM) DEM, instead of being flown at a constant altitude above ground. A height of 60 m agl was selected to allow this study to investigate DEMs based on the highest image resolution that can be afforded while maintaining a safe distance above the terrain. All images were saved in JPEG format. Each flight recorded from 66 to 68 images.

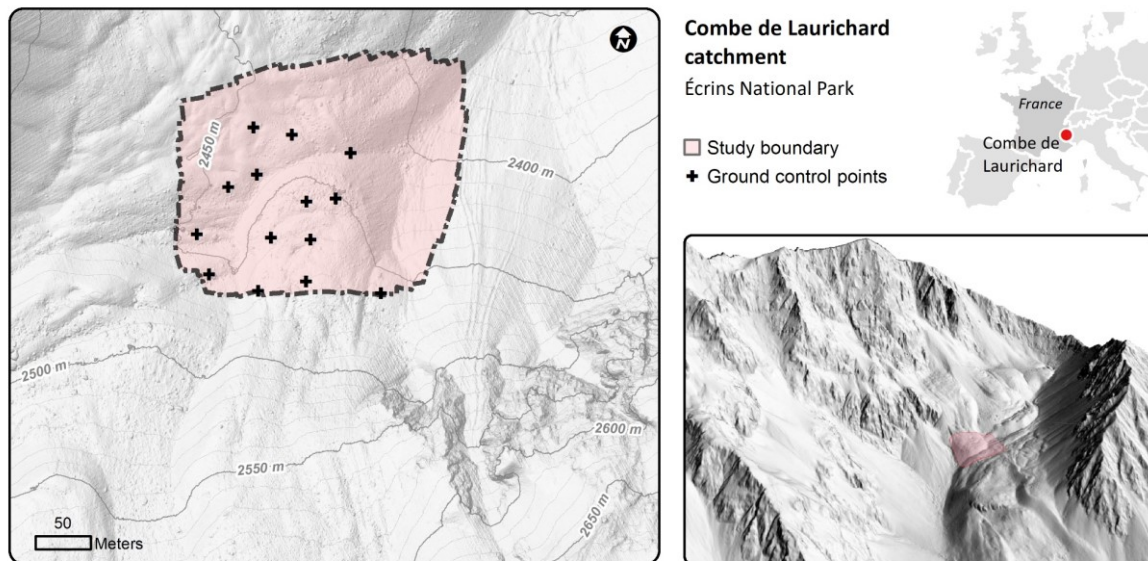


Figure 1. Location of the surveyed rock glacier in the Combe de Laurichard catchment including the extent of the study area and position of ground control points (i.e. artificial targets). The background topographic data is a hillshaded DEM derived from a terrestrial lidar survey performed in 2012 (data courtesy of *Station Alpine Joseph Fourier*, CNRS / Univ. Grenoble-Alpes).

The sky during the flights was cloud-free. The scene was predominantly snow-covered, with some areas of exposed boulders and rock debris (**Figure 2**). The snow cover had a strong texture, as the last snowfall in the catchment, recorded by the nearest meteorological station situated 2 km away (Col du Lautaret), was on the 8 February 2017, 14 days before the survey. This location is also popular among backcountry skiers, and had been marked up by ski tracks. The UAV images did contain shadowed areas, which grew larger with each flight as the sun sank from 32° to 30° in elevation and extended northeastwards as the sun also travelled from 200° to 208° in azimuth (**Figure 2**).

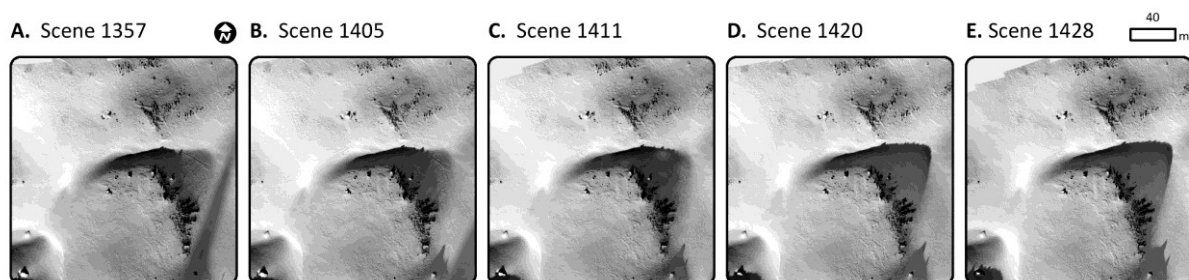


Figure 2. Orthomosaics of the snow covered landscape from the set of images obtained from each flight. These are the UAV surveyed scenes used for processing the DEMs (Table 2). The scene numbers correspond to the time each UAV survey began.

In addition to the UAV surveys, a survey of ground control points (GCPs), using artificial targets, and check points was collected from kinematic Global Navigation Satellite System (GNSS) measurements with a positional accuracy ≤ 2 cm (at 1σ). The penetration depth of the GNSS-receiver pole into the snow surface was recorded to adjust the observed GNSS vertical positions in post-processing to represent the elevations of the snow surface. This survey was used as the reference data for our study. In total, 14 GCPs and 106 check points were surveyed. All the check point measurements represent the elevation of the snow surface.

3.2.2 DEM processing and error estimation

The imagery from each flight was processed to produce its own DEM (5 in total). Agisoft's Photoscan software (version 3.12) was used to process the images into dense 3D point clouds based on its own SFM-MVS workflow. All camera (intrinsic and extrinsic) parameters were optimized, including an option for rolling shutter correction. Before camera parameters were optimized, tie-points with a reprojection error greater than 0.5 pixels were removed to reduce the reprojection error while maximizing the available number of tie points for model optimization. This optimization and georeferencing was also based on the set of surveyed GCPs. The alignment process was set to use high accuracy, and the dense point matching parameters were set to high quality with moderate depth filtering. The points cloud for each set of imagery was exported as a DEM with a 5 cm × 5 cm spatial resolution, and the grid cells between each DEM were aligned using the snap raster feature available in ESRI's ArcMap (version 10.5).

A grid of precision estimates was computed by calculating the standard deviation in elevation for each overlapping grid cell of the DEMs. This calculation follows the approach to spatial varying precision estimation described in Equation 7 using repeated UAV surveys and only check point data, not a reference DEM. It results in a raster data set illustrating the amount of variation in elevation between the multiple surveyed DEMs. Since in this study only a set of check points was available for reference data, bias was estimated using Equation 8: the difference between check point elevations and the mean elevations from overlapping data in the multiple DEMs. The result of the bias estimation is a set of points, corresponding to the locations of the check points, illustrating how much, on average per check point location, the DEMs differed from the reference data. Using the check points, the RMSE, mean absolute error (MAE), bias and standard deviation of error were also calculated for each DEM individually to summarize error using the basic non-spatial approach presented in Section 2.1.

3.2.3 Modelling the spatial distribution of precision

A generalized additive model (GAM) was selected to model the spatial distribution of estimated DEM precision. GAMs are an extension of generalized linear models that have the flexibility to represent the dependence of the response on linear or nonlinear predictors (Hastie and Tibshirani, 1990). The smoothing terms with the GAM were optimized based on generalized cross-validation (GCV) with a limit of 4 degrees of freedom to ensure model flexibility while still providing interpretable generalizations of variable trends within the model.

There is potentially an inexhaustible list of variables that might be useful for explaining the precision pattern. We decided to focus on variables that would hopefully provide some practical insight into their influences on precision, leading to improved methods for increasing precision. These predictors are based primarily on the sensor conditions and spatially varying image processing factors related to the scene. Therefore, we used image height, image count, image mean reprojection error, image saturation, and distance to GCPs. Additionally, landform slope angle was used as a variable to describe the relationship with terrain shape,

and a classification of shaded areas was used to assess precision varying with lighting conditions.

The variables for image height, count and mean reprojection error are based on the values of individual images used for the 3D reconstruction. The footprint boundaries of each image were projected onto the corresponding reconstructed elevation surface. These projected image boundaries were then each assigned the corresponding value related to the height the image was taken, and the mean reprojection error resulting from the image matching process. To summarize image height, count and mean reprojection error, for all scenes, the mean value was taken from an overlay of all the individual images. The mean reprojection error is a summary of the quality of tie-point matching within each image. It depends on the quality of the camera calibration and on the points within an image, which are related to the general image network (or image collection design; (James and Robson, 2014; James et al., 2017b).

Image saturation may provide a proxy of areas within a scene that are difficult to reconstruct because of a lack of information (i.e. over- and under-exposed areas), such as areas cast under shadow. Here, the maximum saturation based on an ortho mosaic for each scene was computed to represent the areas that had saturation problems across all scenes. The Red Green Blue (RGB) to Hue-Intensity-Saturation (HIS) image transformation in GRASS GIS (version 7.4) was used to calculate saturation for each orthomosaic.

Shaded areas were classified for each scene using a k -nearest neighbor (k -NN) algorithm applied to the RGB bands of the orthomosaics. The resulting classes of the k -NN classification were labeled as either shaded or unshaded areas. A map representing the shaded areas of all scenes was created by merging the shaded areas from each scene to a single grid. Distance to GCPs was based on computing the Euclidean distance to the nearest GCP within the DEM grid, and slope angle was based on the mean slope angle for each pixel across all scenes.

The relative importance of each of the variables in the GAM was also assessed to determine which variables were most important for characterizing the spatial variation in precision. An estimate of the proportion each variable contributed to explaining the deviance in the GAM was used to rank variable importance. A higher proportion of deviance explained indicates a higher rank.

Given the large data size (about 19 million grids cells per variable), a spatially random sample of 20 000 grid cells was used for the GAM. This sample was taken from an area that all DEMs managed to cover (the study boundary in **Figure 1**). This sample was also used to explore relationships between predictors and DEM precision.

3.3 Results

3.3.1 Spatial variation in precision

Overall, the median precision estimated from repeated DEM surveys for this study area was 0.03 m with an interquartile range (IQR) of 0.05 m (**Figure 3h** and **Figure 4**). The maximum and minimum precision was 0.001 m and 0.33 m, respectively.

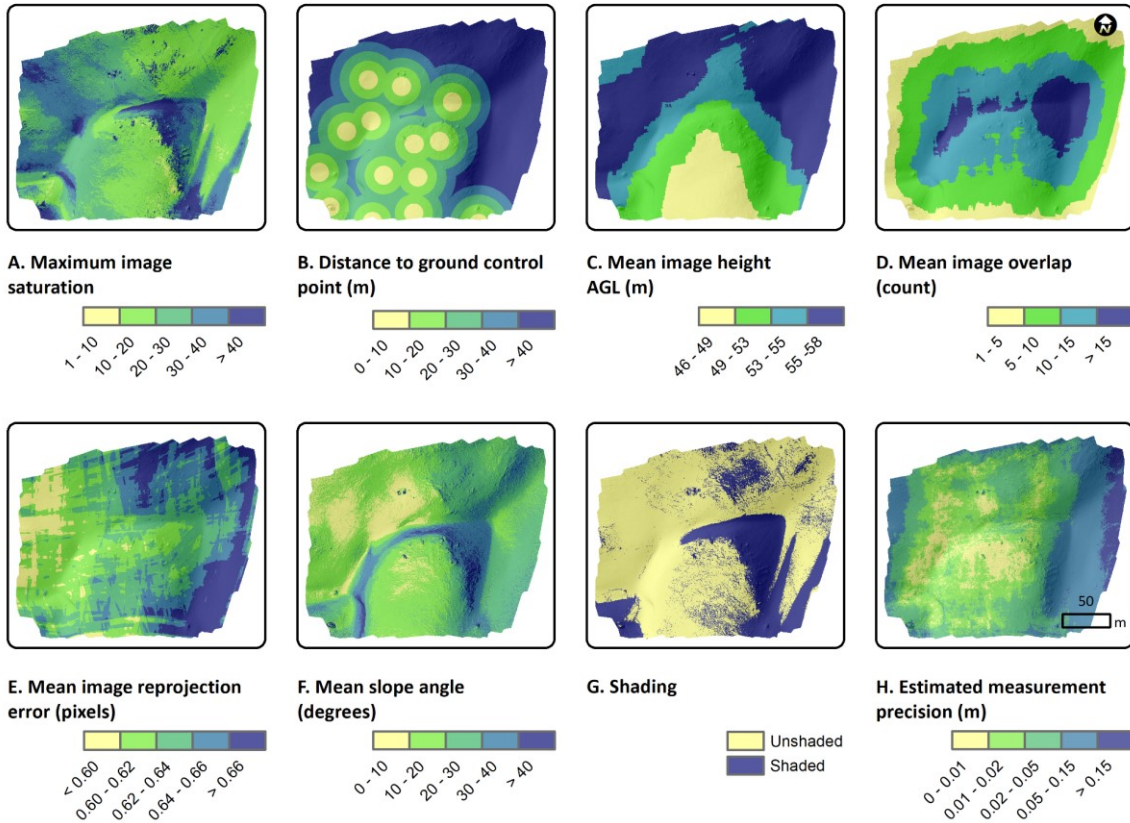


Figure 3. Maps of the distribution of values for each variable used for modelling precision (a-g), and map of DEM error calculated from standard deviation which represents the spatial variation in measurement precision ($\hat{\sigma}^2$ in Equation 7, calculated from repeat aerial surveys; h).

The deviance in precision explained by the GAM was 83%. Factors relating to survey design, such as image height and distance to GCPs were most important for modelling the spatial variation in precision, as estimated by the proportion of deviance explained (**Table 1**). Scene conditions such as saturation, slope angle and shading had relatively much less influence on precision characterization.

Some of the factors in the GAM illustrate well-defined trends, which characterize the spatial variation in precision (**Figure 5**). The modeled precision tends to lower when the distance to the nearest GCP is greater than 30 m, when image height is greater than 58 m, when slope was greater than 40°, and generally when the image reprojection error is higher. Modeled precision was also slightly lower for shaded areas.

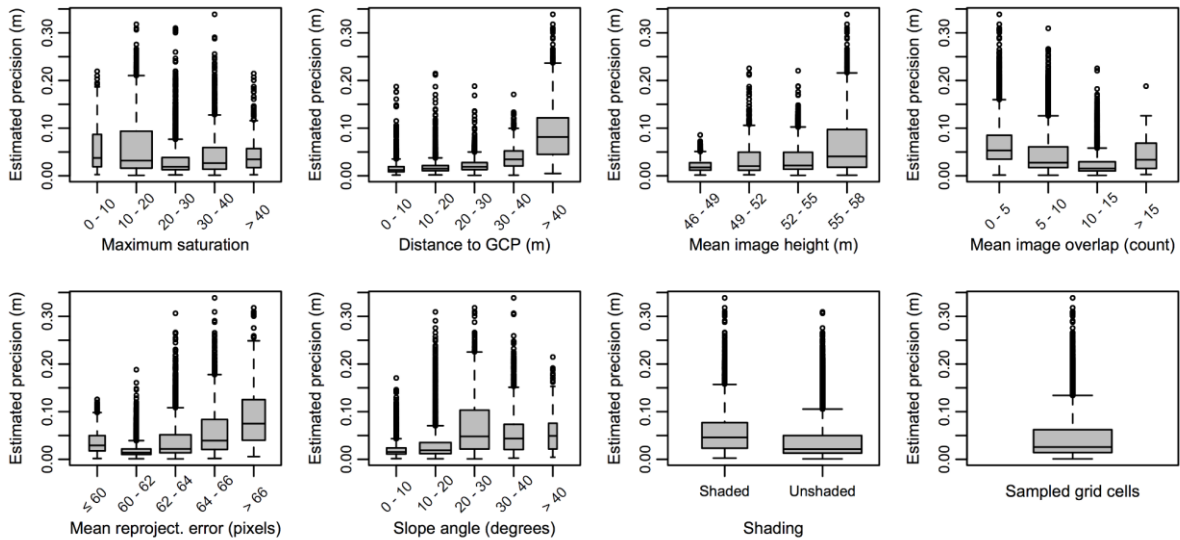


Figure 4. Box plots of measurement precision (SD in elevation per pixel) for classes of each variable used to model precision with the GAM. These observations are based on the sample used for the GAM. The width of each box plot is proportional to the size of the group.

Table 1. Estimated proportion of deviance explained by each variable in the GAM. The higher proportion indicates a higher contribution to spatial variation in DEM precision.

Variable in GAM	Proportion deviance explained
Mean image height	0.114
Distance to GCP	0.068
Mean image overlap	0.021
Mean reprojection error	0.014
Maximum saturation	0.006
Slope angle	0.004
Shading	0.003

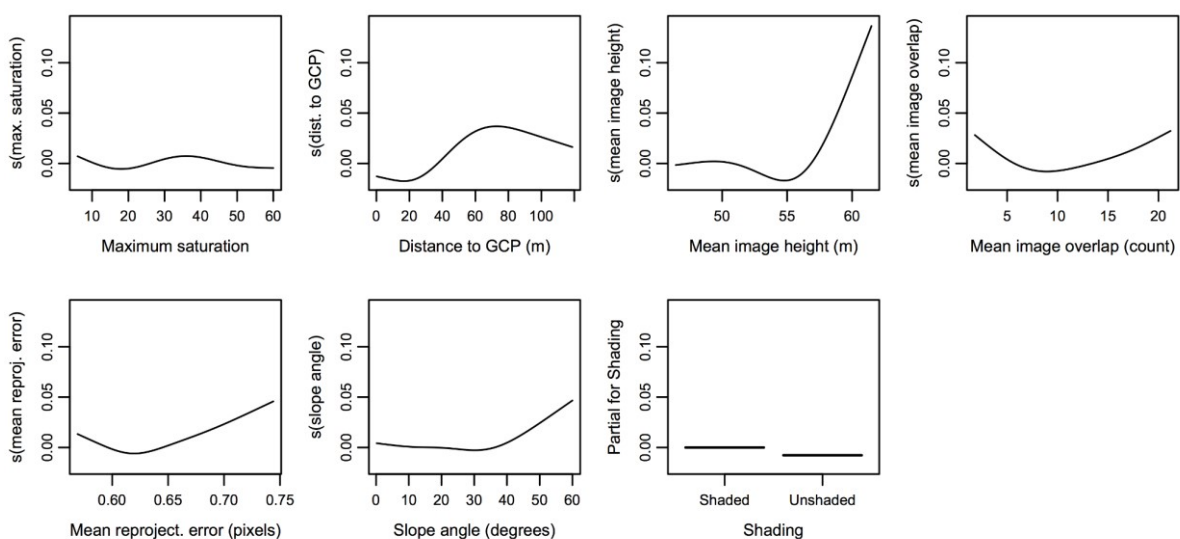


Figure 5. A spline function for non-parametric smoothing of the variables in the GAM.s

3.3.2 Estimated error

The mean RMSE estimated error for the DEMs was 0.050 m with a standard deviation of 0.003 m. The error ranged from -0.176 to 0.152 m between the DEMs (**Table 2**). The mean bias was -0.008 m with a standard deviation of 0.005 m, which may indicate that the global bias on average is close to zero when considering elevations measured from repeat DEM observations. The values of the overall root mean square (RMS) reprojection error for each scene ranged from 0.446 to 0.801 pixels. There is no indication that there is a clear relationship between the check point estimated error estimates and the RMS reprojection errors (**Table 2**).

Table 2. Global statistics describing error estimated from GNSS check points for each UAV surveyed DEM, and the root mean square (RMS) reprojection errors corresponding to the image alignment within each DEM scene.

DEM Scene	Time of image acquisition	RMSE (m)	MAE (m)	Bias (m)	Standard deviation of error (m)	Max. error (m)	Min. error (m)	RMS reproj. error (pixels)
1357	13:57	0.047	0.038	-0.010	0.046	0.111	-0.110	0.446
1405	14:05	0.050	0.039	-0.013	0.048	0.108	-0.118	0.768
1411	14:11	0.052	0.041	-0.002	0.052	0.152	-0.112	0.737
1420	14:20	0.047	0.038	-0.012	0.046	0.108	-0.103	0.402
1428	14:28	0.054	0.043	-0.004	0.055	0.135	-0.176	0.801

The spatial distribution of the estimated bias does not clearly show any pattern that would indicate a strong bias through the entire scene (**Figure 6**). There are some transects where the error seems to have a positive trend towards the edge of the scenes, but this error pattern is not consistent with all transects. There are also areas in the center of the scene where the check point transects show contrasting error results.

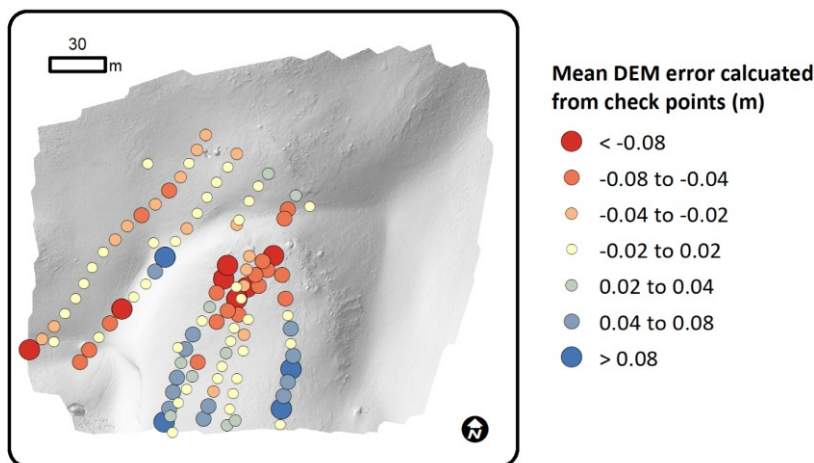


Figure 6. Bubble plot of estimated mean error between GNSS surveyed check points and SFM-MVS derived DEMs.

3.4 Discussion

3.4.1 Spatial variation in precision

Modelling the spatial variation in precision can provide us with insights on the major factors influencing precision, which can help improve sensor and image acquisition design, particularly for a site where SFM-MVS DEMs are key to monitoring changes in surface elevations.

Our model of the spatial variation in precision indicates that a GCP spacing of 30 m would help provide better precision across a SFM-MVS derived DEM for our given study area and survey design. Various optimal GCP spacings have been found in other studies. Both with image heights near 100 m agl, (James et al., 2017a) and (Tonkin and Midgley, 2016) found that a spacing of 50 and 100 m, respectively, was suitable for controlling DEM errors. In our model, distance to GCPs was also an important variable for explaining the spatial variation of precision. This finding provides further empirical support to previous studies that demonstrate the importance of a well-designed GCP network to mitigate errors related to the SFM-MVS approach to elevation modelling (James and Robson, 2014; Clapuyt et al., 2016; Tonkin and Midgley, 2016; James et al., 2017b).

The lowest precisions within the surveyed area were generally related to areas that had a poor distribution of GCPs (**Figure 4**). In general, lower elevation precisions can be attributed to imprecise GNSS surveyed GCP locations or a poor distribution of GCPs (James et al., 2017b). In the case where there is a well distributed GCP network and the precision of the GNSS surveyed GCP locations is high (i.e. centimeters scale), other factors such as the image network (i.e. location and distribution) may better characterize the spatial variation in precision (Bemis et al., 2014; James et al., 2017b). With our modelling approach, if the GCP network is strong, we may not observe a substantial influence of distance to GCPs for modelling precision within the GAM. This result may provide evidence that would suggest a good GCP network design; however, it may also lead to potentially underestimating the importance of the GCPs for future surveys at the same site. Methods of survey simulation (James et al., 2017a) or a comparison of SFM-MVS DEMs created with different GCP distributions (Clapuyt et al., 2016; Tonkin and Midgley, 2016) can be used to further investigate the influence of the GCP for a given study site.

The GAM also indicates that lower precision was generally associated with images taken from higher altitudes above ground, as well as where the number overlapping images was either relatively low or high (**Figure 5**). Image height and overlap have been established as strong factors that influence SFM-MVS DEM errors in previous studies (Bemis et al., 2014; James and Robson, 2014; Micheletti et al., 2015b). The maximum precision related to image overlap, show in the GAM plots of smoothed functions (**Figure 5**), may have been affected by the spatial distribution of precision influenced by the distribution of GCPs. A large portion of the area where image overlap was the highest was also where the GCP network was the poorest (**Figure 3**). This result may highlight that increasing image overlap alone cannot act as a substitute for having a well-distributed network of GCPs. The area of high image overlap was also related to areas where slope was generally the steepest (**Figure 3**). Thus, terrain conditions, such as slope, may have influenced the precision of the elevation models; however,

this effect was likely related to how terrain conditions may restrict the placement of GCPs due to problems of accessibility. It is also possible that since the images were taken at nadir, more images without different viewing angles may have produced worse auto-calibrated camera models by contributing more noise in the calibration procedure (Bemis et al., 2014; James and Robson, 2014). We attempted to ensure that the image height was stable above our surveyed object (i.e. the rock glacier) by designing the UAV surveys to follow the terrain at constant height above ground level based on approximately 30 m spatial resolution SRTM data. However, an even height above ground may be challenging to maintain since SRTM data in high-mountain areas is prone to lower vertical accuracies (Berthier et al., 2006). Therefore, there may be inconsistencies between the actual ground elevation and the SRTM data, which in the case of our UAV survey design would result in having some areas under- or overestimating the actual altitude above ground level. As our results illustrated, precision tends to deteriorate as the images are taken from higher heights (**Figure 5**); typically, higher flying heights result in a deterioration in elevation model accuracy (Smith and Vericat, 2015). Thus, relatively lower precision of SFM-MVS derived elevation models can occur in areas where the actual flying height of the UAV is higher than the desired programmed height above ground level.

Image reprojection errors have been found to be closely related to the spatial variation in SFM-MVS elevation model precision (James et al., 2017b). It was observed in our model that precision generally decreased with higher mean reprojection errors. However, we also observed that the lowest mean reprojection errors were associated with areas of lower precision in the eastern edge of our study (**Figure 3** and **Figure 5**). We conjecture that this may be due potential biases related to how mean reprojection error is calculated. A very low mean reprojection error may indicate a good local camera model that is overfitting. That is, it does not apply well throughout the entire reconstructed scene. Local overfitting can occur when few images with little variation in viewing angle are used for camera model calibration, which was the case for our observed area of low reprojection error (**Figure 3d**). UAV flight designs to mitigate the issue of producing only good local camera models can be found in James and Robson, 2014).

Factors related to field site conditions, such as lighting (saturation and shading) and terrain (slope), were the least effective at explaining the spatial variation in precision. We did however observe that precision deteriorated with increasing landform slope angle. Steep slopes are more susceptible to horizontal shifting errors between DEMs. Also, steep areas may be more affected by shadows. Poor lighting conditions in general can have negative effect on the quality of the SFM-MVS model (Bemis et al., 2014). Perhaps, the low contribution to predictive performance is due to the spatial scarcity of these variables throughout the scene. That is, they do not occur throughout most of the scene, since we had generally good lighting conditions during the UAV surveys conducted for this study.

3.4.2 Investigating measurement bias

The approach for estimating error by comparing DEM values to reference data is adequate when the measurement accuracy of the reference data far surpasses that of the technique to derive the DEM. However, when the measurement accuracy of the DEM approaches that of the reference data, such as is the case with SFM-MVS DEM, which is producing sub meter to decimeter accuracies (e.g. (Carrivick et al., 2016; Clapuyt et al., 2016), caution should be taken. The errors corresponding to the reference data may propagate into the estimation of DEM errors, which may contribute to an inaccurate knowledge of the distribution of errors. In our study, we may have observed just that. It appears that there may have been biases in the GNSS survey, since adjacent and nearly parallel transects showed different patterns of error (**Figure 6**). Error in the GNSS survey data may be related to the challenges of surveying the snow surface elevations. As mentioned in the methods, we would record the depth of the GNSS antenna pole into the snow to correct for the height of the snow surface. However, it is possible that some of the observed depths of the antenna pole were inaccurately observed.

Measurement bias can be much better explained by a comparison to spatially continuous reference data, such as a laser scanning derived DEM (Favalli et al., 2012; James and Robson, 2012; Westoby et al., 2012; Smith and Vericat, 2015). Laser-scanning data has become an established approach for high density and resolution surveying (Wilson 2010), and as a result it has provided valuable insights on the systematic errors associated with the SFM-MVS techniques (James and Robson, 2014; Javernick et al., 2014; Smith and Vericat, 2015; Brunier et al., 2016; Carbonneau and Dietrich, 2017). In this paper, we have provided a model to describe error that when given repeat DEMs could potentially provide a more confident estimate of how DEM error may vary spatially by allowing for multiple elevation observations (or realizations).

Having reference data based on laser scanning is still one of the best options for investigating DEM measurement bias. However, in general, obtaining laser scanning reference data to characterize the errors in SFM-MVS elevation models may not only be difficult due to cost, equipment or timing constraints, it may also not be practical from an operational point of view (Smith et al., 2015). Reference data collected from GNSS surveys is much more feasible for error analysis of SFM-MVS elevation models, especially considering that GNSS surveyed ground control points (GCPs) are usually required for georeferencing and controlling systematic errors (James and Robson 2014; James et al. 2017b). For these reasons, we have provided and demonstrated within this study an error model that allows for spatial variation in error based on check points and repeat DEM observations.

3.5 Conclusion

Overall, mapping the distribution of precision can provide better confidence in our observations than using traditional error assessments such as the global RMSE statistic. In this study, we had presented several approaches to describing DEM error depending on the data available for model validation. In the case of having multiple DEMs from repeated surveys, we can characterize spatial variations in DEM precision. This spatial estimate of error from

repeat DEMs can provide stronger support of the elevation model quality than from a single DEM observation.

For our study, factors related to SFM-MVS survey design were the strongest at characterizing the spatial variation of precision: image height and distribution of GCPs were the strongest. The factors relating to the field conditions, such as shading and slope steepness had only a slight influence on the spatial variation of precision.

We would recommend our approach as an excellent starting ground for designing and conducting pilot studies for monitoring changes in surface elevations. Much investment goes into monitoring, especially in remote areas, which is why investigating the precision of a particular sensing approach is critical to ensure we obtain quality data from our efforts.

3.6 Acknowledgements

We would like to thank the Parc national des Écrins and the Joseph Fourier Alpine Research Station (SAFJ) for their support, and everyone who assisted us in the field.

The National Sciences and Engineering Research Council (NSERC) of Canada through an Alexander Graham Bell Graduate Scholarship awarded to J. Goetz and funding from the Carl Zeiss Foundation awarded to A. Brenning have supported this research.

Chapter 4

Quantifying uncertainties in snow depth mapping from structure-from-motion photogrammetry in an alpine area

Abstract

Mapping snow conditions in alpine areas is crucial for monitoring local hydrology to support water resource management decisions. Recently, the use of structure-from-motion multi-view stereo (SFM-MVS) 3D reconstruction (or SFM photogrammetry) to derive high-resolution digital elevation models (DEMs) has become popular for mapping snow depth in alpine areas. In this study, methods for communicating the uncertainty in snow depth calculated from SFM-MVS derived DEMs are presented using a case study in the French Alps. A spatially varying snow depth precision estimate was determined using an error propagation model based on the precision of the acquired SFM-MVS DEMs, which was obtained from repeated unmanned aerial vehicle (UAV) flights. Spatially varying snow depth detection limits were determined using Student's *t* distribution. Additionally, the effect of the spatial resolution on the snow depth accuracy was explored. It was found that snow depths as shallow as 1 cm to 5 cm could be detected with high confidence for most of the study area. A map of the snow depth detection threshold was also found useful at identifying areas with high uncertainties, such as changes in topography or a systematic error caused by poor SFM-MVS reconstruction. It was additionally found that the spatial resolution of the snow-free conditions had a stronger effect on the snow depth accuracy than the snow-covered DEM. This result suggests that high-accuracy snow depths can be achieved by combining a detailed snow-free DEM with a lower-resolution snow-covered DEM, as obtained by satellite photogrammetry or a high-altitude above the ground UAV survey.

4.1 Introduction

Snow is an important water resource in many mountain regions around the world. A warmer climate can effectively reduce the water availability in these snow-dominated regions (Middelkoop et al., 2001; Barnett et al., 2005; Lemke et al., 2007). Therefore, given the changing climate, accurate monitoring and prediction of seasonal snow accumulation play key roles in water resources management. Accurate knowledge of snow accumulation can also help us improve our understanding of environmental processes in mountain areas including changes in ground temperatures (Luetschg and Haeberli, 2007; Apaloo et al., 2012), permafrost creep (Ikeda et al., 2008; Delaloye et al., 2010), avalanches (Bühler et al., 2011), rockfalls (Haberkorn et al., 2016), landslides (Matsuura et al., 2003; Okamoto et al., 2018) glacier dynamics

(Immerzeel et al., 2014; Rossini et al., 2018), and vegetation growth (Jonas et al., 2008). Additionally, high-resolution snowpack data can be used as reference data to test the accuracy of satellite remote-sensing products (Tinkham et al., 2014; Marti et al., 2016).

In the past two decades, lidar (light detection and ranging) has been a major source of high-resolution snow depth mapping, with accuracies typically in the decimeter range (Deems et al., 2006; Prokop, 2008; Schaffhauser et al., 2008; Deems et al., 2013). It has helped improve our understanding of the spatial distribution of seasonal snow accumulation (Deems et al., 2006; Helfricht et al., 2012; Kirchner et al., 2014; López-Moreno et al., 2015), and it has also improved snowpack modelling by integrating lidar derived snow depths into physically-based models (Revuelto et al., 2016; Hedrick et al., 2018).

There have been recent developments for high-resolution snow depth mapping in mountain environments using digital photogrammetry. Bühler et al. (2015) demonstrated that airborne stereo optical imagery can produce snow depth maps with 2 m spatial resolution and a root mean squared error (RMSE) of 30 cm. Marti et al (2016) demonstrated the potential of stereo satellite imagery for snow depth mapping. They obtained decimeter accuracies using Pléiades high-resolution optical imagery, also with a 2 m spatial resolution. There were earlier attempts to use photogrammetry to map snow depth (Cline, 1993, 1994), but due to technical limitations at the time, it was difficult to produce accurate snow depth maps.

In addition to lidar and digital photogrammetry, the use of structure-from-motion multi-view stereo (SFM-MVS) 3D reconstruction (also known as SFM photogrammetry) for high-resolution snow depth mapping has become popular. In general, SFM-MVS can create a 3D reconstruction of a surface using a collection of images taken from different viewing angles (Snavely et al., 2006). When SFM-MVS techniques are applied for topographic analysis, they can be used to produce high-resolution digital elevation models (DEMs) of Earth's surface (James and Robson, 2012; Westoby et al., 2012; Fonstad et al., 2013). Like lidar and digital photogrammetry methods, SFM-MVS derived snow depth maps are computed by differencing two co-registered elevation models acquired for snow-covered (snow-on) and snow-free (snow-off) conditions. Reported snow depth RMSEs typically range between 7 cm to 30 cm (Nolan et al., 2015; Vander Jagt et al., 2015; Bühler et al., 2016a; Harder et al., 2016; Adams et al., 2018; Avanzi et al., 2018).

Although SFM-MVS derived snow depth maps have shown promise to obtain frequent observations of snow distribution with a high spatial resolution, as with the other techniques, there are challenges to produce reliable and accurate data. These challenges are related to uncertainties inherent in elevation differencing, which are controlled by the elevation models' quality (Wechsler and Kroll, 2006; Wheaton et al., 2010) and co-registration accuracy (Nuth and Kääb, 2011; Marti et al., 2016; Bernard et al., 2017; James et al., 2017b). Understanding and quantifying the uncertainties in elevation model differencing can help us differentiate the computed surface change observations from noise (Wheaton et al., 2010). Or in the case of mapping snow distribution, it can help us determine detection limits of the computed snow depths.

Calculating the propagation of elevation model errors is typically used for estimating the uncertainty when analysing surface changes (Brasington et al., 2000; Lane et al., 2003; Wheaton

et al., 2010; James et al., 2017b). Uncertainties in SFM-MVS-derived elevation models are usually assessed by a comparison with a spatially distributed set of reference data, typically acquired using a lidar, differential/kinematic Global Navigation Satellite System (GNSS) or total-station survey data (James and Robson, 2012; Westoby et al., 2012; Smith et al., 2015; Goetz et al., 2018).

The quality of the SFM-MVS-derived elevation models for snow depth mapping depends on site conditions (Nolan et al., 2015; Bühler et al., 2016b; Harder et al., 2016; Cimoli et al., 2017; Gindraux et al., 2017), survey design (James and Robson, 2014; Tonkin et al., 2014; Smith et al., 2015; Piermattei et al., 2016; James et al., 2017a; Goetz et al., 2018) and the data processing pipeline (Ouédraogo et al., 2014; Micheletti et al., 2015b; Cimoli et al., 2017). Currently, a major limitation of the SFM-MVS techniques for mapping snow depth is that it is difficult for feature matching algorithms to perform well with images having a weak image texture, such as in the smooth-homogeneous surface caused by fresh snow cover (Bühler et al., 2016a; Bühler et al., 2016b; Gindraux et al., 2017). However, image acquisition over weathered snow surfaces can produce good results for SFM-MVS elevation models (Vander Jagt et al., 2015; Bühler et al., 2016b; Michele et al., 2016), even if the fresh snow has been exposed to sunlight for only a day (Gindraux et al., 2017).

An additional challenge unique to mapping snow depth using elevation differencing, is accounting for changes in the surface topography beneath the snow cover that may occur over time. For example, seasonal erosion of the surface (Bernard et al., 2017; Avanzi et al., 2018), frost heave (Nolan et al., 2015), vegetation compression (Nolan et al., 2015), and permafrost creep [Goetz *al* 2018- *submitted*] can cause errors in the computed snow depths. In the case of monitoring snow accumulation on glaciers, glacier surface lowering due to ice or snow melt and ice flow can also lead to errors (Gindraux et al., 2017).

The purpose of this paper is to spatially characterize uncertainties in snow depths computed from SFM-MVS-derived elevation models in an alpine area. This study's approach utilizes repeated unmanned aerial vehicle (UAV) surveys and in-situ field survey data taken during both snow-on and snow-off elevation model acquisition dates to spatially determine the precision of the derived snow depths and a spatially varying snow depth detection limit. Additionally, an analysis is conducted to investigate the effect of scale (i.e., spatial resolution of the DEMs) on snow depth accuracy.

4.2 Materials and Methods

4.2.1 Study site and data collection

This study was conducted in the Combe de Laurichard (45.01°N, 6.37°E, 2500 m a.s.l.), which is located in the French Alps near the Col du Lautaret. The snow depth in the area of an active rock glacier was mapped, the Laurichard rock glacier, to test SFM-MVS methods in complex mountain topography. The rock glacier surface is generally composed of large angular boulders and debris formed from densely fractured granite (Bodin et al., 2009). The survey area (~240 m × 210 m) contains the front of a tongue-shaped rock glacier showing compression features such as transverse ridges and furrows. Throughout this paper, the rock glacier area is

referred to as active terrain. The stable terrain, which is adjacent to the rock glacier front, has a hummocky topography that contains dense and sparse clusters of large boulders and debris, as well as low vegetation cover.

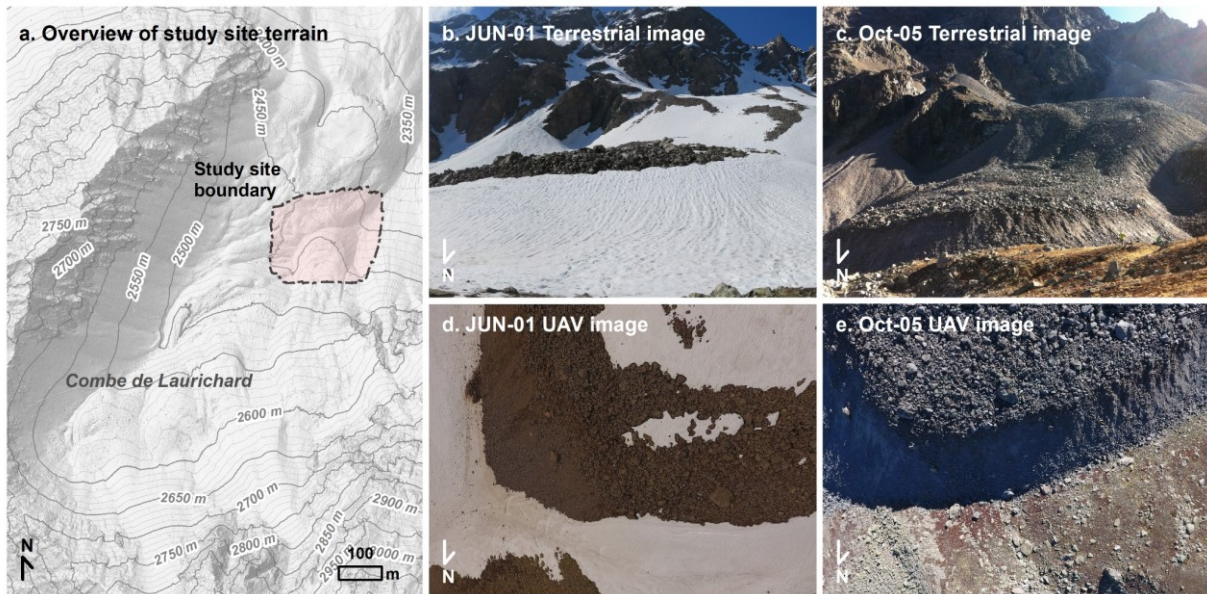


Figure 7. A terrain map illustrating the study site and UAV surveyed area (a). Ground-based (b,c) and UAV (d,e) images of the rock glacier taken on the survey dates in 2017.

Aerial imagery acquired from UAV flights for SFM-MVS processing and ground-based measurements were collected on June 1st and October 5th, 2017. The June date corresponds to the snow-on conditions during the melt period, and October 5th was the snow-off date required for computing snow depth (**Figure 7**). During the survey on June 1st, the study area was partially snow covered. The snow had a strong texture due to formation of suncups and surface runoff patterns. The UAV flights were flown in cloud-free conditions with air temperature ranging from 2 to 10°C. On October 5th, the study area was entirely snow-free. The flights were flown in mainly cloud-free to partially cloud-covered conditions, and the air temperature ranged from 7 to 16°C.

Repeated UAV surveys were performed on each date to obtain multiple DEMs representing the surface heights. These surveys were conducted using a DJI Phantom 4 quadcopter that was programmed to fly autonomous missions with the Map Pilot app for iOS devices. Each survey was programmed to fly in parallel flight paths with a maximum speed of 7.1 m/s, and to fly above the terrain at 60 m above ground level; the terrain model is based on the Shuttle Radar Topography Mission (SRTM) 1 Arc-Second Global elevation data. The optical imagery (RGB) was acquired at nadir position with a 75% side and top overlap. A shutter-priority mode with a set aperture of f/2.8 and ISO of 100 was used to take the images, which were saved in JPEG format. Artificial targets spread across the study area were used as ground control points (GCPs).

Reference data and the position of the GCPs were surveyed using Real-Time-Kinematic (RTK) GNSS measurements. The errors in the SFM-MVS derived snow-on and snow-off DEMs were determined from surveyed checkpoints of surface heights, which depending on the date,

include the height of snow-covered and/or snow-free surfaces. During the snow-on date, snow-probe measurements were taken at each checkpoint location using an avalanche snow probe with a maximum depth of 3 m. These probed snow depths were used to measure errors in the SFM-MVS-derived snow depths.

Due to the changing topography of the snow-covered surface, the location of the GNSS base station was different during survey dates. To improve the quality of the RTK GNSS measurements, the data was post-processed using GNSS data from the PUYA reference station, which is located approximately 19 km from the study area. The positional accuracies of the RTK GNSS surveys were ≤ 2 cm at 1σ . The spatial reference of this study was based on the RGF93 / Lambert-93 projection and the NGF-IGN69 vertical datum (EPSG::5698). The positional accuracy of the GNSS was relied on for co-registration of the snow-free and snow-on DEMs. There were no shared GCP targets between the snow-on and snow-off DEMs. The co-registration of the DEMs relied solely on the accuracy of the georeferencing based on the RTK-GNSS surveyed GCPs. There were no shared GCP targets between the snow-on and snow-off DEMs. This condition was tested to determine what snow depth accuracies may be achievable when snow-free areas are not available for co-registration, which can be the case in this study area during peak accumulation or after recent snowfall.

Table 3. Summary of UAV flights used to derive SFM-DEMs for computing snow depth.

Date	No. of flights	No. images / flight	No. GCPs	Avg. flying height (m)	Coverage area (km ²)	RMS reproj. error (pixels)	Vertical error from GCPs (cm)
Jun-01	6	67-77	19	59 - 62	0.056 – 0.061	0.48 – 0.70	1.8 – 2.5
Oct-05	7	92-121	13	62 - 67	0.078 – 0.090	0.44 – 0.51	1.9 – 3.9

4.2.2 DEM processing and computing snow depths

The UAV imagery for each flight was processed using Agisoft's Photoscan (version 1.4.2) for deriving SFM-MVS DEMs. The photos were aligned using a high accuracy with a key point limit of 40,000, a tie point limit of 4000, and the option for adaptive camera model fitting selected. All intrinsic and extrinsic parameters were optimized. Before optimization, the sparse point cloud was filtered by removing points that had a reprojection error > 0.5 , a projection accuracy > 3.0 , and reconstruction uncertainty level > 10 . Georeferencing and optimization of camera parameters were based on the surveyed GCPs. The dense points matching quality parameter was set to mild. The dense point clouds were exported as DEMs to the software-suggested spatial resolution (< 5 cm). All DEMs were resampled to the same $5 \text{ cm} \times 5 \text{ cm}$ spatial resolution grid format using bilinear interpolation. The elevation surface for each surveyed date was represented by a mean DEM, which was determined by calculating the mean elevation, \bar{y} , for each grid cell from the corresponding repeat DEMs. Snow depths were computed by subtracting the mean elevations, $\bar{y}_{\text{on}} - \bar{y}_{\text{off}}$, of the mean snow-on and snow-off DEMs.

4.2.3 Mapping snow depth uncertainties

A spatially varying uncertainty, σ_d , or precision in the SFM-MVS snow depths can be expressed by estimating the standard deviation of the propagated error for each grid cell,

$$\sigma_d = \sqrt{\sigma_{\text{on}}^2 + \sigma_{\text{off}}^2}, \quad (11)$$

where σ_{on} and σ_{off} are measures of uncertainty for the snow-on and snow-off DEMs, whose errors are assumed to be independent. Calculating the propagated error standard deviation for DEM differencing is often applied to estimate the uncertainties in topographic change detection (Brasington et al., 2000; Lane et al., 2003; Wheaton et al., 2010; James et al., 2017b). Similar to Goetz et al. (2018), the uncertainty or precision in the DEMs was estimated by calculating the standard deviation σ in elevation for each grid cell from the repeatedly acquired SFM-DEMs (Table 3). The root mean squared error (RMSE) was used to determine the accuracy of the DEMs and the snow depths from the GNSS-surveyed validation data. The errors in the DEMs were also characterized by terrain cover: snow cover, fine debris, or rocky debris. The snow depth errors were estimated for stable terrain and active terrain (i.e. on the active rock glacier).

In addition to mapping the precision of the SFM-MVS snow depths, the uncertainty in differencing DEMs can be expressed using the minimum level of detection (LoD) for a given confidence level based on estimates of DEM precision (Brasington et al., 2003; Lane et al., 2003; Wheaton et al., 2010). Since in this study there are repeat observations of the snow-on and snow-off DEMs, the detection limit was expressed as the margin of error corresponding to a one-sided confidence interval using a critical t -value. That is, for determining a minimum level of snow depth detection, we are mainly concerned if the SFM-MVS snow depths are greater than 0, in this case at a 95% confidence level. In earth sciences (Borradaile, 2002), including topographic change detection studies (Brasington et al., 2003; Wheaton et al., 2010; Lague et al., 2013; James et al., 2017b) a 95% confidence level is usually applied. The minimum detected snow depth was determined by,

$$\text{LoD}_{95\% \text{ CL}} = t_{\text{df}}^* \times \sqrt{\frac{\sigma_{\text{on}}^2}{n_{\text{on}}} + \frac{\sigma_{\text{off}}^2}{n_{\text{off}}}}, \quad (12)$$

where, σ_{on} and σ_{off} are estimates of the standard deviations of the snow-on and -off elevations based on repeat DEM observations, n_{on} and n_{off} are the corresponding number of DEMs used for finding \bar{y} and σ , and t_{df}^* is the (one-sided) critical t -value for the given degrees of freedom, df. These are calculated for each grid cell as,

$$\text{df} = \left(\frac{\sigma_{\text{on}}^2}{n_{\text{on}}} + \frac{\sigma_{\text{off}}^2}{n_{\text{off}}} \right)^2 / \left(\frac{1}{n_{\text{on}}-1} \left(\frac{\sigma_{\text{on}}^2}{n_{\text{on}}} \right)^2 + \frac{1}{n_{\text{off}}-1} \left(\frac{\sigma_{\text{off}}^2}{n_{\text{off}}} \right)^2 \right). \quad (13)$$

4.2.4 DEM resolution and snow depth accuracy

To gain some insight on how these methods could be scaled for application to larger areas, we performed an exploratory analysis on how the spatial resolution of the DEMs can affect the

accuracy of the snow depth measurements. That is, we use the spatial resolution as a proxy for performing higher altitude UAV surveys that can result in coarser resolution DEMs (i.e., ground sampling distance). Three scenarios were tested: (1) the snow-on DEM was resampled to coarser spatial resolutions, (2) the snow-off DEM was sampled to coarser spatial resolutions, and (3) both DEMs were sampled to coarser spatial resolutions. The snow depth accuracy (RMSE) was determined for resolutions from 0.05 m to 10.00 m with a step of 0.05 m. Coarser resolutions were obtained by aggregating the original 0.05 m resolution DEMs using the mean elevation values. For the individual comparison of the snow-on and snow-off DEM resolutions (scenarios 1 and 2), the aggregated DEMs were resampled to a 0.05 m resolution using bilinear interpolation.

4.3 Results

4.3.1 DEM accuracy and precision

The relatively smoother snow-covered DEM surface heights had a higher accuracy than the snow-free areas (**Table 4**), which was predominantly made up of exposed rock debris. Also, the DEM measured surface heights were more accurate for the smoother fine rock debris areas than the rougher rock-debris surfaces such as found on the rock glacier. The overall accuracy, measured by the RMSE, of the DEMs ranged from 7 cm to 9 cm.

The distribution of DEM errors for the snow-off DEM was generally spatially heterogeneous (**Figure 8b**). That is, there was no clear sign of strong systematic error in the elevation surface where the GNSS validation data was sampled. However, there was a cluster of over-estimated elevations in the north-west area of the snow-on DEM (**Figure 8a**). This elevation measurement bias was occurring outside of an area enclosed by the GCPs, and where the precision was relatively good (< 2 cm; **Figure 8c**).

The precision of the DEMs was lower where the terrain surface was rougher (i.e., rocky debris cover), further away from ground control, and at the smoothly textured snowdrift located in the south-west area of the snow-on DEM (**Figure 8c**). The precision throughout the DEMs was mainly less 2 cm. The distribution of precision values was spatially more heterogeneous in the snow-off DEM than the snow-on DEM.

Table 4. Accuracy of DEMs calculated from GNSS surveyed checkpoints. June represents the snow-on DEM, and October the snow-off DEM.

Mean DEM	No. obs.	RMSE (cm)	Mean (cm)
June (<i>overall</i>)	177	8.7	2.1
<i>Snow cover</i>	106	6.5	0.3
<i>Rocky debris cover</i>	71	11.3	4.8
October (<i>overall</i>)	141	7.4	1.5
<i>Fine debris cover</i>	38	3.8	2.0
<i>Rocky debris cover</i>	103	8.4	1.3

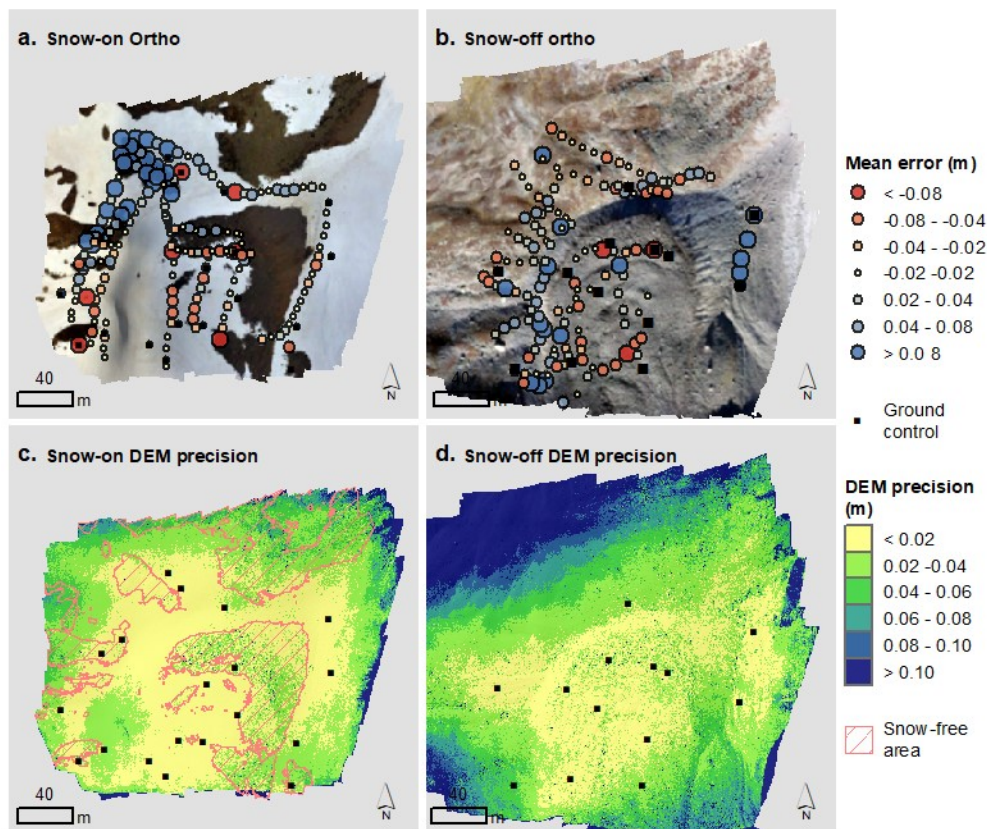


Figure 8. Bubble plots of GNSS measured accuracies and orthomosaics obtained from UAV imagery (a,b). Maps of DEM precision calculated from repeat DEM observations (c,d).

4.3.2 SFM-MVS snow depth uncertainty

The overall RMSE of the snow depths was 15 cm (**Table 5**). The stable terrain had a higher accuracy (RMSE = 12.2 cm) than the active terrain (18.2 cm). Based on the snow-probe measurements, the snow depths were on average underestimated. However, this may be a result of a measurement bias related to snow-probing – the suncups made it difficult to determine the height of the snow to the nearest cm. Snow depths that were also computed in the snow-free areas located in the north-east part of the scene show an increasing trend in depth towards the boundary of the study area. This trend may be an indication of where an overestimation in snow depth occurred due to a bias in the snow-on DEM, which was identified with the GNSS measurements. The precision of the SFM-MVS snow depths was less than $\sigma = 4$ cm for most of the study area (**Figure 9**).

Table 5. SFM Snow depth accuracy based on snow-probed observations calculated for the entire area (overall), active terrain (i.e. on the rock glacier) and stable terrain.

Terrain	No. obs.	RMSE (cm)	Mean (cm)	Std. dev. (cm)	Median (cm)	IQR (cm)
<i>Overall</i>	80	15.2	-3.6	14.8	-2.4	17.3
<i>Stable</i>	44	12.2	-1.0	12.3	-1.9	12.3
<i>Active</i>	36	18.2	-6.7	17.2	-10.3	26.2

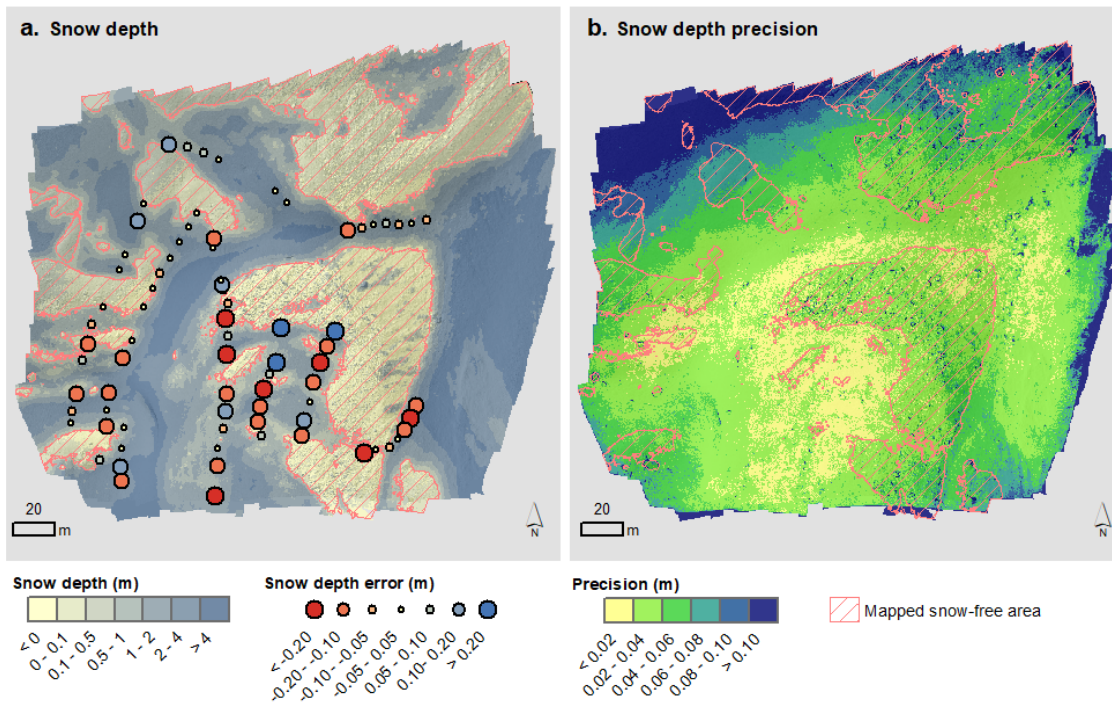


Figure 9. SFM Snow depth map and bubble plot of snow depth accuracies based on snow-probed observations (a), and an SFM snow depth precision map (b).

At a 95% confidence level, most of the study area had a detection limit between 1 cm to 5 cm – the median detection limit was 3 cm (**Figure 10** and **Figure 11**). The minimum detectable snow depth ranged from 0.2 cm to 194 cm. The snow depths in most of the study area were significantly detected. A comparison of the mapped snow-free areas to the areas that were lower than the snow depth detection limit shows possible uncertainties in the computed snow depths (**Figure 10**). For example, areas that should be below the detection limit because they are snow-free were not (**Figure 10e**). This is the same area that was overestimated in the snow-on DEM (**Figure 8a**) and may indicate that there was also a bias in the estimated snow depths surrounding this area. On the active rock glacier, there was a mismatch between the mapped-snow free areas and the ones detected by the threshold limit (**Figure 10cd**), which can be an indication of a change in the bare-ground topography between the snow-on and snow-off DEM acquisition dates.

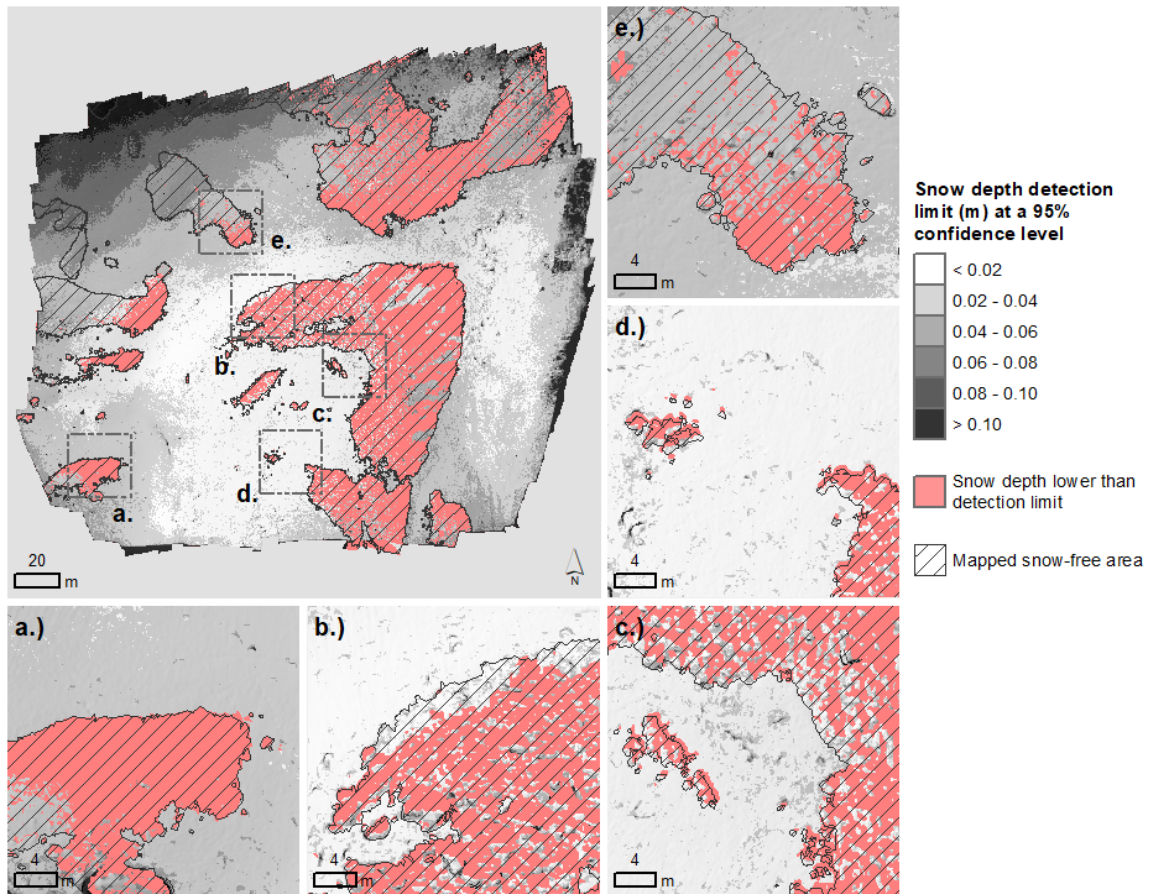


Figure 10. Areas where the SFM-MVS snow depth level was determined to be significant based a t-test applied for each grid cell at a 0.05 significance level. The snow-free area was mapped from an orthomosaic of the UAV imagery.

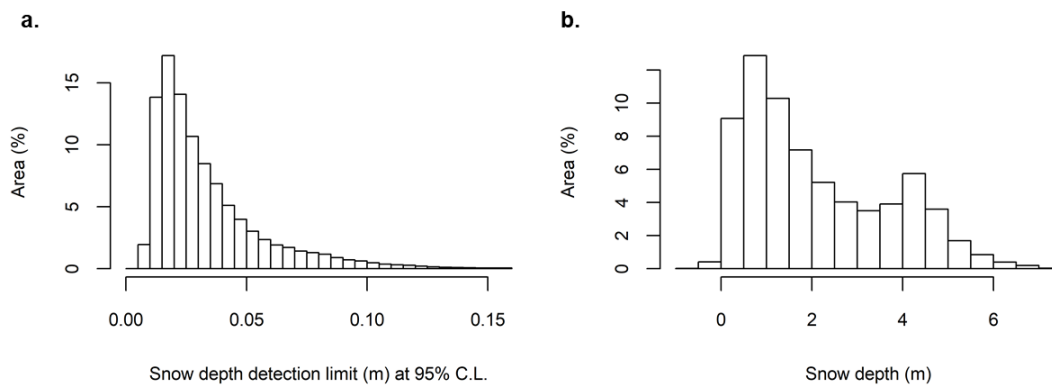


Figure 11. Histograms of the spatially varying snow depth detection limit at a 95% confidence level (a), and SFM-MVS snow depths (b).

4.3.3 Snow depth accuracy and spatial resolution

The accuracy of the snow depths was more sensitive to the spatial resolution of the snow-off DEM than the snow-on DEM (Figure 12). The resolution of the snow-on DEM did not affect the accuracy of the DEM until resolutions coarser than 5 m. The accuracy decreased approximately at a rate of 4 cm per m in coarser resolution when the snow-off DEM was resampled and decreased 5 cm per m in coarser resolution when both DEMs were resampled to a coarser resolution (Figure 12).

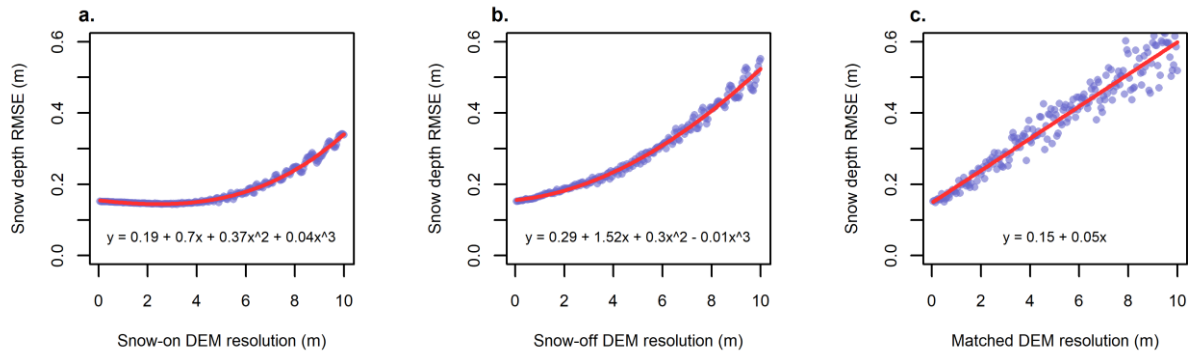


Figure 12. The impact of SFM-DEM spatial resolution on snow depth accuracy (RMSE). (a) the snow-on DEM was resampled to lower resolutions, (b) the snow-off DEM was sampled to lower resolutions, and (c) both DEMs were sampled to lower resolutions.

4.4 Discussion

4.4.1 Mapping snow depth uncertainties

Based on a spatially varying snow depth detection limit, it was shown that SFM-MVS snow depths using UAV imagery can detect depths as shallow as 1 cm (**Figure 11a**). Harder et al (2016) proposed a global SFM-MVS snow detection limit of 30 cm (at 4σ), which would be approximately 15 cm at a 95% confidence level (2σ). For deep snowpacks where it is clear the most of the snow depths will exceed the precision, a global limit of snow depth detection may be suitable (Passalacqua et al., 2015). However, a spatially varying snow depth detection limit may be useful for analysis of shallow snowpack since the precision of snow depths, as observed in this study and by Adams et al (2018), can substantially vary spatially. Spatially varying measures of precision can be used to avoid overly conservative detection limits caused by global thresholds (Lane et al., 2003; Wheaton et al., 2010; Passalacqua et al., 2015).

In general, the precision of the SFM-DEMs is related to flying height, distance to GCP, and image overlap (James et al., 2017b; Goetz et al., 2018), as well as field site conditions (Nolan et al., 2015; Bühler et al., 2016a). That is, errors in the computed snow depths can also vary temporally due to different snow-cover conditions (Bühler et al., 2016a; Harder et al., 2016; Adams et al., 2018). The precision for most of the study area was less than 4 cm (at 1σ). This precision estimate is based on a flying height of approximately 60 m agl. Adams et al (2018) observed precisions ranging from 4 cm for stable terrain to 33 cm for their entire alpine study area. This relatively weaker precision that they reported is likely due to their higher-flying height of 400 m agl. The precision of SFM-DEMs can increase with higher flying heights (Goetz et al., 2018).

In addition to using the detection limits to determine where significant levels of snow depth were detected, a comparison with a map of snow-free areas helped to identify areas where a bias in the snow depths was present. Bias in SFM-MVS snow depths can be caused by co-registration errors (Nuth and Kääb, 2011; Westoby et al., 2012; Marti et al., 2016), changes in the sub-snow topography between snow-on and snow-off DEM acquisition dates (Nolan et al., 2015; Bernard et al., 2017; Gindraux et al., 2017; Avanzi et al., 2018), and a systematic ‘doming’ error in the SFM-DEMs (James and Robson, 2014; Micheletti et al., 2015b). The

pattern in the GNSS-measured errors of the snow-on DEM did show signs of such a doming error (**Figure 8a**). This error is likely due to the poor image collection geometry caused by the UAV imagery being taken at near-parallel directions, and an inaccurate camera model (Micheletti et al., 2015b). Perhaps this error was only observed outside the area enclosed by the GCPs because the error is locally improved near GCPs (James and Robson, 2014; Javernick et al., 2014).

The spatially varying detection limit in this study used critical values of a t distribution based on precision estimates calculated from repeat UAV surveys; however, there are other approaches for calculating a spatially varying estimate of SFM-DEM precision. For example, the position precision of the SFM-MVS tie-points (i.e. sparse point cloud) can be estimated from the bundle adjustment using a stochastic error model, which can be interpolated to map the precision of the corresponding elevation model (James et al., 2017b).

4.4.2 Reducing SFM-MVS snow depth uncertainties

When designing a survey for snow depth monitoring with SFM photogrammetry, just as with lidar (Csanyi and Toth, 2007) and digital photogrammetry (Barrand et al., 2009), it is important to ensure that in each survey the spatial distribution of GCPs encloses the entire area of interest. Otherwise, data may be lost due to low-precision observations, or more-likely due to a strong bias in one of the DEMs that can lead to an over- or underestimation of snow depth, as was observed in this study.

Depending on the desired accuracy and precision of the snow depth estimates, it is also important to ensure that the GCPs are evenly spaced out to control the amount of measurement uncertainty. For example, Goetz et al. (2018), who used the same sensor (DJI Phantom 4) and flying height above ground level (60 m), observed that precision decreased substantially in areas that were farther than 40 m from a GCP. Tonkin et al 2016 observed a decrease in elevation accuracies further away from GCPs: at 100 m away from the GCP they found the RMSE of the elevations became greater than a decimeter. However, as both Tonkin et al. (2016) and Gindraux et al. (2017) observed, the accuracy of the DEM only improved until a certain GCP density is reached. In the case of Gindraux et al. (2017), they found that more than 17 GCPs/km² did not significantly improve DEM accuracy.

Accurate georeferencing of the SFM-DEMs is also important for reducing the uncertainties and improving the accuracy of computed snow depths. Due to the constantly changing topography of a snow-covered surface, especially just after recent snowfall, there may be occasions when there are no exposed snow-free areas that could allow for co-registration of the snow-on and snow-off DEMs to reduce any potential registration biases. Also, the constantly changing snow-covered topography makes it difficult to have GCPs located in the same place (Bernard et al., 2017). In such scenarios, only the positional accuracy of the GCPs measured by a GNSS survey are relied on for the registration of the DEMs.

The influence of GCPs on DEM accuracy, and the resulting snow depth accuracy, is also controlled by the quality of the positional estimate of the GCPs locations (Tonkin and Midgley, 2016; James et al., 2017a). In this study, a local reference GNSS station was used to ensure high

quality positional estimates of the GCPs. Using this approach, it was demonstrated that an overall snow depth accuracy of 15 cm, and a precision of the snow depth measurements of approximately less than 5 cm can be achieved without co-registering the snow-on and snow-off DEMs.

4.4.3 The effects of spatial resolution on snow depth accuracy

The spatial resolution of the snow-off DEM had a stronger influence on the accuracy of the snow depths than the spatial resolution of the snow-on DEM. Since our study area has a complex terrain, the accuracy of the snow depths depended on the ability of the SFM snow-off DEM to capture the small-scale variability of the surface topography, which is consistent with the findings of Cimoli et al (2017). Marti et al (2016) observed that the accuracy of the SFM-MVS snow depths remained similar when calculated for spatial resolutions of 0.1, 1 and 2 m; however, this result contrasts with this study, which found a strong effect on accuracy – a 5 cm decrease with each 1-meter increase in spatial resolution. This difference is likely due to the rougher rocky-debris covered terrain of the site used in this study.

The relatively stable accuracy of the snow depth with lower spatial resolution (**Figure 11**) of the snow-on DEM indicates that future DEM-differencing snow depth calculations may combine data from other sources such as satellite high-resolution stereo imagery (e.g. Pléiades) to capture snow-on conditions (Marti et al 2016). This combination of the SFM- and satellite-derived DEMs could allow for more frequent snow depth estimation in remote areas that are difficult to access. Additionally, one could spend more time in surveying the snow-off DEMs, for examples by flying closer to the surface. Conversely, UAVs can fly higher to capture a larger area when snow is present. The smaller sensitivity to the spatial resolution of the snow-on DEM is likely due to the gentler topography of the snow-covered surface.

4.5 Conclusions

This study presented a method for calculating a spatially varying estimate of snow depth precision and detection limits using repeated UAV surveys. The map of snow depth precision is important for communicating the distribution of uncertainties in the snow depths. Through applying the spatially varying detection limits it is found that it is possible to observe snow depths generally as low as 2 cm with 95% confidence from UAV imagery and SFM photogrammetry. The spatially varying detection limit was also found to be useful in this study to highlight areas where possible snow depth biases were present. Identifying areas that may have a strong bias in the calculated snow depths can be used to delineate the boundaries of the study area where the data quality is acceptable. It is recommended to ensure that the area covered by the GCPs is the same for the snow-on and snow-off DEMs to avoid losing data due to poor SFM-MVS performance in areas more distant from ground control locations.

In our study, a snow-on DEM resolution as low as 5 m would have been sufficient for snow depth estimation without loss of accuracy. This result shows the potential to combine snow-on elevation models obtained from satellites with snow-off SFM-elevation models to map snow depth with high accuracies. The ability to acquire snow-on DEMs with different sensors

may increase the possibility to obtain more frequent high-resolution snow-depth observations in remote areas.

4.6 Acknowledgements

Thanks to the Parc national des Ecrins and the Joseph Fourier Alpine Research Station (SAFJ) for their support, and everyone who assisted in the field. The Natural Sciences and Engineering Research Council (NSERC) of Canada through an Alexander Graham Bell Graduate Scholarship awarded to J. Goetz and funding from the Carl Zeiss Foundation awarded to A. Brenning have supported this research. The data used in this study (i.e., DEMs, UAV imagery, ground control locations, snow probed depths and GNSS survey data) are available in the Mendeley research data repository:

Goetz, J., A. Brenning., M. Marcer, and X. Bodin (2019), UAV imagery and in-situ measurements for structure-from-motion snow depth mapping over the Laurichard rock glacier, France - surveyed in 2017, *Mendeley Data, v1*, <http://dx.doi.org/10.17632/9rhscd27y4.1>

Chapter 5

Accounting for permafrost creep in high-resolution snow depth mapping by modelling sub-snow ground deformation

Abstract

Snow depth estimation derived from high-resolution digital elevation models (DEMs) can lead to improved understanding of the spatially highly heterogeneous nature of snow distribution, as well as help us improve our knowledge of how snow patterns influence local geomorphic processes. Slope deformation processes such as permafrost creep can make it challenging to acquire a snow-free DEM that matches the sub-snow topography at the time of the associated snow-covered DEM, which can cause errors in the computed snow depths. In this study, we illustrate how modelling changes in the sub-snow topography can reduce errors in snow depths derived from DEM differencing in an area of permafrost creep. To model the sub-snow topography, a surface deformation model was constructed by performing non-rigid registration based on B-splines of two snow-free DEMs. Seasonal variations in creep were accounted for by using an optimization approach to find a suitable value to scale the deformation model based on in-situ snow depth measurements or the presence of snow-free areas corresponding to the date of the snow-covered DEM. This scaled deformation model was used to transform one of the snow-free DEMs to estimate the sub-snow topography corresponding to the date of the snow-covered DEM. The performance of this method was tested on an active rock glacier in the southern French Alps for two surveys dates, which were conducted in the winter and spring of 2017.

By accounting for surface displacements caused by permafrost creep, we found that our method was able to reduce the errors in the estimated snow depths by up to 33% (an interquartile range reduction of 11 cm) compared to using the untransformed snow-free DEM. The accuracy of the snow depths was only slightly improved (root-mean-square error decrease of up to 3 cm). Greater reductions in error were observed for the snow depths calculated for the date that was furthest (i.e., the winter survey) in time from the snow-free DEM. Additionally, we found that our approach to scaling the deformation model has promising potential to be adapted for monitoring seasonal variations in permafrost creep by combining in-situ snow depth measurements with high-resolution surface deformation models.

5.1 Introduction

A combination of complex terrain with variable snow accumulation and ablation processes can result in a spatially highly heterogeneous snow distribution (Elder et al., 1991; Blöschl, 1999; Deems et al., 2006; Erickson et al., 2005; Winstral et al., 2013; Grünewald et al., 2013). In mountain areas, snow cover can be an important control of surface deformation rates related to geomorphic processes such as permafrost creep (Ikeda et al., 2008) and shallow-landslides (Matsuura et al., 2003; Okamoto et al., 2018). Snow cover also plays an important role in ground temperatures (Hasler et al., 2011; Luetsch and Haeberli, 2007; Haberkorn et al., 2016). Therefore, providing detailed and accurate mapping of the heterogeneous snow patterns would allow a continued improvement in our understanding of snow distribution and how to model it (Sturm, 2015; Bhardwaj et al., 2016) to better describe the impact of snow cover on mountain geomorphic processes (Swift et al., 2015).

Currently, the best method to capture the spatial variations in snow depth is the use of high-resolution digital elevation models (DEMs). High-resolution mapping of snow depth can be achieved using any or a combination of available techniques for deriving high-resolution elevation models of the Earth's surface. Some common techniques already applied include laser altimetry (LiDAR; (Deems et al., 2006; Prokop et al., 2008; Helfricht et al., 2012; Draebing et al., 2017), digital photogrammetry (Bühler et al., 2015; Marti et al., 2016; Grünewald et al., 2014; Bühler et al., 2012), and structure-from-motion multi-view stereo (SfM-MVS) 3D reconstruction (Nolan et al., 2015; Vander Jagt et al., 2015; Bühler et al., 2016; Michele et al., 2016; Harder et al., 2016).

Snow depth based on high-resolution elevation data can be computed by differencing co-registered elevation models obtained for snow-covered and snow-free conditions. The differencing can be applied to surface elevations represented as 3D point clouds or a corresponding DEM (Deems et al., 2013). It is typically assumed that the surface topography beneath the snow-cover remains unchanged during the period between the acquisition of the snow-covered and snow-free conditions. However, any change in the surface topography between the acquisition dates can contribute to errors in the computed snow depth measurements (Nolan et al., 2015; Bernard et al., 2017; Avanzi et al., 2018). For this reason, applying this approach in mountain areas can be challenging due to on-going changes in surface topography caused by permafrost creep (Haeberli et al., 2006; Käab et al., 2003), and other slope deformation processes (Arenson et al., 2016). Therefore, such changes in surface topography should be accounted for in the snow-free elevation model to reduce errors in the computed high-resolution snow depths, as well as to provide more reliable snow distribution data for analysis on the impacts of snow on local variations in geomorphic processes. In this paper, we propose that a kinematic model of surface displacements can be used to account for changes in topography due to permafrost creep.

The spatial pattern of creeping mountain permafrost is often monitored using surface displacement fields obtain from processing remote sensing data (Arenson et al., 2016). Most commonly, surface displacements fields are determined from multi-temporal optical imagery using image matching techniques (Scambos et al., 1992; Käab, 2002; Heid and Käab, 2012; Käab, 2005; Debella-Gilo and Käab, 2011; Kraaijenbrink et al., 2016; Evans, 2000). Image

matching has also been applied to high-resolution DEMs to produce detailed surface displacement maps of glacial ice (Abdalati and Krabill, 1999), slow-moving landslides (Ghuffar et al., 2013) and permafrost creep (Dall'Asta et al., 2017; Bodin et al., 2018). The use of DEMs for image matching has the advantage of avoiding the requirement of having the paired survey data acquired under similar lighting conditions (Kääb, 2005), and have been found to obtain a greater number of matched pixels than high-resolution optical imagery (Dall'Asta et al., 2017).

Due to its simplicity, normalized cross-correlation is one of the most commonly applied methods for image matching using remote sensing data (Kääb, 2005; Heid and Kääb, 2012). However, this method typically requires post-processing to remove erroneous matches (Heid and Kääb, 2012; Kääb, 2005; Debella-Gilo and Kääb, 2012). Also, large data gaps in surface displacement maps can occur in areas where the image matching algorithm had difficulties detecting corresponding surface features (Bodin et al., 2018; Kääb, 2005). To overcome these issues, image registration techniques, in particular deformable or non-rigid registration, may be a good alternative to using image matching techniques alone for mapping surface displacement field since they are designed to provide a spatially continuous field of displacements for monitoring deformation of objects over time (Hill et al., 2001).

Image registration is the process of aligning images by finding a spatial transformation that maps the pixels from one image to corresponding pixels in another image (Hill et al., 2001). Like image matching techniques, the aligning of two images for registration can be feature- and/or intensity-based, where features refer to corresponding points identified in the images either manually or automatically. The alignment based on features aims to minimize the distance between points, where intensity-based alignment involves minimizing a cost function that measures the similarity between a set of corresponding pixels between images (Yoo, 2004).

Non-rigid image registration allows for a non-uniform mapping of corresponding pixels between images (Rueckert et al., 1999; Crum et al., 2004). The resulting transformation is a deformation field that tracks the displacement of every pixel from one image to another. To ensure that physically meaningful deformations are recorded by the transformation, regularization terms can be applied (Crum et al., 2004; Rueckert et al., 1999). Given this ability to record realistic changes in morphology, non-rigid image registration techniques have promising potential for producing a model of creep-related surface deformations for an entire scene. Additionally, to our knowledge, non-rigid image registration techniques have yet to be applied for monitoring surface displacements of Earth surface landforms.

In this study, we present a method to reduce errors in snow depths computed from high-resolution DEMs in an area of permafrost creep based on surface deformation modelling. The changes in the sub-snow topography caused by permafrost creep movement during snow-cover conditions are estimated by transforming a snow-free DEM using a kinematic model of surface deformations. This model is obtained by performing non-rigid registration using a free-form deformation model based on B-splines of two snow free DEMs. To account for variations in creep rates over time, the resulting displacement field is scaled and then used to transform one of the snow-free DEMs to estimate the sub-snow surface topography at the time

of the snow-covered DEM. The performance of our method is evaluated using in-situ bare-ground topography and snow depth measurements.

5.2 Methods

5.2.1 Study site and data

Our study site is the Laurichard rock glacier in the Combe de Laurichard catchment, Écrins National Park, located in the southern French Alps (45.01°N, 6.37°E). It is an active, tongue-shaped rock glacier extending from 2650 m a.s.l. (the headwall) to 2450 m a.s.l. (the front) with a width varying from about 100 m to 200 m. Based on expert knowledge of the study site (Bodin et al., 2009; Bodin et al., 2018), areas on the rock glacier were considered as active terrain, and the remaining terrain was considered as stable. The delineation of active and stable terrain was based on a map of the rock glacier (**Figure 13**). The movement rate of the rock glacier, measured as the mean annual surface velocity (0.39 to 1.44 m/yr; (Bodin et al., 2009)), is typical of deep-seated permafrost creep (Haeberli et al., 2006). Similarly to many rock glaciers in the Alps (e.g., Delaloye et al., 2008; Kellerer-Pirklbauer et al., 2018), the Laurichard rock glacier experiences interannual fluctuation of its velocity (Thibert et al., 2018). The spatial pattern of displacements have been generally consistent over the past 10 years (Bodin et al., 2018). Consistent spatial patterns of rock glacier movement has also been observed by others (Ikeda et al., 2008).

Our method for accounting for permafrost creep in snow depth mapping was applied to two dates, February 22, 2017 and June 2, 2017, which represent the snow cover conditions during the winter accumulation and spring melt periods. A snow-free DEM was obtained on October 5, 2017. The DEMs were acquired by performing SFM-MVS 3D reconstruction with Agisoft's PhotoScan (version 1.41) to images collected from unmanned aerial vehicle (UAV) surveys using a DJI Phantom 4 quadcopter. The UAV surveys and PhotoScan processing used the same methods as Goetz et al. (2018). The winter DEM (referred to as Feb-2017 DEM) was mainly snow covered except for some large rock debris and boulders located on the rock glacier (**Figure 13**). The spring DEM (Jun-2017 DEM) was partially (75%) snow covered.

An available DEM acquired on August 16-17, 2012 (Aug-2012 DEM) and the Oct-2017 DEM were used to find a non-rigid image transformation that captures the permafrost creep related surface deformation patterns. The Aug 2012 DEM was derived from airborne-laser scanning (ALS; Cessna 206 with a Riegl LMS Q680i laser scanner) (Bodin et al., 2018). All of the DEMs used in our study were sampled (bilinear interpolation) to have a 10 cm × 10 cm spatial resolution.

The vertical accuracies of the DEMs were assessed from Global Navigation Satellite System (GNSS) surveyed elevation measurements (positional accuracy ≤ 2 cm at 1σ). The resulting RMSE for the Jun-2017, Oct-2017 and Aug-2012 DEMs were 7.8 cm, 9.1 cm and 2 cm, respectively (**Table 6**). The RMSE for the Aug-2012 DEM was based on a set of GNSS surveyed points of artificial flat surfaces measured during the acquisition of the airborne LiDAR data (Bodin et al., 2018).

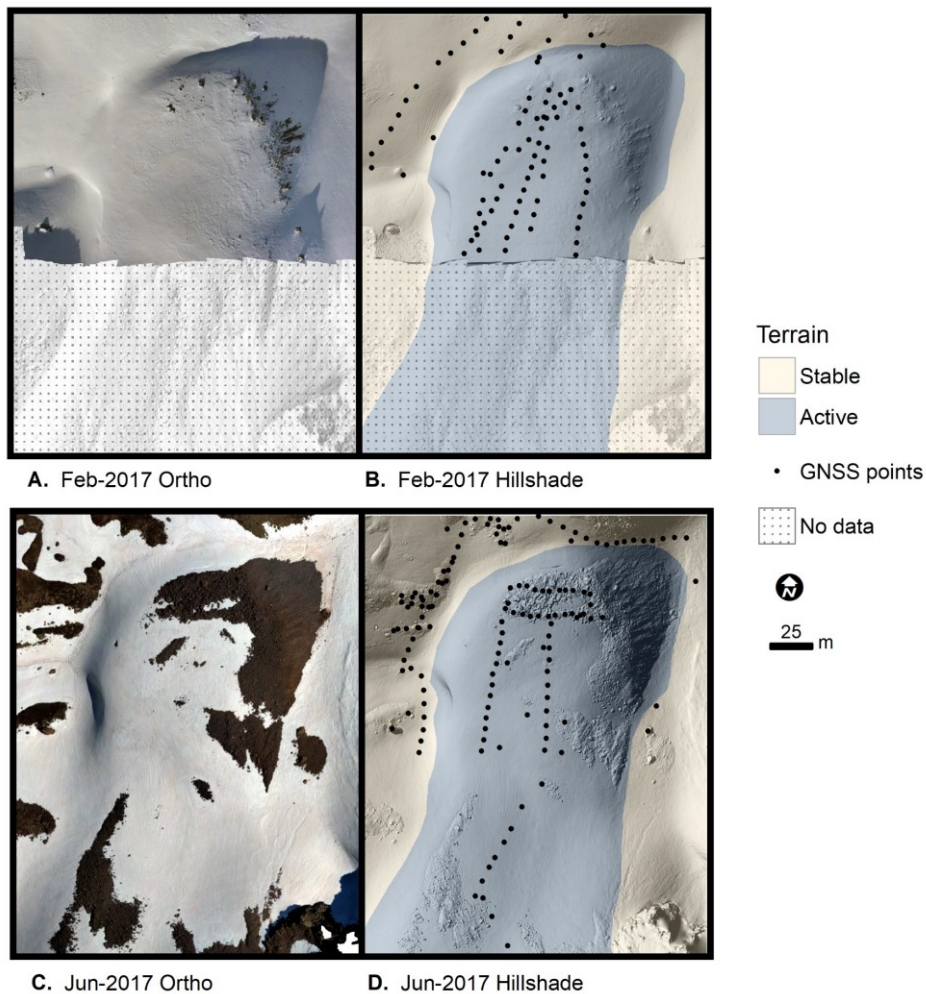


Figure 13. Orthomosaics of the snow-covered scenes on 22-Feb-2017 (a) and 2-Jun-2017 (c). Distribution of field surveyed GNSS points of snow-free areas and snow-probed measured. An outline of the stable and active terrain areas overlays the hillshade models of the Feb-2017 and Jun-2017 DEMs. The winter Feb-2017 DEM covers about half the area of the spring Jun-2017 DEM.

Table 6. Summary of data sets used for estimating snow depth. The vertical accuracy is based on a set of GNSS observations (N) surveyed for each date.

Data overview				
Label	Feb-2017 DEM	Jun-2017 DEM	Oct-2017 DEM	Aug-2012 DEM
Acquisition data	22 Feb 2017	2 Jun 2017	5 Oct 2017	16/17 Aug 2012
Description	Snow covered	Snow covered	Snow free	Snow free
Method	UAV SFM-MVS	UAV SFM-MVS	UAV SFM-MVS	Airborne LiDAR
Vertical accuracy (RMSE)	4.8 cm ($N = 85$)	7.6 cm ($N = 118$)	9.1 cm ($N = 130$)	2 cm ($N = 45$)
No. of snow probe observations	$N_D = 63$	$N_D = 58$	-	-

5.2.2 Mapping snow depth from DEMs

Estimating snow depth $\widehat{D}(\mathbf{x})$ for a continuous surface at locations \mathbf{x} for a given time t_0 can be calculated as

$$\widehat{D}_{t_0}(\mathbf{x}) = S_{t_0}(\mathbf{x}) - \widehat{Z}_{t_0}(\mathbf{x}), \quad (14)$$

where $S_{t_0}(\mathbf{x})$ and $\widehat{Z}_{t_0}(\mathbf{x})$ are DEMs consisting of elevations for the snow-covered surface and the estimated sub-snow topography, respectively. Since the actual sub-snow topography $Z_{t_0}(\mathbf{x})$ at the time of the acquired snow-covered DEM is an unknown, the acquired snow-free DEM $Z_{t_1}(\mathbf{x})$ can be used to estimate $\widehat{Z}_{t_0}(\mathbf{x})$ the sub-snow topography. Given an area with little to no change in the ground topography over time, the estimated sub-snow topography is usually assumed to equal the elevations at the time of a snow-free elevation model either obtained before or after the time of the snow-covered DEM. However, in the case that the surface topography of the snow-free elevation model is likely different than the actual sub-snow topography, meaning there are active deformation processes occurring, the sub-snow topography can be obtained by transforming a snow-free DEM $Z_{t_1}(\mathbf{x})$ to represent the bare-ground topography conditions at the time of the snow-covered DEM.

To determine this transformation $\mathbf{T}_u(\mathbf{x})$, we treat this as a registration problem which aims to find the displacement field $\mathbf{u}(\mathbf{x})$ that makes the snow-free DEM $Z_{t_1}(\mathbf{x} + \mathbf{u}(\mathbf{x}))$ as close as possible to the actual sub-snow topography $Z_{t_0}(\mathbf{x})$. Since the sub-snow topography is unknown, we estimate the transformation by scaling displacements $\mathbf{a}(\mathbf{x})$, which have been determined a priori, that map the general surface deformation patterns of the bare-ground topography. We define the estimate of the transformation $\widehat{\mathbf{T}}_u(\mathbf{x})$ as

$$\widehat{\mathbf{T}}_u(\mathbf{x}, \hat{c}) = \mathbf{x} + \hat{c}\mathbf{a}(\mathbf{x}); \quad (15)$$

the estimated sub-snow topography is therefore determined by applying the estimated transformation to the snow-free DEM $Z_{t_1}(\mathbf{x})$

$$\widehat{Z}_{t_0}(\mathbf{x}) = Z_{t_1}(\widehat{\mathbf{T}}_u(\mathbf{x}, \hat{c})), \quad (16)$$

where \hat{c} is an estimate of a scale factor c , used to find displacements $\mathbf{u}(\mathbf{x})$ by scaling the known displacements $\mathbf{a}(\mathbf{x})$. The scale factor c is basically a measure of the position of the deforming topography relative to the reference snow-free topography $Z_{t_1}(\mathbf{x})$.

The general deformation pattern $\mathbf{a}(\mathbf{x})$ can be obtained by finding a transformation $\mathbf{T}_a(\mathbf{x})$ from non-rigid registration that makes the snow-free DEM $Z_{t_1}(\mathbf{T}_a(\mathbf{x}))$ as close as possible to another snow-free DEM, $Z_{t_2}(\mathbf{x})$, where the transformation $\mathbf{T}_a(\mathbf{x}) = \mathbf{x} + \mathbf{a}(\mathbf{x})$ is a model of the surface deformation. Note that the change in time between the snow-free DEMs, $Z_{t_1}(\mathbf{x})$ and $Z_{t_2}(\mathbf{x})$, should be large enough to detect surface deformations. The snow-free DEM $Z_{t_1}(\mathbf{x})$ should be defined as the snow-free elevation model that is closest in time to the snow-covered DEM since the interpolation of an estimated sub-snow DEM will likely become more unstable as the time between the acquisition dates of the snow-covered and snow-free DEMs increases. Additionally, the accuracy of the estimated transformation $\widehat{\mathbf{T}}_u(\mathbf{x})$ of the snow-free DEM highly depends on how well the model of surface displacements, as determined by $\mathbf{T}_a(\mathbf{x})$, represents

the general deformation of the bare-ground surface topography over time, and on our ability to determine a suitable scale factor c .

A displacement field mapped using deformable (non-rigid) image registration will have a vector magnitude and direction for each corresponding DEM grid cell that can vary spatially. It is therefore assumed that the displacements $\mathbf{a}(\mathbf{x})$, which are used to model the creeping processes acting on the landscape, have a spatial pattern that remains similar during the period between snow-free DEMs, $Z_{t_1}(\mathbf{x})$ and $Z_{t_2}(\mathbf{x})$. A constant displacement rate is not assumed. Instead, by finding an optimal scale value for a given date, we allow our model to account for variations in displacement rates over time.

5.2.3 Finding an optimal scale factor

Given that the transformation $\mathbf{T}_a(\mathbf{x})$ provides a good model of the surface deformation movements, the ability to produce a good estimation of the sub-snow topography for a given time depends on the scaling of this transformation. In this study we apply several methods for estimating an optimal scale factor \hat{c} based on manually mapped surface displacements, snow-free areas in the snow-covered DEM and in-situ snow depth measurements.

Provided there are exposed blocks that can have their movement tracked from the snow-free DEM $Z_{t_1}(\mathbf{x})$ to the snow-covered DEM $S_{t_0}(\mathbf{x})$, we may determine \hat{c} as the average ratio of the magnitude of displacements observed from matching displaced features in $Z_{t_1}(\mathbf{x})$ to $S_{t_0}(\mathbf{x}_i)$ for a set corresponding snow-free (i.e., bare-ground) cell locations, Ω_Z , within the domain of the snow-covered DEM $S_{t_0}(\mathbf{x})$,

$$\hat{c} := \frac{1}{|\Omega_Z|} \sum_{\mathbf{x}_i \in \Omega_Z} \frac{v(\mathbf{x}_i)}{\mathbf{a}(\mathbf{x}_i)} \quad (17)$$

where $v(\mathbf{x}_i)$ are displacements mapped from locations in the snow-free DEM $Z_{t_1}(\mathbf{x}_i)$ to the corresponding snow-free cell locations in the snow-covered DEM $S_{t_0}(\mathbf{x}_i)$, $\mathbf{a}(\mathbf{x}_i)$ are the displacements from transformation $\mathbf{T}_a(\mathbf{x})$, and $|\Omega_Z|$ is the number of snow-free cell locations. The matched features in $Z_{t_1}(\mathbf{x}_i)$ and $S_{t_0}(\mathbf{x}_i)$ can be mapped manually, or, depending on the magnitude of the mapped displacements $v(\mathbf{x}_i)$, an automatic feature extraction algorithm such as the scale-invariant feature transform (SIFT; Lowe, 2004) may be applied.

Alternatively, the estimated scale factor \hat{c} can be optimized using snow-free cells in locations of active terrain in the snow-covered DEM $S_{t_0}(\mathbf{x}_i)$ (e.g., during snow melt conditions) to iteratively calculate the estimated sub-snow topography $\hat{Z}_{t_0}(\mathbf{x}_i)$ with different scale factor c values. The optimal estimated \hat{c} value would result in the an estimated sub-snow topography $\hat{Z}_{t_0}(\mathbf{x}_i)$ that has the greatest similarity to the snow-free cells in the snow-covered DEM $S_{t_0}(\mathbf{x}_i)$, such as defined by the root mean squared error (RMSE),

$$\hat{c} := \arg \min_c \text{RMSE}_Z \left(S_{t_0}(\mathbf{x}), \hat{Z}_{t_0}(\mathbf{x}, c) \right) \quad (18)$$

where

$$\text{RMSE}_Z \left(S_{t_0}(\mathbf{x}), \hat{Z}_{t_0}(\mathbf{x}, c) \right) = \sqrt{\frac{1}{|\Omega_Z|} \sum_{x_i \in \Omega_Z} \left(S_{t_0}(x_i) - \hat{Z}_{t_0}(x_i, c) \right)^2} \quad (19)$$

In the scenario where there are no snow-free areas, a set of snow-probe recorded depths in the active terrain, Ω_D within the domain of $S_{t_0}(\mathbf{x})$, can take the place of snow-free areas to iteratively search for an optimal scale factor. The locations of the snow-depths should be highly accurate to match the location accuracy of the DEMs: e.g., the snow-depth locations determined from a Global Navigation Satellite System (GNSS) survey. Here, the RMSE is determined for the number of observed snow depth locations $|\Omega_D|$

$$\hat{c} := \arg \min_c \text{RMSE}_D \left(S_{t_0}(\mathbf{x}), \hat{Z}_{t_0}(\mathbf{x}, c) \right) \quad (20)$$

where

$$\text{RMSE}_D \left(D(\mathbf{x}), \hat{D}(\mathbf{x}, c) \right) = \sqrt{\frac{1}{|\Omega_D|} \sum_{x_i \in \Omega_D} \left(D(x_i) - \hat{D}(x_i, c) \right)^2} \quad (21)$$

5.2.4 Modelling surface deformation

Rock glacier surface displacements from the snow free DEMs, $Z_{t_1}(\mathbf{x})$ and $Z_{t_2}(\mathbf{x})$, were obtained by performing non-rigid registration using a free-form deformation model based on B-splines (Rueckert et al., 1999). In general, B-splines can be used to create a smooth, continuous and deformable image transformation by manipulating a mesh of control points embedded in an image. A larger spacing of the mesh control points results in modelling more global deformations, while smaller spacing captures local deformations (Rueckert et al., 1999). Thus, a hierarchical multi-resolution approach that uses large to small mesh spacing can model deformations occurring at different scales.

For this paper, we used the bUnwarpJ algorithm for multi-resolution, elastic and consistent 2D image registration represented by B-Splines. bUnwarpJ, which was developed by Arganda-Carreras et al., 2006) is available as a plugin in ImageJ, an open-source image processing software (Schindelin et al., 2015). Its registration process can be guided using image intensity, a consistency constraint, vector regularization and/or a set of landmarks. This algorithm has already been applied for various biological image analysis problems (Komsta et al., 2011; Grocott et al., 2016; Ku et al., 2016).

The bUnwarpJ algorithm is designed to perform bidirectional registration (forward and reverse directions), $Z_{t_2} \rightarrow Z_{t_1}$ and $Z_{t_2} \leftarrow Z_{t_1}$. Bidirectional registration can help reduce the number of ambiguous correspondences between the forward and reverse transformation, which may result in improving the registration accuracy (Johnson and Christensen, 2002). The Oct-2017 DEM was used as the source image (Z_{t_1}), and the Aug-2012 DEM as the target image (Z_{t_2}). The bUnwarpJ settings for the multi-resolution iterations were set to initiate with a ‘‘Fine’’ deformation and finish with ‘‘Super fine’’ deformation. In our case, the initial deformation could be set to ‘‘Fine’’ since the DEMs were already georectified, and as we are

interested in the local deformations between the DEMs. We also set the registration to use both image intensity and feature points; these weights were set to 1. The consistency weight was left at the default value of 10. At first, we experimented with the use of automatic feature detection for extracting corresponding points; however, it was evident that some of the rock debris displacements occurring between 2012 and 2017 were too large to find accurate matches. As a result, we manually identified 233 corresponding points across the scene to assist in the image registration process. DEM-derived hillshade models were used to help identify the corresponding points.

The resulting direct (or forward) B-spline transformation, $Z_{t_2} \rightarrow Z_{t_1}$, was used to model the general deformation patterns as a transformation function $\mathbf{T}_a(\mathbf{x})$. This transformation was converted from the B-spline parameters to a transformation format containing the x and y direction displacements for each grid cell (i.e., the displacement field $\mathbf{a}(\mathbf{x})$). Since bUnwarpJ is a 2D image registration method, it only describes the horizontal (x, y) movement of the corresponding points over time. To determine the 3D displacement (x, y, z) required to interpolate the elevations to estimate the sub-snow topography, we used the change in elevation of the corresponding points between snow-free DEMs, Z_{t_1} and Z_{t_2} , to find the displacement in the z direction. The resulting (x, y, z) displacements representing $\mathbf{a}(\mathbf{x})$ were scaled using an estimated scale factor \hat{c} and applied to transform the snow-free DEM Z_{t_1} to estimate the sub-snow topography (Equation 15). After the transformation $\hat{\mathbf{T}}_u(\mathbf{x}, \hat{c})$ is applied, there may be some grid cells in the estimated DEM $\hat{Z}_{t_0}(\mathbf{x})$ without an assigned value for which interpolation is needed. Inverse distance weighting (IDW; Shepard, 1968) was used to fill these missing elevation values.

5.2.5 Applying sub-snow topography estimates

For the winter scene (Feb-2017 DEM), manual tracking by mapping exposed rock debris (Equation 17), and an optimization of the scale factor based on the snow depths was applied (Equation 20). The manually mapped displacements were based on both aerial imagery and hillshade models from the UAV surveys. We were able to map the displacements of five exposed rocks. For the spring scene (Jun-2017 DEM), the optimization of the scale factor was based on snow-free elevations and snow-depth observations in active terrain (Equation 18). The snow-free areas in the Jun-2017 were mapped from an orthomosaic derived from the UAV imagery. The snow depths for both scenes were based on snow probing in combination with a GNSS (positional accuracy ≤ 2 cm at 1σ) survey of observed depth locations (**Figure 13**). There were 63 field-surveyed snow depth observations made over the rock glacier on February 22, 2017 and 58 on June 2, 2017.

Since the snow-free DEMs used in this study were obtained before (Z_{t_2} ; Aug-2012) and after (Z_{t_1} ; Oct-2017) the snow-covered DEMs (S_{t_0} ; Jun and Feb-2017) the optimized scale factors \hat{c} were determined by applying the transformation (Equations 18 and 20) with a range of c values from 0.0 to 1.0 (with a step of 0.01). As c approaches 0 and 1 the resulting estimated DEM \hat{Z}_{t_0} becomes closer to the snow-free DEMs Z_{t_1} (Oct-2017 DEM) and Z_{t_2} (Aug-2012 DEM), respectively. In this case, the scale values can be interpreted as an approximation of the proportion of surface movement occurring between the dates used for mapping surface

deformation, where one step of 0.01 would be expected to represent 2.68 weeks until October 5, 2017 (or 4.4 cm of average creep movement of the rock glacier). This scale ratio was used to explore the general plausibility of the scale values by determining how far off they are from the actual time between the snow-covered DEM and the Oct-2017 DEM. An overview of the processes involved to estimate the sub-snow topography are presented in **Figure 14**.

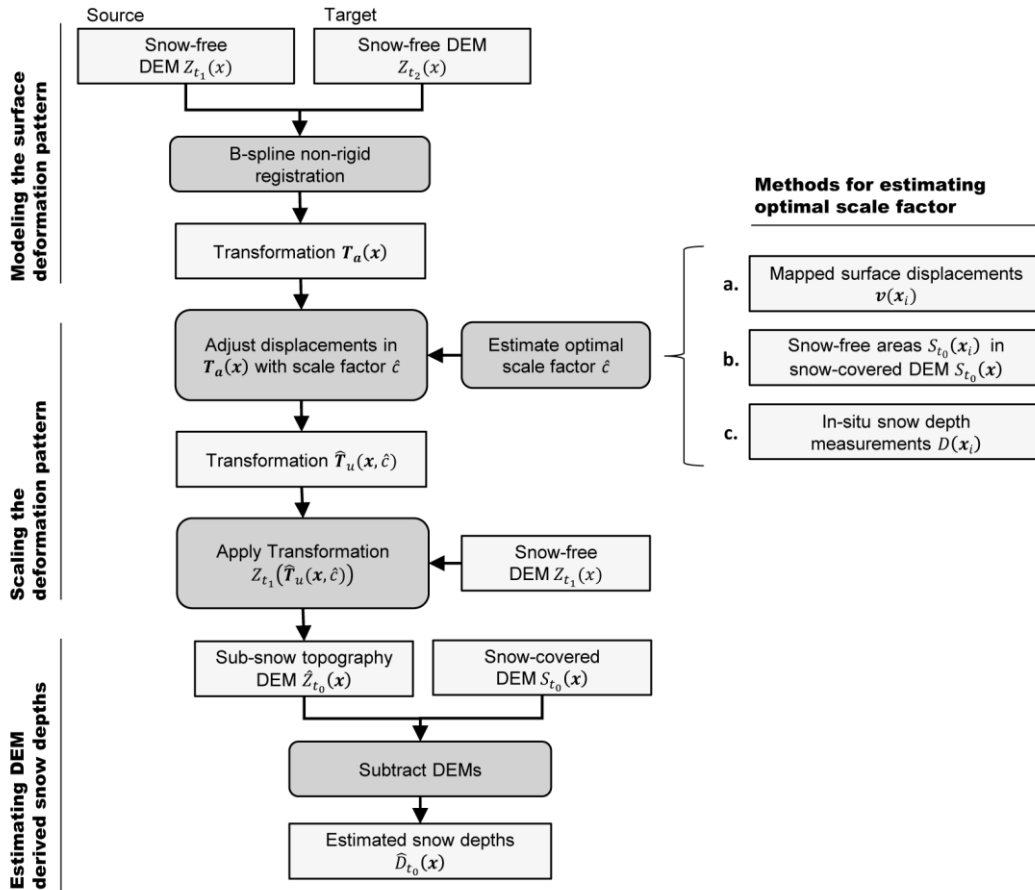


Figure 14. A flowchart outlining the processes involved in estimating the sub-snow topography using non-rigid registration. The source and target snow-free DEMs used to model the general surface deformation pattern related to permafrost creep were the Oct-2017 and Aug-2012 DEMs, respectively. The optimal scale factor \hat{c} was obtained from mapped surface displacements, snow-free areas or in-situ snow-depth measurements. \hat{c} was optimized for the corresponding snow-cover date: either February 22, 2017 or June 2, 2017.

5.2.6 Error analysis

The performance of the sub-snow topography estimates was assessed by comparing the estimated snow depths to in-situ snow-probed measurements (**Table 6**). For each date, the snow depth errors were calculated for the estimated snow depths based on the untransformed snow-free DEMs (Oct-2017 and Aug-2012 DEMs) and the transformed snow-free DEMs (i.e., est. Jun-2017 or est. Feb-2017 DEMs). Since the Jun-2017 DEM contained snow-free areas, the performance of the estimated elevation model (est. Jun-2017 DEM) was also assessed using a GNSS field survey (positional accuracy ≤ 2 cm at 1σ) conducted on June 2, 2017. This survey

allowed for validation of the est. Jun-2017 DEMs independent from the procedure used for optimizing the scale factor. For general comparison, the accuracy was calculated for stable and active terrain. In total 70 points located in exposed stable ($N=35$) and active ($N=35$) terrain were collected. These observed elevations were compared to the nearest grid cells in the Jun-2017 DEM and the est. Jun-2017 DEMs to measure the corresponding elevation errors. Additionally, the error relative to these GNSS surveyed locations to the Oct-2017 and the Aug-2017 DEM were measured as a benchmark for accuracy. The elevation and snow depth errors were reported using the interquartile range (IQR) and median relative absolute error (RAE) to account for the potential presence of outliers. The RMSE was also reported along with the IQR since it is a standard measure of accuracy for measuring elevation height and snow depths.

5.3 Results

5.3.1 Mapped surface deformations

The direction of the modelled surface displacements follows the general downslope path of the rock glacier, where the front is moving slightly northeast (**Figure 15**). The stable areas were modelled as the areas adjacent to and along the sides of the rock glacier. The faster movements (> 1.0 m/yr) in the upper part of the rock glacier occurred in an area where the hillslope is relatively steep compared to the rest of the rock glacier body. There were also modelled fast movements (>1.4 m/yr) on the steep rock face (**Figure 15c**). These high displacement magnitudes on the rock face were not expected since this is a stable outcrop and indicate an area where the image alignment was difficult.

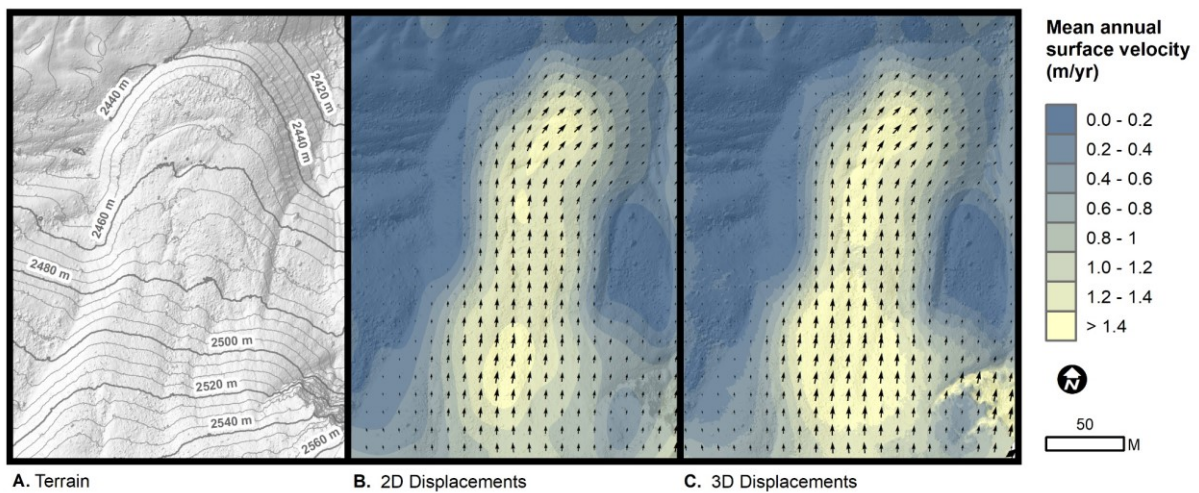


Figure 15. A map of the study site terrain illustrated using a hillshade map and a 5 m contour interval (a), and the 2D (b) and 3D (c) displacement fields obtained from a free-form deformation model based on B-splines. The displacements magnitudes are shown here as the mean annual surface velocities (m/yr) from 2012-2017. The size of the arrows depicting the direction of the rock glacier movement is proportional to the magnitude of the displacements.

5.3.2 Optimal scale factors

The scale factors optimized using the snow-free elevation and snow-depth data were in general agreement (Figure 16). The snow-free areas ($\hat{c}=0.08$) and snow-depth ($\hat{c}=0.08$) optimized scale factors for the est. Jun-2017 DEM were the same. The mapping based ($\hat{c}=0.14$) and snow-depth optimized ($\hat{c}=0.13$) scale factors for the est. Feb-2017 DEM differed by a single step (0.01 or 4.4 cm of average creep movement of the rock glacier). The scale factors were also plausible in terms of their expected displacement on the respective dates (Figure 17). The expected scale factors based on the number of weeks that the June 2, 2017 (18) and February 22, 2017 (32) dates were before October 5, 2017 were 0.07 and 0.12, respectively. Optimized scale factors for June and February were found within 3 weeks of these expected values (Figure 17).

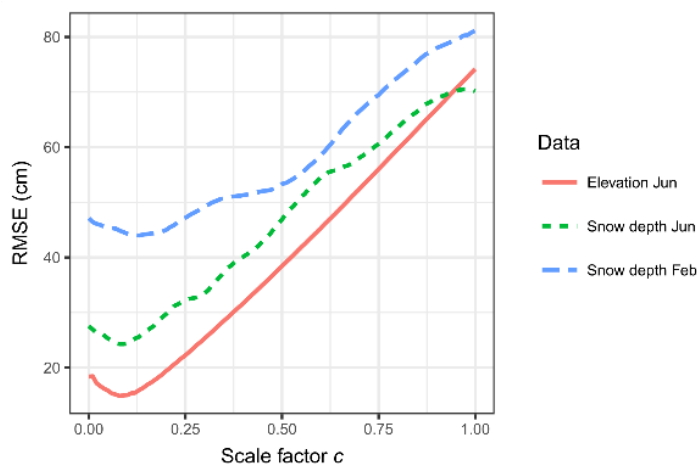


Figure 16. The performance of scaled values for est. Jun- and Feb-2017 DEMs based on optimization using snow-free elevation grid cells (Jun-2017) and in-situ snow-depth measurements (Jun-2017 and Feb-2017).

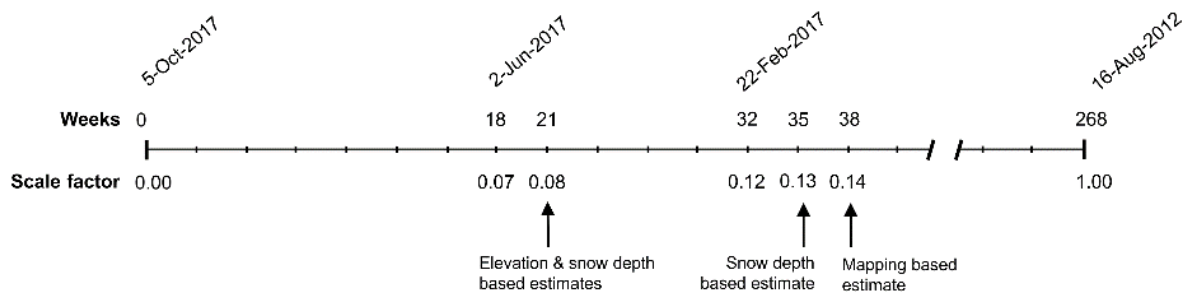


Figure 17. Estimated scale factor c compared to expected weeks

5.3.3 Performance of estimated DEMs

As assessed using GNSS field observations in snow-free areas, the est. Jun-2017 DEM had the best overall vertical accuracy compared to the Oct-2017 and Aug-2012 DEMs (Table 7). The spread of the vertical errors in the est. Jun-2017 DEM (IQR = 5.5 cm) was also considerably lower for the active terrain compared to the Oct-2017 (21.8 cm) and Aug-2012 (54.4 cm) DEMs (Figure 18, Table 7). The est. Jun-2017 DEM also had a lower spread in errors for active terrain compared to the Jun-2017 DEM. The spread of the errors in the stable terrain were generally

similar between the snow-free DEMs with a range in IQRs from 8.4 cm to 9.0 cm (**Table 7**). Additionally, there was a tendency to overestimate the elevations in stable terrain and underestimate them in active terrain.

Table 7. Error in elevations relative to the snow-free GNSS measurements in the Jun-2017 DEM. The errors have been grouped into active (i.e., on the rock glacier) and stable terrain. The est. Jun-2017 DEM where $\hat{c}=0.07$ was obtained from the expected scale factor on 2-Jun-2017 DEMs, and $\hat{c}=0.08$ was obtained from optimization of the elevation and in-situ snow-depth measurements. The Oct-2017 and Aug-2017 were untransformed DEMs. The median and mean error are reported as measures of bias.

DEM	2-Jun-2017 GNSS elevation error (cm)			
	IQR	Median	RMSE	Mean
<i>Overall</i>				
Jun-2017	13.8	0.2	9.5	1.6
est. Jun-2017 ($\hat{c}=0.07$)	9.7	-2.8	13.4	-3.1
est. Jun-2017 ($\hat{c}=0.08$)	9.2	-1.9	13.5	-3.0
Oct-2017	17.2	-2.8	19.8	-7.8
Aug-2012	51.3	-6.8	50.9	-24.3
<i>Active</i>				
Jun-2017	8.1	-3.9	6.7	-4.1
est. Jun-2017 ($\hat{c}=0.07$)	5.0	-5.0	17.1	-8.6
est. Jun-2017 ($\hat{c}=0.08$)	5.5	-5.1	17.3	-8.3
Oct-2017	21.8	-12.0	26.8	-18.3
Aug-2012	54.4	-48.1	70.9	-49.6
<i>Stable</i>				
Jun-2017	7.3	8.0	11.7	7.4
est. Jun-2017 ($\hat{c}=0.07$)	8.9	2.8	8.2	2.4
est. Jun-2017 ($\hat{c}=0.08$)	9.0	2.9	8.2	2.4
Oct-2017	8.5	2.6	7.8	2.6
Aug-2012	8.4	1.5	12.8	1.1

The comparison to the GNSS field observations also illustrated that the reliability of the snow-free DEMs decreases as the time between acquisitions dates increases. The Oct-2017 and Aug-2012 DEMs tended to underestimate the actual elevations in snow free areas (**Figure 18**). The Aug-2012 had the highest overall error (RMSE=51.3 cm, IQR=50.9 cm).

The differences in elevations of the DEMs relative to the snow-free areas in the June-2017 DEM were used to determine which elevation model best represented the sub-snow topography on June 2, 2017. Overall, the est. Jun-2017 DEM had the highest similarity to the snow-free cell locations in the June-2017 DEM followed by the Oct-2017 DEM (**Table 8**). The higher similarity of the est. Jun-2017 DEM compared with the Oct-2017 DEM was mainly attributed to the better performance of the est. Jun-2017 DEM to represent the sub-snow topography in active terrain (**Table 8**).

The highest differences to the Jun-2017 DEM were observed in areas where mass-wasting processes additional to the overall rock glacier creep occur (**Figure 19**). Elevations in the est. Jun-2017 DEM and the Oct-2017 DEM were underestimated where small debris channels formed on the rock glacier front. They were also underestimated in an area just next to the

steep rock face, located in the southeast corner of the scene, where there is evidence of a debris flow. The elevations on the rock glacier front for the est. Jun-2017 and Oct-2017 DEM were for the majority overestimated. However, the front in the est. Jun-2017 DEM appears to have a smaller area of overestimation. The Aug-2012 DEM suffered from high elevation underestimation at the front slope, and high overestimation in snow-free areas located in areas upslope of the rock glacier front.

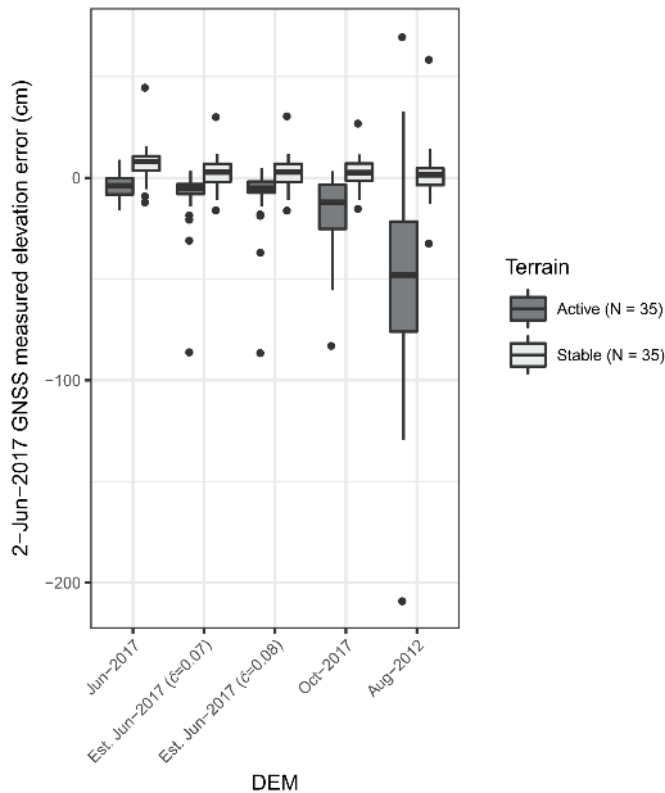


Figure 18. Elevation errors of the Jun-2017 DEMs based on GNSS surveyed elevations of snow-free areas. The errors have been grouped into active (i.e., on the rock glacier) and stable terrain. The est. Jun-2017 DEMs where $\hat{c}=0.07$ were obtained from the expected scale factor on 2-Jun-2017, and $\hat{c}=0.08$ was obtained from optimization of the elevation and in-situ snow-depth measurements. The Oct-2017 and Aug-2017 were untransformed DEMs.

In terms of reducing snow depth errors for the June data, the estimated DEMs had the lowest errors measured by the IQR and median RAE compared to the untransformed DEMs (**Table 8**). As previously observed in the snow-free locations (**Table 7**), the better performance of the estimated DEMs was related to reducing errors in active terrain. Except for the Aug-2012 DEM, the errors in snow-depth were similar in stable areas (**Table 8**). It was also observed that the June snow depths were generally underestimated in active terrain (all median values <-6.0 cm; **Figure 20A**). The snow depth errors were considerably lower in stable terrain than in active terrain (IQR difference of up to 10 cm); however, the snow depth errors in the stable terrain also contained major outliers (**Figure 20a**).

Table 8. Differences in elevations relative to the snow-free areas in the Jun-2017 DEM, and the errors in snow-depth estimation for 2-Jun-2017 based on the comparison of snow-probed measurements and DEM-derived snow depths. The errors have been grouped into active (i.e., on the rock glacier) and stable terrain. The est. Jun-2017 DEMs where $\hat{c}=0.07$ was obtained from the expected scale factor on 2-Jun-2017, and $\hat{c}=0.08$ was obtained from optimization of the elevation and in-situ snow-depth measurements. The Oct-2017 and Aug-2017 were untransformed DEMs. The median and mean error are reported as measures of bias.

2-Jun-2017 DEM	Snow-free elevation difference (cm)				Snow depth error (cm)						
	IQR	Median	RMSE	Mean	IQR	Median	RMSE	Mean	Median	Median	
									RAE %	depth (cm)	
Overall											
est. Jun-2017 ($\hat{c}=0.07$)	9.5	-1.2	14.5	-2.3	12.2	-1.4	47.1	7.0	6.7	115.8	
est. Jun-2017 ($\hat{c}=0.08$)	9.6	-1.3	14.6	-2.5	13.0	-1.4	47.0	6.8	6.6	114.9	
Oct-2017	12.5	-1.8	16.1	-0.8	16.5	-0.9	47.8	8.1	7.4	118.4	
Aug-2012	52.5	-6.4	61.0	-23.0	36.5	0.5	66.7	3.2	15.9	114.5	
Active											
est. Jun-2017 ($\hat{c}=0.07$)	8.6	1.3	15.1	-0.5	15.5	-6.9	24.4	-5.2	8.9	94.8	
est. Jun-2017 ($\hat{c}=0.08$)	8.6	1.3	14.9	-0.8	16.5	-7.1	24.3	-5.5	9.2	95.3	
Oct-2017	15.8	2.1	18.4	1.6	19.5	-6.0	27.6	-3.2	11.0	93.0	
Aug-2012	100.4	-18.4	75.1	-34.1	61.4	-21.6	70.5	-18.8	35.8	99.0	
Stable											
est. Jun-2017 ($\hat{c}=0.07$)	5.1	-5.0	13.3	-5.7	9.9	1.4	61.1	18.3	5.3	166.3	
est. Jun-2017 ($\hat{c}=0.08$)	5.2	-5.0	13.9	-5.7	9.7	1.4	61.1	18.3	5.0	166.3	
Oct-2017	5.3	-4.9	10.7	-5.3	9.8	2.0	61.0	18.7	5.0	166.5	
Aug-2012	12.1	-3.4	12.8	-2.4	17.0	4.9	62.9	23.7	5.1	172.2	

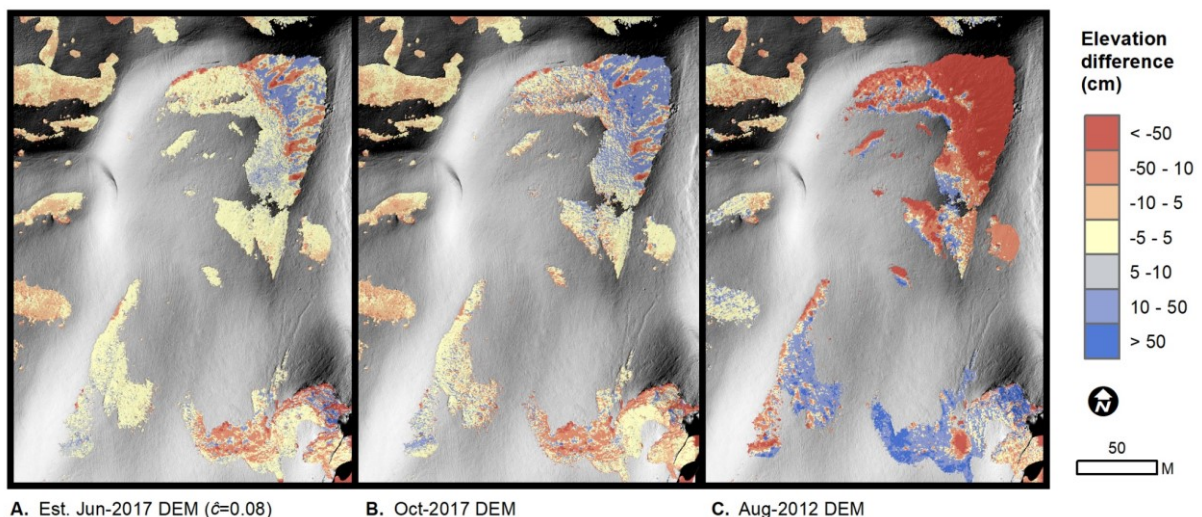


Figure 19. Maps of the difference in elevations for the est. Jun-2017 ($\hat{c}=0.08$), Oct-2017 and Aug-2012 DEMs from the snow-free areas in the Jun-2017 DEM.

Table 9. Errors in snow-depth estimation for 22-Feb-2017 based on the comparison of snow-probed measurements and DEM-derived snow depths. The errors have been grouped into active (i.e., on the rock glacier) and stable terrain. The est. Feb 2017 DEMs where $\hat{c}=0.12$ obtained from the expected scale factor on 22-Feb-2017, $\hat{c}=0.13$ from the optimization of the in-situ snow depth measurements, and $\hat{c}=0.14$ from the manually mapped displacements. The Oct-2017 and Aug-2017 were untransformed DEMs. The median and mean error are reported as measures of bias.

22-Feb-2017 DEM	Snow depth error (cm)					
	IQR	Median	RMSE	Mean	Median RAE %	Median depth (cm)
<i>Overall</i>						
est. Feb-2017 ($\hat{c}=0.12$)	17.5	3.3	55.0	15.5	7.1	152.5
est. Feb-2017 ($\hat{c}=0.13$)	17.6	3.2	55.0	15.7	7.5	152.4
est. Feb-2017 ($\hat{c}=0.14$)	18.3	3.3	55.1	15.8	7.2	151.8
Oct-2017	23.1	3.7	57.0	14.2	10.1	152.0
Aug-2012	58.7	8.1	80.7	23.3	26.7	144.0
<i>Active</i>						
est. Feb-2017 ($\hat{c}=0.12$)	21.4	0.8	44.0	10.8	9.1	149.7
est. Feb-2017 ($\hat{c}=0.13$)	22.7	1.8	44.0	11.0	8.2	149.4
est. Feb-2017 ($\hat{c}=0.14$)	25.5	1.7	44.1	11.2	8.2	148.2
Oct-2017	32.0	-0.8	47.1	9.0	13.1	146.6
Aug-2012	80.4	20.4	80.5	22.1	35.8	141.0
<i>Stable</i>						
est. Feb-2017 ($\hat{c}=0.12$)	9.2	5.5	78.3	29.1	5.4	159.6
est. Feb-2017 ($\hat{c}=0.13$)	9.1	5.4	78.4	29.1	5.4	159.6
est. Feb-2017 ($\hat{c}=0.14$)	8.9	5.4	78.5	29.1	5.4	159.6
Oct-2017	9.6	5.6	78.7	29.0	4.9	159.1
Aug-2012	9.6	6.7	81.5	26.6	5.3	160.3

For the February data, the lower IQRs and median RAEs demonstrate that the estimated elevation models performed better at estimating snow depths compared to the untransformed DEMs (**Table 9**). Like the June results, the spread of the snow depth errors was larger in active terrain (all IQRs >22.7 cm) than in stable terrain (all IQRs <9.6 cm).

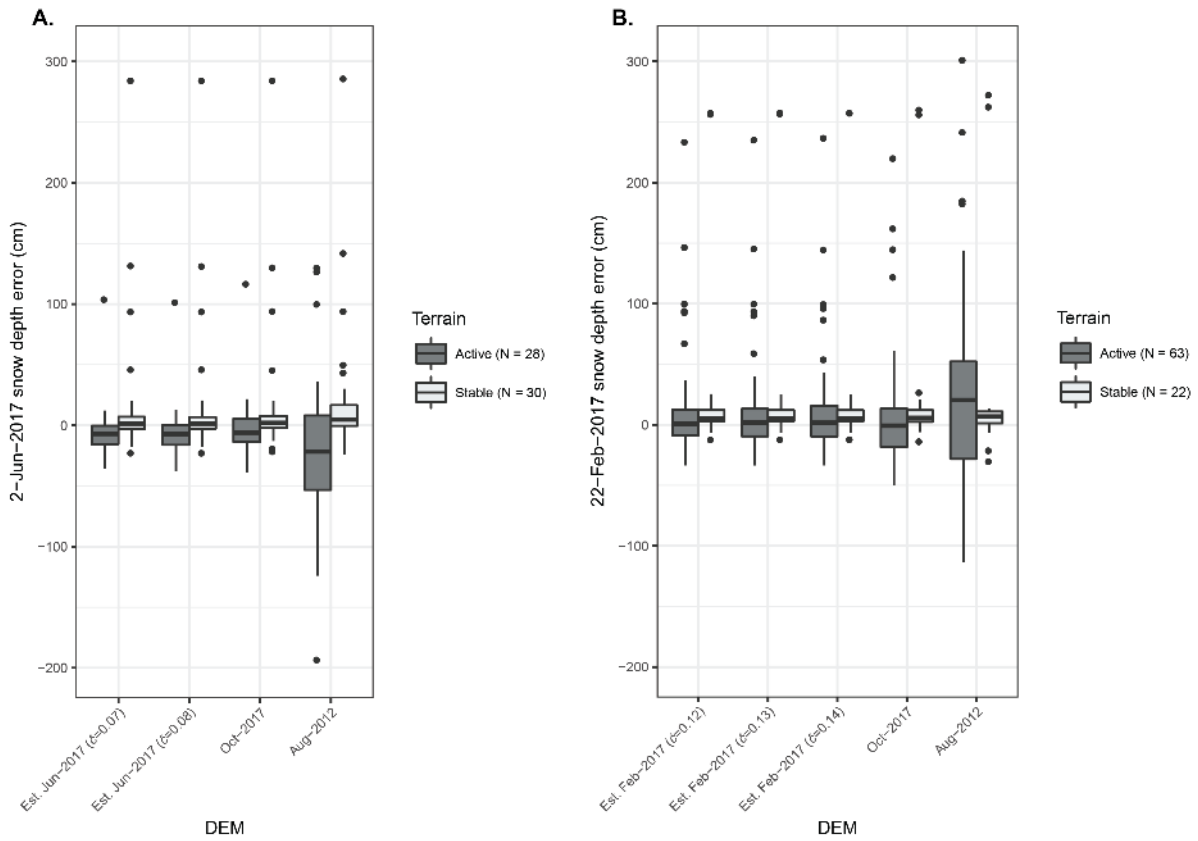


Figure 20. Box plots of the error between snow-probed measured and the DEM-derived snow depths for 2-Jun-2017 (a) and 22-Feb-2017 (b). The snow depth error has been grouped by active (i.e., on the rock glacier) and stable terrain. Est. Jun-2017 DEMs where $\hat{c}=0.07$ was obtained from the expected scale factor on 2-Jun-2017, and $\hat{c}=0.08$ was obtained from optimization of the elevation and in-situ snow-depth measurements. The est. Feb 2017 DEMs where $\hat{c}=0.12$ obtained from the expected scale factor on 22-Feb-2017, $\hat{c}=0.13$ from the optimization of the in-situ snow depth measurements, and $\hat{c}=0.14$ from the manually mapped displacements. The Oct-2017 and Aug-2017 were untransformed DEMs.

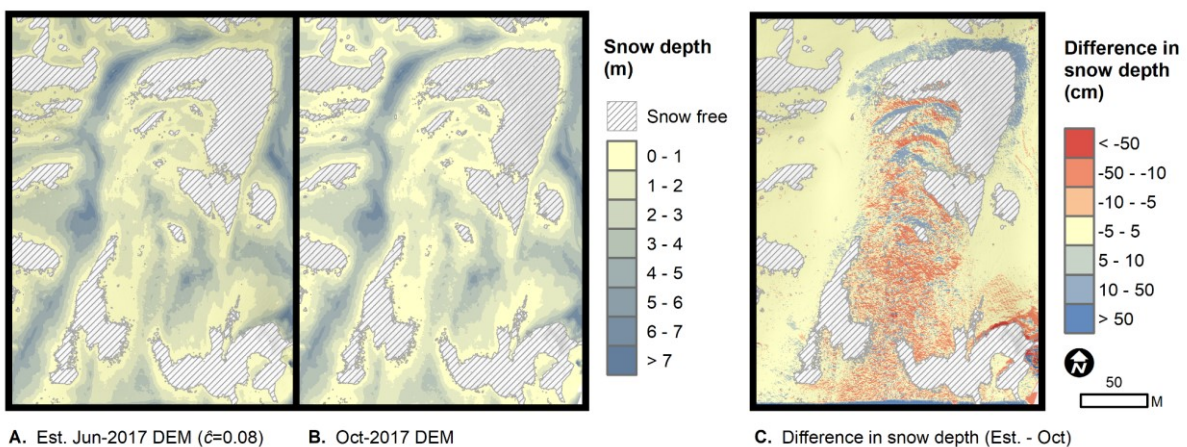


Figure 21. Snow depth maps derived from the est. Jun-2017 DEM ($\hat{c}=0.08$) (a) and the Oct-2017 DEM (b) for 2-Jun-2017, as well as a map of the difference in snow depth estimated by these DEMs (c). Positive values in the difference map indicate areas where the est. Jun-2017 DEM derived snow depths were deeper than the Oct-2017 DEM derived snow depths.

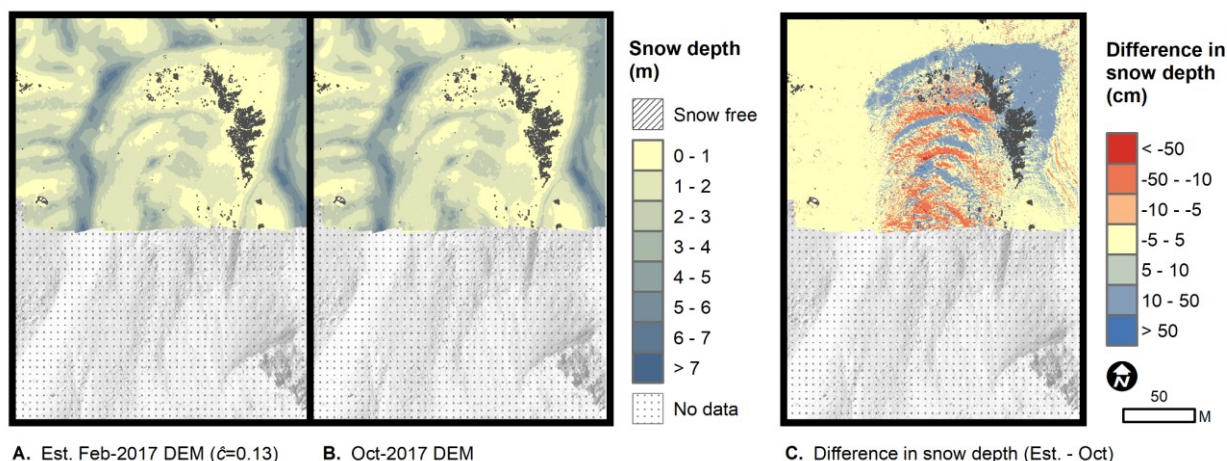


Figure 22. Snow depth maps derived from the est. Feb-2017 DEM ($\hat{\sigma}=0.13$) (a) and the Oct-2017 DEM (b) for 22-Feb-2017, as well as a map of the difference in snow depth estimated by these DEMs (c). Positive values in the difference map indicate areas where the est. Feb-2017 DEM derived snow depths were deeper than the Oct-2017 DEM derived snow depths.

By qualitatively examining the snow depth maps, it appears at the scale of meters that the general patterns were similar between the est. DEMs and the Oct-2017 DEM derived snow depths (Figure 21ab and Figure 22ab). However, by looking at the sub-meter scale (Figure 21c and Figure 22c), the pattern of snow depth varied substantially in the area on the rock glacier, particularly at the rock glacier front, and where compression ridges are present.

5.4 Discussion

5.4.1 Performance of the deformation model

The ability to improve the estimate of the sub-snow topography and to reduce errors in the resulting snow depths weighed heavily on the ability of the surface deformation model to correctly represent the spatial pattern of the rock glacier movement. Our model based on non-rigid image registration using B-splines to model surface deformations appeared to perform well throughout most of the scene. The model displacement magnitudes and directions of the rock glacier movement and stable areas agreed with our knowledge of the scene. The GNSS-assessed accuracy of the est. Jun-2017 DEMs were most similar to the snow-free areas of the Jun-2017 snow-covered DEM, and the elevation accuracy was nearly 50% better than the Oct-2017 DEM. Additionally, the overall pattern of the displacements on the rock glacier matched well to the patterns obtained using the IMCORR image matching algorithm in a study by Bodin et al. (2018). However, there were some areas where it was clear where the deformation model did not perform well (Figure 15).

The rock glacier front was one of the most difficult areas for the registration algorithm to perform. The movement of rock debris on the rock glacier front was more dynamic than the rest of the rock glacier body due to the steep slope. Here, the main mass-wasting processes were rock-falls and small debris slides. This dynamic nature of the rock glacier front, or any area on the rock glacier where more rapid mass wasting processes occur, can make it more difficult to determine pixel correspondences. Alternatively, if features are identified on the rock glacier front, such as large boulders, we have to be cautious to map these correspondences, as

it may result in modelling displacements that are unrelated to the overall rock glacier creep movement. It is likely that the errors in the deformation model related to other mass-wasting processes can be reduced by performing non-rigid registration using DEMs acquired in the snow-free period directly before and after the snow-cover season. However, deformations related to seasonal erosion (Bernard et al., 2017) and frost-heaving (Nolan et al., 2015) would still be difficult to spatially model since they occur locally beneath the snow-cover.

The steep rock face of a stable outcrop was also an area where the deformation model did not perform well. It is likely that the errors in vertical displacement for the steep rock face were due to vertical disagreements between the LiDAR Aug-2012 and SFM-MVS Oct-2017 derived DEMs in this stable area. The vertical accuracy of DEMs derived from both airborne LiDAR and SFM-MVS data are known to deteriorate on steeper terrain (Hodgson and Bresnahan, 2004; Tonkin et al., 2014). To overcome this issue, it may be necessary to align the stable areas of these DEMs before performing registration on the entire scene. In general, more accurate SFM-MVS DEMs can be obtained by using lower UAV flying heights (Smith and Vericat, 2015; Goetz et al., 2018). Broad systematic errors in SFM-MVS DEMs can be mitigated using well-distributed high-quality GNSS measured ground control (Tonkin and Midgley, 2016; James et al., 2017a; James and Robson, 2014), and by including images taken at oblique angles to the ground surface in the UAV imagery collection (James and Robson, 2014).

5.4.2 Finding the optimal the scale factor

The proposed methods for finding the optimal scale factor (i.e., manually mapping displacements, using probed snow depths, or using snow-free areas) were shown to produce estimates of the sub-snow topography that were more accurate than using the acquired snow-free DEM. During spring melt conditions containing snow-free areas, finding an optimal c was rather straightforward, and required no additional data collection. In contrast, finding the scale factor during the times of complete snow cover may require additional data.

Some winter scenes may have exposed debris that can be utilized to determine c , as demonstrated in this study. Yet, there will be occasions when the scene is completely snow covered. In this case, we illustrated how snow probed depths can be used to find an optimal c . If the DEMs are derived from UAV or terrestrial imagery (i.e., SFM-MVS 3D reconstruction), the required depths for optimization can be measured after image acquisition during the collection of ground control points. DEMs derived from SFM-MVS methods generally require the use of a network of GNSS surveyed ground control for accurate DEM construction (Tonkin and Midgley, 2016; James et al., 2017b). However, collecting snow probed depths can be challenging and dangerous depending on the given snow conditions and terrain complexity.

Although it was not initially proposed, we found that the expected scale factor determined as the proportional time before October 5, 2017 also produced estimated DEMs that reduced errors in the DEM representing the sub-snow surface and reduced the corresponding snow depth errors compared the Oct-2017 DEM. That is, given the rate of permafrost creep movement is rather constant, a suitable scaling factor can also be determined based on the date

of the snow-covered scenes alone (as illustrated in **Figure 17**) for occasions when the scene is completely snow covered.

The general agreement of the snow-free based and snow-depth based optimization of the scale factors illustrates a promising potential of manual snow depth probing, in combination with an accurate surface deformation model, to monitor interannual variations of permafrost creep during snow-covered periods. Since the scale factor can be expressed as the displacement rate relative to the time of one of the snow-free DEMs, seasonal variation may be observed by comparing the determined scale factors from snow probe surveys taken from a range of dates during the snow-covered period.

5.4.3 Snow depth errors

The reduction in snow depth errors related to using the estimated sub-snow surface DEM compared to the available snow-free DEM illustrates that surface deformation processes, such as permafrost creep, can lead to errors in high-resolution snow depths determined from differencing of DEMs. It also illustrates that kinematic models of the surface deformation can be used account for the permafrost creep related changes in topography between snow-covered and snow-free DEM acquisition dates to reduce errors in snow depth estimation.

In previous studies, the observed accuracies of snow depth estimated from high-resolution DEMs measured as the RMSE varied from of 7 cm to 30 cm (Nolan et al., 2015; Vander Jagt et al., 2015; Bühler et al., 2016; Harder et al., 2016; Michele et al., 2016). The overall accuracy of the est. Feb-2017 DEM snow depths (55 cm) and the est. Jun-2017 DEM snow depths were just outside of the range (47 cm). Outliers influenced these comparatively high RMSE values, ranging from 50 cm to 300 cm (**Figure 20**), of the snow depth errors based on snow probe measurements. Since the majority of these outliers were overestimating the snow depths, we believe they may have been caused by occasions where the snow probe failed to penetrate the ground. To account for outliers in the survey data, the IQR was used as an alternative to the RMSE as a measure of the spread of the error.

Although the spread of error between the stable and active terrain in snow-free areas of the Jun-2017 DEMs were similar (min. IQR difference of 3.5 cm), the snow depth errors were lower on stable terrain than active terrain (6.8 cm). This dissimilarity in snow depth errors was also found with the Feb-2017 derived snow depths (13.6 cm). Given the surface of the stable terrain is not as rough as the active terrain, we believe this dissimilarity in snow depth errors may be due the challenges of obtaining accurate snow probe measurements in rock-debris filled terrain. That is, due to the higher variability in the surface topography, the accuracy of the snow probe measurements is more sensitive to GNSS-related location errors, and errors in reading of the snow depth caused by the snow probe penetration not being perpendicular to the ground. An improved GNSS surveyed snow depth sampling scheme could be applied in future works. For example, Harder et al (2016) used the average snow depth measurement around a given location (i.e., within a 40 cm x 40 cm square) to account for snow depth reading errors related to the terrain's surface roughness when validating snow depths derived from high-resolution DEMs.

5.5 Conclusion

Errors in high-resolution snow depths derived from DEMs in mountain areas can be reduced by accounting for slope deformation, in this study by permafrost creep. This error reduction comes from being able to accurately model terrain surface deformations related to permafrost creep using non-rigid image registration. Multiple methods, which account for variable surface displacements over time, can be used to find a scaling factor to transform the displacement field for estimating a DEM representing the terrain surface beneath snow cover. In this study, they all resulted in estimated DEMs that provided an improved representation of the sub-snow topography relative to the original snow-free DEM. Surprisingly, a scale factor simply estimated based on the time before the snow-free scene resulted in an improvement of the estimate sub-snow topography similar to the optimization techniques.

Although the free-form deformation model based on B-splines for non-rigid image registration was performed for modelling only the movement of permafrost creep, we expect it could also be used to improve surface deformation modelling of other Earth surface processes such as landslide creep or glacial flow. Additionally, non-rigid image registration is not limited to DEM data, and can also be applied to optical remote sensing imagery to obtain displacement fields of the horizontal movement of Earth surface processes.

5.6 Acknowledgements

We would like to thank the Parc national des Ecrins and the Joseph Fourier Alpine Research Station (SAFJ) for their support, and everyone else who assisted us in the collection of this data. Also, thanks to the constructive comments provided by the anonymous referees. The Natural Sciences and Engineering Research Council (NSERC) of Canada through an Alexander Graham Bell Graduate Scholarship awarded to J. Goetz and funding from the Carl Zeiss Foundation awarded to A. Brenning have supported this research.

Chapter 6

General discussion and conclusions

The goal of this thesis was to enhance the understanding of the measurement uncertainties in SFM-MVS snow depth mapping with UAV surveying. To reach this goal, this thesis focused on developing methods for quantifying, characterizing and correcting errors in SFM-MVS elevation models and snow depths for alpine environments. In this section the importance of this work related to the research questions outlined in **Section 1.2** is discussed. Additionally, how the methods, results and findings in this thesis relate to general topographic mapping and change detection analysis with SFM-MVS elevation models are discussed.

6.1 Uncertainties in SFM-MVS DEMs

Most research on SFM-MVS applied to snow depth mapping, and geosciences in general, has focused on validating the performance of the SFM-MVS elevation models by comparison to more traditional topographic surveying methods such as lidar, and high-accuracy and precision differential GNSS surveys (Westoby et al., 2012; Carrivick et al., 2016). SFM-MVS methods have been tested for a wide range of geoscientific mapping applications; however, no standards for robustly validating the quality of the SFM-MVS elevation models are generally available (Smith et al., 2015). Also, many authors use different terminology to define SFM-MVS elevation model errors, which can make comparing results from one study to another difficult. To help resolve this issue, definitions for describing the spatial pattern of errors in DEMs depending on the available validation data were presented in this thesis.

In addition to describing errors, visualizing the errors is essential to support the quality of the SFM-MVS DEMs (James et al., 2017a; Goetz et al., 2018). For example, bubble plots illustrating the magnitude of errors determined from a well distributed set of check points are important to reveal if any major systematic errors are present in the DEM. Clusters of relatively large errors can indicate problems in the quality of the SFM-MVS reconstruction (James and Robson, 2014; Javernick et al., 2014; Magri and Toldo, 2017). Additionally, as shown in this thesis, repeated measurements can help illustrate how uncertainty can spatially vary and how it depends on the survey design.

As illustrated in this thesis, quantifying the spatial distribution of DEM precision from repeated surveys can be used to express the uncertainty related to random variations in SFM-MVS derived elevations. The major advantage of the repeated surveying methods for estimating precision is that they communicate one of the main concerns of topographic surveyors, which is knowing the actual variation in topographic mapping from one survey to the next (Lane et al., 2003; Wheaton et al., 2010; Passalacqua et al., 2015).

There are other methods for producing spatially varying estimates of precision for SFM models. For example, measuring the variation in the SFM model parameters like the 3D locations of the tie-points can provide a measure of precision. This method can also be extended to consider the variation in the tie-point locations related to georeferencing errors by performing a Monte Carlo simulation of the bundle adjustment using a distribution of GCP errors (James et al., 2017b). Precision can also be estimated by measuring the local roughness of each point in the dense point cloud (Lague et al., 2013). Both these methods produce precision estimates by quantifying the consistency of estimated point locations internally based on a single dataset. This contrasts with the methods used in this thesis, which estimates precision by measuring the actual variation in elevation values using repeat observations obtained from multiple UAV surveys.

Additionally, precision estimates based solely on the SFM model are limited to the tie points in the sparse point cloud. That is, precision is not estimated for the corresponding dense point cloud that is typically used to produce the DEM. Therefore, for detailed precision analysis, such as required for topographic change detection, interpolation of precision across the elevation model may be required (James et al., 2017b). The approach proposed in this thesis using repeated-surveys can calculate the precision for each grid cell without the need of interpolation. However, if only the general pattern of uncertainty is required, or the study areas is too large to perform repeated flights, the internal SFM model- and surface roughness-based precision estimates are good alternative approaches.

Although in-situ field measurements for measuring bias and repeated-survey based estimates of precision are crucial for assuring the quality of SFM-MVS DEMs from UAV surveys (Smith et al., 2015; James et al., 2017a; Goetz et al., 2018), it can be challenging to always obtain validation data depending on the field site size and complexity. Performing repeated flights and collection GNSS surveyed validation data can be time consuming and thus difficult to perform for large study areas. Therefore, at the very least, it is recommended to perform a detailed uncertainty analysis or a pilot test of the UAV and SFM-MVS survey design for a small segment of a study area. By doing so, a better picture can be drawn of how the particular camera sensor, distribution of ground control, environmental conditions, UAV survey design and SFM-MVS software will affect DEM uncertainty (Smith et al., 2015; Benassi et al., 2017; James et al., 2017a; Goetz et al., 2018; Hendrickx et al., 2019). Generally in sciences pilot studies have a key role in making certain that applied surveying methods are suitable for investigating given research questions (Lancaster et al., 2004).

Some of the most widely used software for performing SFM-MVS reconstruction, including Agisoft PhotoScan and Pix4D provide black-box reconstruction solutions (Carrivick et al., 2016; Hendrickx et al., 2019). As a result, internally estimating uncertainties can be challenging. James et al. (2017b) provided a customized solution based on Monte Carlo simulations of errors. However, this is currently only a solution that can be applied when using PhotoScan. Therefore, one of the biggest advantages of repeated-survey based precision estimating is that it is software independent. This means that regardless of the SFM-MVS software used for elevation modelling, a measuring of the spatial variation of uncertainties can be produced. As a result, determining repeated-survey based precision estimates are highly suitable for

benchmarking the 3D reconstruction performance of different SFM-MVS methods and software.

Furthermore, the repeated UAV image collection surveys performed on February 22nd, June 1st, and October 5th, 2017 are therefore a unique dataset for testing methods for assessing uncertainties in the SFM-MVS DEMs. Accessible datasets are needed for benchmarking SFM-MVS reconstruction methods for geoscience applications (Smith et al., 2015). The June and October UAV surveys and in-situ field measurements have therefore been published on an open-access data repository (Goetz et al., 2019). It is highly suggested that this data is used for helping assess the limitations of different SFM-MVS reconstruction software solutions.

6.1.1 Characterizing SFM-MVS DEM error

Knowing where and what is influencing the SFM-MVS DEM uncertainty can be used to improve future UAV surveys, or for simply understanding the limitations of the SFM-MVS method. In this thesis, regression modelling was applied to determine UAV survey characteristics (e.g., image overlap, camera height and GCP distribution) and field site conditions (e.g., shadows and hillslope angle) that effect the spatial variation in uncertainty of the SFM-MVS DEMs. This work was the first study performed that comprehensively investigated the effect of these factors on precision using a multiple variable approach, and it was also the first study to explore the precision of applying SFM-MVS methods for obtaining a DEM of a snow-covered surface.

No two SFM-MVS DEMs derived from UAV surveying will be identical. Changing environmental factors such as weather (e.g., variation in wind and lighting conditions) and technical limitations like the precision of the UAV navigation system make collecting identical image networks practically impossible in the outdoor environment. This issue is due to SFM procedures being highly sensitive to the set of tie points and the bundle adjustment for fine tuning the estimation of intrinsic and extrinsic camera parameters (James and Robson, 2012; Harwin et al., 2015). While SIFT's feature matching is robust to variation in feature appearance, substantial appearance changes can make it difficult to determine feature correspondences (Snavely et al., 2008). Therefore, small changes in the appearance and viewing angle of images from one survey to another can result in different tie points, which results in variations of the elevation surface between DEMs from repeated UAV surveys.

Random procedures in the SFM method, like filtering erroneous feature correspondences using RANSAC, can also result in different tie points (Dickscheid et al., 2008). Hendrickx et al. (2019) assessed the variation in DEMs from repeated SFM-MVS processing of a rock glacier front using PhotoScan. While using identical images and pixel locations of marked GCPs they found that the reconstructed elevations varied substantially on steep slopes (standard deviation up to 10 cm) and at the edge of the reconstructed model where image overlap was low (standard deviation up to 3 m). Consequently, in addition to variability in image networks, some of the variation in elevations observed using repeated UAV surveys can also be attributed to the built-in random variability of the SFM procedure.

This mixing of contributions of random error to the precision estimate can pose a problem when trying to model the direct influence of UAV survey design on DEM uncertainty. In this thesis, to account for the random error from the SFM procedure, the mean image reprojection error was included as variable in the model of the DEM precision. The mean image reprojection error, which is a measure of the SFM quality, can be a proxy for areas within a reconstructed scene that may be more sensitive to uncertainties in the SFM procedure.

In general, areas that typically have higher reconstruction uncertainty are also areas that are more sensitive to variation in the SFM procedure. This uncertainty can be expressed by reprojection errors. The quality of feature matching and the corresponding measure of reprojection error are influenced by image quality (e.g., blurry), image texture (e.g., repeated patterns or smooth surfaces) and feature movement (e.g. vegetation) (Westoby et al., 2012; Fonstad et al., 2013; Micheletti et al., 2015b).

6.1.2 Uncertainties in SFM-MVS reconstruction of snow-covered surfaces

Reconstructing fresh snow-covered surfaces is a major challenge for SFM-MVS snow depth mapping (Bühler et al., 2015; Harder et al., 2016; Cimoli et al., 2017; Fernandes et al., 2018). Smooth surfaces with little texture are in general difficult to reconstruct with SFM-MVS methods. Smooth surfaces can result in low key-point densities due to images lacking features for matching, which can result in large data gaps or noisy data in the reconstructed surface (Bühler et al., 2016a; Cimoli et al., 2017; Fernandes et al., 2018).

Using a near infrared (NIR) band in images has been found to help mitigate errors caused smooth snow-covered surfaces such as fresh snow (Bühler et al., 2016a). Alternatively, simply waiting a day after fresh snow can substantially improve the quality of the reconstructed surfaces and the resulting accuracy of the snow depths (Gindraux et al., 2017; Fernandes et al., 2018). By just waiting a day after fresh snowfall, subtle features in the snow cover (e.g. from snow drift) can appear that provide textures for good SFM-MVS performance (Fernandes et al., 2018). However, subtle features in the snow-cover topography are only useful under optimal lighting conditions (Bühler et al., 2016a)

Mapping snow-cover topography with cloudy overcast lighting conditions has similar challenges to SFM-MVS reconstruction of fresh snow. Overcast can result in diffuse lighting conditions that reduce the appearance of subtle snow features that can be used for image textures. The surface texture is therefore more homogenous, which results in errors in the reconstructed surface that resembles those of a fresh (i.e. smooth) snow-cover (Harder et al., 2016; Cimoli et al., 2017; Gindraux et al., 2017).

In terms of favourable lighting conditions for reconstruction of snow-covered surfaces, sunlight and shadow are good (Bühler et al., 2016a). Subtle shading variations can give texture to a seemingly texture-less surface (Seitz et al., 2006). Deep shadows, such as produced in steep slope areas with low sun elevation, can cause errors in the SFM-MVS snow depths (Bühler et al., 2016b). However, it was observed in this thesis, when other environmental factors such as slope angle and the image network are considered, the effect of shading contributed very little to the uncertainty in the SFM-MVS DEM. In this study there were large

areas covered by deep shadows. Therefore, this finding may indicate that the benefits of shadows to improve contrast of subtle features may outweigh the negative effect deep shadows have on the reconstruction of snow-covered area.

Overall, like most optical remote sensing processing, the quality of the SFM-MVS modelling is highly dependent on the lighting conditions.

6.2 Quantifying SFM-MVS snow depth uncertainties

Accounting for uncertainty is essential for determining the suitability and describing the limits of the SFM-MVS measured snow depths. As observed in this thesis, even within a short period (e.g., 15 minutes; Goetz et al., 2018), there will be variation in the SFM-MVS elevation models results from one survey to another. This measurement uncertainty is compounded by requiring two separate elevations models that each have their own uncertainties in addition to possible registration errors. However, uncertainties in the SFM-MVS models can be estimated using repeat UAV surveys. Essentially, the observed variation in the snow-covered and snow-free DEMs can be used to create an error propagation model of SFM-MVS snow depths as demonstrated in this thesis.

Error propagation models for DEM differencing are commonly used in topographic change detection analysis to estimate areas where actual changes in DEM elevations are observed. They are used to remove undetectable measurements from an analysis, or to quantifying uncertainty by calculating a range of likely measured values (Anderson, 2019). In topographic change analysis, thresholding is a common method used to reduce positive biases in total erosion and deposition estimates (Wheaton et al., 2010; Lague et al., 2013; James et al., 2017b). Thresholding reduces biases by removing areas that are confidently believed to be stable – i.e. where no statistically significant geomorphic change is detected (Anderson, 2019).

In snow depth mapping, we similarly want to avoid including areas that are snow-free (i.e. stable) from our snow depth calculations and reduce any biases in observed changes in snow distribution. However, thresholds can lead to wrong observations if applied to data consisting of systematic errors (Schaffrath et al., 2015). Due to biases in the SFM-MVS DEMs that can occur from survey design and from geomorphic changes between DEM acquisition dates, thresholds should not be applied for modelling changes in snow distribution from SFM-MVS data. Besides, since a co-registered orthomosaic from the UAV imagery can be easily obtained and used for delineating snow cover, there is no need to use thresholds to reduce biases in snow distribution changes.

Instead, as demonstrated in this thesis, thresholding individual measurements (i.e. at each grid cell) can be used as a tool for visualizing potential sources of errors in the SFM-MVS snow depth map – for example caused by SFM-MVS related systematic error, or from geomorphic changes that have altered the snow-free topography in the time between DEM acquisition dates.

6.2.1 Spatially varying snow depth uncertainty

Modelling the distribution of uncertainties across the surveyed area is important for validating the suitability and determining the limitations of the snow depth data for applications like snowpack modelling (Hedrick et al., 2018). As illustrated in this thesis, many factors can influence uncertainties in the spatial distribution of the SFM-MVS DEM errors which are propagated into the computed snow depths. These factors including UAV survey design, terrain complexity, the presence of vegetation, geomorphic changes in the DEM over time and co-registration errors, can occur in highly heterogeneous spatial patterns, which is a strong reason why a spatially variable propagation model should be applied.

This thesis presented a new method for spatial modelling error propagation in the SFM-MVS snow depths at the grid cell level. By utilizing the repeated DEM observations, a straight forward approach to quantifying the uncertainty in snow depths could be applied based on the Student's *t* distribution. Additionally, it was illustrated how snow depth uncertainty can be expressed by determining the spatially varying error bounds for a given confidence level. This approach has the advantage of being able to communicate to users where and what measurement levels of snow depths can be confidently detected. This contrasts with traditional global or spatially uniform estimates of snow depth uncertainty obtained from reference data that communicates only one uncertainty value for the entire area, which as seen in the results of this work and others does not represent the actual heterogeneous spatial nature of the SFM-MVS elevation model and DEM differencing errors (Tinkham et al., 2014; Cimoli et al., 2018; Adams et al., 2018; Buehler et al. 2017).

6.2.2 Co-registration errors

A major source of error and uncertainty in DEM differencing, and thus SFM-MVS snow depths, are co-registration errors (Nuth and Kääb, 2011; Nolan et al., 2015; Vander Jagt et al., 2015). In this thesis, it was illustrated that with high-quality GNSS surveyed GCPs (e.g. RTK-GNSS that are post-processed using a local base station), additional registration procedures like applying iterative closest point (ICP) algorithms may not always be required for obtaining high-accuracy (< 10 cm) snow depths.

Co-registration of the SFM-MVS DEMs can be challenging, in particular for fresh snow and high snow accumulation periods due to a lack of snow-free (i.e. stable) areas for registration (Bühler et al., 2016b; Marti et al., 2016; Fernandes et al., 2018). The initial SFM reconstruction is generally without scale, or location, and thus ground control is necessary for transforming the reconstruction into real-world coordinates. The registration error can therefore be estimated by comparing the mean error of the snow-on and snow-off DEMs from either an individual set of control points or the GCPs. This comparison provides an estimate of the mean distance of the individual DEMs from the datum, which can be used to approximate the co-registration error.

In general, the co-registration error of the SFM-MVS DEMs is controlled by the precision, accuracy and distribution of the surveyed locations of the ground control (James et al., 2017b; Goetz et al., 2018). Therefore, if necessary, one could include the overall estimate of the vertical accuracy of the ground control as another uncertainty term in the error propagation model.

However, in the case studies in this thesis, the co-registration errors, which were measured as the mean error from the distance from the datum (i.e. GNSS surveyed check points), were below the 1 cm measurement limit of the snow depth pole (- 8 mm for February 22nd and + 6 mm for June 1st). Consequently, if high quality ground control is used for SFM processing, it is likely that the co-registration errors have a negligible impact on SFM-MVS snow depth errors.

However, in the case of combining UAV and satellite-based DEMs, co-registration errors will likely become a larger component of the uncertainty in measured snow depths. Artificial ground control may be required for registering satellite imagery due to a lack of stable areas in the snow-covered area for obtaining high accuracy snow depths in complex terrain (Marti et al., 2016). If stable areas are present between DEMs, affine registration technique can be applied to reduce co-registration errors (Nuth and Kääb, 2011).

6.2.3 SFM-MVS DEM spatial resolution

Depending on terrain complexity, the spatial resolution of the snow-on and snow-off DEMs can affect the accuracy of the SFM-MVS snow depths. In this thesis, it was found for an example of complex terrain in an alpine environment that the accuracy of the snow depths was mainly controlled by the spatial resolution of the snow-off DEM. Additionally, it was observed that in general you can expect a 5 cm increase in the RMSE of snow depth for every meter increase in spatial resolution. This result contrasts findings of others who found little variation in SFM-MVS snow depth accuracy for spatial resolutions less than 2 m (Marti et al., 2016; Michele et al., 2016). These studies were conducted in relatively more gentle alpine terrain than the case study in this thesis.

The effects of the spatial resolution on the accuracy of DEM differencing is not only important for snow depth detection, but also in topographic change detection. It has been observed in high alpine environments that error in DEM differencing increases with lower spatial resolution (i.e. lower point densities), higher surface roughness (e.g., coarse-rocky debris material), and steeper slopes (Liu et al., 2007; Guo et al., 2010; Sailer et al., 2014). That is, uncertainties in DEM differencing increase as terrain complexity increases, which was observed in this study as well.

In general, since small scale variability in snowpack is correlated to local variability in topography (López-Moreno et al., 2015; Cimoli et al., 2017), it is recommended that higher snow-off DEM resolutions are used for complex terrain to reduce snow depth errors from DEM differencing. Higher spatial resolutions can be obtained by increasing the point density of the SFM-MVS reconstruction by for example flying UAV surveys closer to the ground, and by waiting for optimal snow texture and lighting conditions.

6.2.4 Errors from vegetation

Although this thesis focused on alpine areas with very low vegetation, the presence of vegetation can have a strong influence on the SFM-MVS based snow depth values (Bühler et al., 2015; Nolan et al., 2015; Harder et al., 2016; Cimoli et al., 2017; Fernandes et al., 2018).

Vegetation can lead to underestimating snow depths because the snow-free elevations are overestimated (Bühler et al., 2015).

The exact influence of vegetation on errors in SFM-MVS snow depth has yet to be examined in detail. Perhaps by modelling the bias in snow depth errors from vegetation corrections could be applied (Nolan et al., 2015). Tinkham et al. (2014) investigated the bias in lidar snow depths related to different vegetation cover using random forest regression based on field measurements; a similar approach could be done to determine SFM-MVS snow depth biases related to vegetation.

Lidar remains to be the best solution for high-resolution surveying of the snow-free topography beneath vegetation cover (Wallace et al., 2016). Combining lidar snow-free DEMs with SFM-MVS snow-covered DEMs is probably the most convenient approach to reducing errors from vegetation (Bühler et al., 2015; Cimoli et al., 2017). Due to these issues with snow depth mapping in vegetated areas, SFM-MVS methods seem to be most appropriate for high-alpine areas (i.e. above the tree-line) and periglacial landscapes that have very shallow or no vegetation.

6.3 Correcting SFM-MVS snow depths in active alpine terrain

One of the main challenges in SFM-MVS snow depth mapping in alpine areas is accounting for uncertainties in snow depths related to sub-snow surface elevation changes occurring between UAV survey acquisition dates (Nolan et al., 2015; Bühler et al., 2016a). In this thesis, it was found that depending on the time between DEM acquisition, slope deformation processes such as permafrost creep, can considerably contribute to uncertainties in high spatial-resolution snow depth maps in alpine areas. Additionally, depending on the terrain complexity and deformation processes, the spatial pattern of snow depth uncertainties can be highly heterogeneous. To account for this uncertainty this thesis illustrated that modelling and applying appropriate scaling of sub-snow surface deformations can substantially reduce snow depth errors. These snow depth corrections can help provide more reliable snow distribution data.

Correcting snow depths from DEM differencing (e.g., from SFM-MVS and lidar) is also important for accurate estimates of snow accumulation on glaciers for winter mass balance and ice thickness distribution (Abermann et al., 2010; Sold et al., 2013; Helfricht et al., 2014; Schöber et al., 2014; Brun et al., 2018). Uncertainties in estimating glacier snow accumulation can occur due to firn compaction and ice flow occurring between the DEM surveys (Sold et al., 2013; Schöber et al., 2014). Sold et al. (2013) provided a similar method for correcting snow depths as presented in this thesis, which was applied for glacier snow accumulation. However, their approach estimates and scales only the vertical displacement of the sub-snow surface (i.e. the ice surface) caused by glacier flow. The approach in this thesis applied a correction to the snow depths by modelling both horizontal and vertical displacements (i.e. 3D displacements) of the sub-snow surface.

Accounting for the horizontal and vertical displacement of the deforming snow-free surface is important for correcting snow depths from sub-snow surface flow movement. For example,

only modelling of the vertical displacements can result in implausible geomorphic changes of the estimated surfaces that may introduce snow depth errors (**Figure 23**). In contrast, a scaled 3D displacement model like the one presented in this thesis can produce a more realistic representation of elevation changes over time that occur due to downslope movements of surface topography.

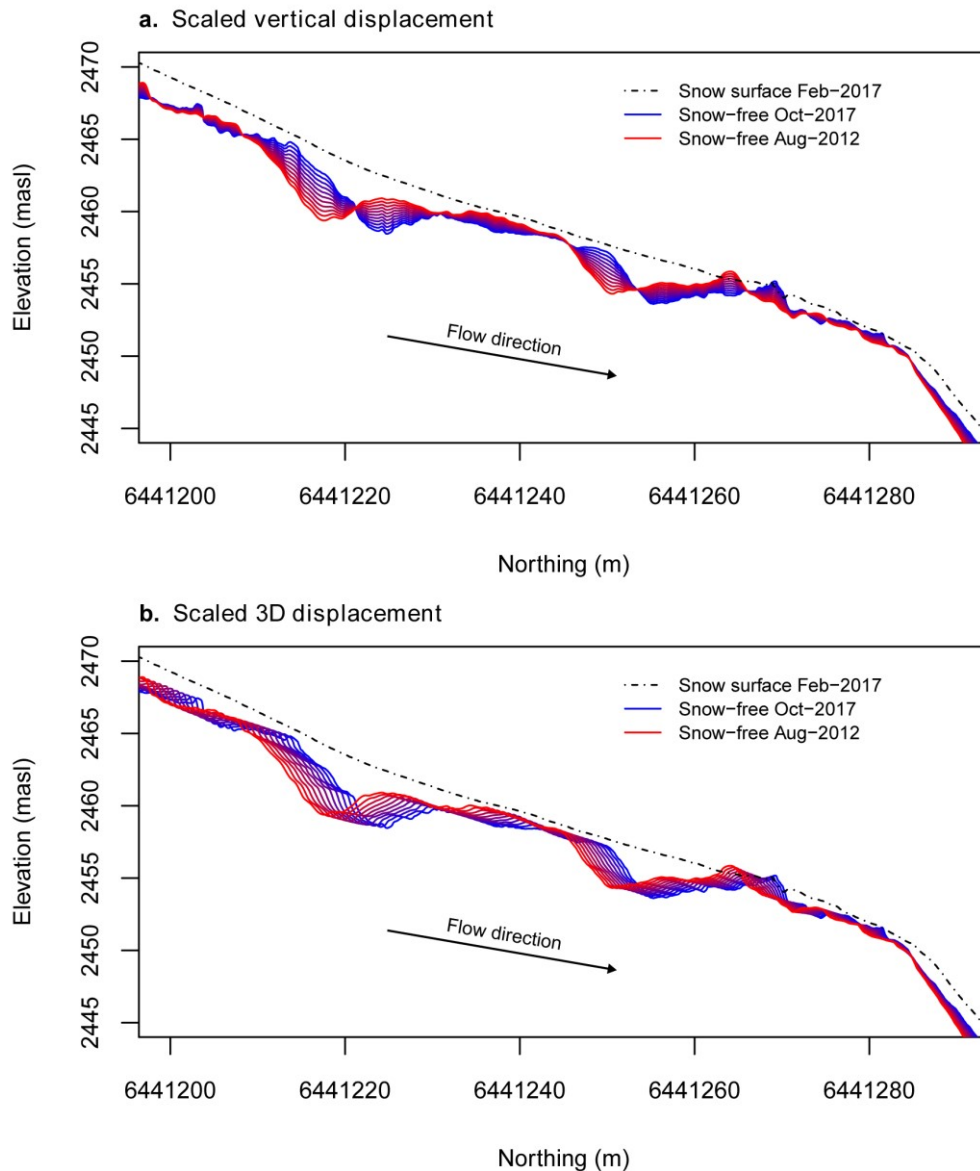


Figure 23. Profile of the rock glacier front illustrating transformed snow-free surfaces represented by (a.) scaling a model of only the vertical of displacements over time and (b.) by scaling a model of the 3D displacements over time. The transition colours from red to blue represent the modelled change in the snow-free rock glacier surface from 2012 (red) to 2017 (blue) obtained by scaling the modelled displacements using factors from 0 to 1 with a step of 0.1. The dotted line represents the snow-cover surface on 22-Feb-2017. The first plot (a.) shows that scaling only the vertical displacements does not capture the transition in elevations over time due to the movement of the rock glacier. The second plot (b.) shows how scaling modelled 3D displacements more realistically represents the elevation changes over time.

6.3.1 In-situ measurements to constrain snow depth corrections

When applying deformation models to correct for snow depth or ice thickness, in-situ measurements are important for constraining the model (Sold et al. 2013; Brun et al., 2018; Rabatel et al., 2018). In this thesis, it was shown that the use of in-situ snow depth measurements from probing was crucial for constraining the transformation of the snow-free DEMs to correct for errors due to surface deformations of the sub-snow topography. Otherwise, the deforming rate can be approximated based on average movement rates; however this approach may not account for temporal variations in the movement rates.

Similar to the findings in this thesis, Sold et al (2013) found that the error in snow depths over a glacier were substantially reduced by correcting for sub-snow surface deformations occurring between the DEM acquisitions. Additionally, they found that the greatest reduction in depth errors came from calibrating the correction using a factor that was optimized using in-situ snow depths from probing. Just as found in this thesis, this better result was due to the ability to account for interannual and seasonal variations in the sub-snow surface (i.e. glacier surface) deformation.

In addition to in-situ measurements, the work in thesis also demonstrated a novel approach to constrain deformation models using snow-free areas in the DEM where ground deformation is occurring. For spring snowpack conditions, using snow-free areas to calibrate the deformation model means having to spend less time in the field snow probing.

6.4 Future work

6.4.1 Benchmarking SFM-MVS algorithms

The DEMs for computing snow depths in this thesis were derived from only one SFM-MVS 3D reconstruction software: Agisoft PhotoScan. However, there are many other commercial and open-source software available that may result in different reconstructions (Niederheiser et al., 2016). Therefore, future work remains in benchmarking SFM and MVS algorithms for reconstructing snow-covered surfaces. For example, different MVS algorithms can be tested to deal with gaps in the point cloud data due to occlusions or lack of features (e.g. surface evolution techniques) (Tagliasacchi et al., 2011).

In commercial SFM-MVS software such as PhotoScan and Pix4D it is difficult to control the reconstruction workflow; however, open-source software like MicMac provides a flexible environment to customize the SFM-MVS solution (Rupnik et al., 2017).

Benchmarking can be challenging due to random sub-procedures in SFM that can influence the errors in the 3D reconstruction (Dickscheid et al., 2008). Therefore, repeated surveys, such as illustrated in this thesis, may provide suitable data for benchmarking because some of the random errors in individual SFM-MVS processing steps can be accounted for. This data is also not limited to SFM-MVS processing for snow depth, it is also relevant for elevation modelling in general. Furthermore, other factors should be considered. For example, if aim of the SFM-MVS snow depth data is to assist in real-time snowpack modelling, similar to examples with lidar (Hedrick et al., 2018), the ability to reduce processing time and self-determine systematic errors remains important (Dickscheid et al., 2008).

In general, SFM-MVS performance varies from site to site, and the future of SFM-MVS mapping will likely focus on determining optimal workflows to obtain a high quality 3D reconstruction for a given application.

6.4.2 Applying SFM-MVS snow depths for snow modelling

Given the proven quality of SFM-MVS snow depth observations, and the ability of UAVs to help acquire frequent observations, SFM-MVS techniques are suitable for mapping snow distribution. They also may have the benefit of being less costly to operate than traditional airborne lidar systems (Buehler et al., 2016; Webb et al., 2018).

Currently, few studies have used SFM-MVS snow depths for analysis of snow distribution (Harder et al., 2016; Fernandes et al., 2018). This is therefore a promising area for research growth. As demonstrated in this work, a major advantage of SFM-MVS snow depth mapping is the ability to quantify the spatial distribution of measurement uncertainties in a rather uncomplicated approach (e.g. repeat surveys). Therefore, for monitoring changes of snow depth over time, the methods presented in this thesis are recommended to be applied to ensure that reliable observations are being made.

Snow depth observations are not enough to determine water content of a snowpack, information on the snowpack density is also required. Therefore, in addition to monitoring snow surface elevation changes, SFM-MVS snow depth data can be integrated into numerical snowpack models (e.g. Crocus, SNOWPACK and iSnobal) for modelling local hydrological conditions as done recently with lidar data (Painter et al, 2016; Revuelto et al., 2016; Hedrick et al, 2018). Constraining numerical snow models by updating snow depth distribution data has seen improvements in the accuracy of snow disappearance dates (Revuelto et al., 2016), snow melt patterns (Hedrick et al., 2018), and run-off (Brauchli et al., 2017) in alpine environments. Furthermore, a strong understanding of snow depth uncertainties is required since the performance of snowpack modelling is dependent on the uncertainties of their model variables (Revuelto et al. 2016; Hedrick et al., 2018).

Therefore, combining distributed snow distribution models with high spatial-temporal snow depth data acquired from UAV imagery and SFM-MVS processing has potential to improve our prediction of snow pattern changes and snowpack evolution. High-resolution snow depth data also has the possibility to improve liquid water content estimation by fusing with ground penetrating radar data (Webb et al., 2018).

6.5 Conclusions

The goal of this thesis was to improve our understanding of the uncertainties in snow depth mapping using UAVs and SFM-MVS. To obtain this goal, novel methods for quantifying, characterizing and correcting errors were presented in this thesis.

Although this thesis focused on snow depth mapping, the mapping of DEM uncertainty, determining spatially varying detection limits, and surface deformation modelling are

methods that may also be applied for improving Earth surface process and landform monitoring from UAV data and SFM-MVS 3D modelling.

Here, a summary of the main conclusions of this thesis is presented.

1. Due to the sensitivity of SFM-MVS reconstruction performance to SFM-MVS processing, UAV survey design and environmental factors, performing detailed analysis of the elevation model errors is essential for assuring the quality of any corresponding geoscientific analysis – including snow depth mapping. As presented in this thesis, uncertainty estimation from repeated surveys is a crucial tool for investigating sources of errors in SFM-MVS elevation models. Additionally, by quantifying the spatial distribution of SFM-MVS uncertainties, the effects of UAV survey design for a field site can be investigated, which help to improve survey design to reduce SFM-MVS errors for a given application.
2. In this thesis, the image height, distribution of GCPs and image overlap were found to have the strongest influence on the uncertainty in DEMs derived from SFM-MVS reconstruction in ideal snow cover surface conditions (i.e., textured snow). These are factors that can be controlled by the survey design and can therefore be optimized to obtain a desired survey quality. Since fresh snow cover and overcast lighting conditions can also lead to errors in the elevation models due to poor SFM-MVS reconstruction of a low texture surface, considering the timing of the UAV surveying is also important for reducing model uncertainties.
3. The uncertainties in SFM-MVS snow depths can be spatially highly heterogeneous. The main contributors to uncertainty are the quality of the SFM-MVS derived snow-free and snow-covered elevation models and the quality of co-registration. Mapping these uncertainties is important for communicating the quality of the computed snow depths. As presented and discussed in this thesis, spatially varying error propagation models, which can be expressed as detection limits, can be determined from repeated UAV surveys. Additionally, since random variations in error can result from the UAV survey design and random procedures in the SFM processing, this work illustrated that the Student's t distribution can be applied to a set of repeated UAV observations to determine if the observed snow depths (i.e., difference in elevations) could occur due to chance alone.
4. In complex alpine terrain (i.e., coarse material and steep), having a very fine resolution snow-off DEM can reduce errors in the computed snow depths. Due to the gentler topography, the spatial resolution of the snow-on DEM has a much smaller effect on snow depth accuracy. Interestingly, there was little variation in the snow depth accuracy in spatial resolutions finer than 5 m when a high-resolution (<10 cm) snow-off DEM was used for computing depths. Also, it was generally observed that when the spatial resolution of the snow-on and snow-off DEMs were both coarsened, the RMSE measured by probing tends to increase 5 cm for every 1 m increase in resolution.

5. The methods for uncertainty analysis based on repeated UAV surveys presented in this thesis are independent from any SFM-MVS software. Consequently, this thesis has developed a framework in which comparing the performance of SFM-MVS methods can be standardized. Being able to adequately assess the performance of different SFM-MVS elevation models can assist in determining best practices for SFM-MVS snow depth mapping.
6. Changes in the ground surface between acquired snow-free and snow-covered DEMs can contribute considerably to errors in the computed snow depths. A novel approach based on kinematic surface deformation modelling to correct errors due to on-going creep was presented in this thesis. The key component of the corrections was ensuring that the modelled surface beneath the snow-cover was accurately scaled (i.e., transformed). Currently, the best approach for all snow cover conditions is to constrain the scaling of the deformation model using in-situ snow depths from probing. However, in sparse snow cover conditions, such as during the melt period, areas in the snow-on elevation model that are snow-free can also be useful for constraining the scaling. Both these methods can account for variations in deformation rates over time.

Future work can focus on improving SFM-MVS methods for reconstructing various snow-cover conditions, the application of SFM-MVS snow depth data for monitoring patterns of snow distribution change, and local modelling of snowpack characteristics. For example, SFM and MVS algorithms can be benchmarked using repeatedly surveyed UAV data to determine which are better at reducing model uncertainties. Error propagation models can be applied to ensure quality analysis of snow depth changes. Additionally, fusing SFM-MVS snow depth data with numerical models may lead to novel insights regarding local snowpack characteristics.

Overall, implementing uncertainty analysis and correcting snow depth data is recommended not only to provide strong support for the quality of the SFM-MVS derived snow depths, but also to find areas where the SFM-MVS approach and UAV surveying can be improved. Given the potential stresses on water supply from a warmer climate, having quality snow depth distribution data is essential for assisting in future water resource management decisions.

References

- Arya, S., Mount, D. M., Netanyahu, N. S., Silverman, R., Wu, A. Y., 1998. An optimal algorithm for approximate nearest neighbor searching fixed dimensions. *Journal of the ACM (JACM)*, 45(6), 891-923.
- Abermann, J., Fischer, A., Lambrecht, A., Geist, T., 2010. On the potential of very high-resolution repeat DEMs in glacial and periglacial environments. *The Cryosphere* 4 (1), 53–65.
- Adams, M.S., Bühler, Y., Fromm, R., 2018. Multitemporal Accuracy and Precision Assessment of Unmanned Aerial System Photogrammetry for Slope-Scale Snow Depth Maps in Alpine Terrain. *Pure and Applied Geophysics* 175 (9), 3303–3324.
- Alahi, A., Ortiz, R., Vandergheynst, P., 2012. FREAK: Fast Retina Keypoint. *IEEE Conference on Computer Vision and Pattern Recognition (CVPR)*, 2012. 16-21 June 2012, Providence, RI, USA, *IEEE Conference on Computer Vision and Pattern Recognition; CVPR; IEEE Computer Society Conference on Computer Vision and Pattern Recognition*. IEEE, Piscataway, NJ, pp. 510–517.
- Anderson, S.W., 2019. Uncertainty in quantitative analyses of topographic change: error propagation and the role of thresholding. *Earth Surface Processes and Landforms* 44 (5), 1015–1033.
- Apaloo, J., Brenning, A., Bodin, X., 2012. Interactions between Seasonal Snow Cover, Ground Surface Temperature and Topography (Andes of Santiago, Chile, 33.5°S). *Permafrost and Periglacial Processes* 23 (4), 277–291.
- Avanzi, F., Bianchi, A., Cina, A., Michele, C. de, Maschio, P., Pagliari, D., Passoni, D., Pinto, L., Piras, M., Rossi, L., 2018. Centimetric Accuracy in Snow Depth Using Unmanned Aerial System Photogrammetry and a MultiStation. *Remote Sensing* 10 (5), 765.
- Bangen, S., Hensleigh, J., McHugh, P., Wheaton, J., 2016. Error modeling of DEMs from topographic surveys of rivers using fuzzy inference systems. *Water Resources Research* 52 (2), 1176–1193.
- Barnett, T.P., Adam, J.C., Lettenmaier, D.P., 2005. Potential impacts of a warming climate on water availability in snow-dominated regions. *Nature* 438 (7066), 303–309.
- Barrand, N.E., Murray, T., James, T.D., Barr, S.L., Mills, J.P., 2009. Optimizing photogrammetric DEMs for glacier volume change assessment using laser-scanning derived ground-control points 55 (189), 106–116.
- Bartlett, J.W., Frost, C., 2008. Reliability, repeatability and reproducibility: analysis of measurement errors in continuous variables. *Ultrasound in obstetrics & gynecology : the official journal of the International Society of Ultrasound in Obstetrics and Gynecology* 31 (4), 466–475.
- Bemis, S.P., Micklethwaite, S., Turner, D., James, M.R., Akciz, S., Thiele, S.T., Bangash, H.A., 2014. Ground-based and UAV-Based photogrammetry: A multi-scale, high-resolution mapping tool for structural geology and paleoseismology. *Journal of Structural Geology* 69, 163–178.
- Benassi, F., Dall'Asta, E., Diotri, F., Forlani, G., Di Morra Cella, U., Roncella, R., Santise, M., 2017. Testing Accuracy and Repeatability of UAV Blocks Oriented with GNSS-Supported Aerial Triangulation. *Remote Sensing* 9 (2), 172.
- Bernard, É., Friedt, J.M., Tolle, F., Griselin, M., Marlin, C., Prokop, A., 2017. Investigating snowpack volumes and icing dynamics in the moraine of an Arctic catchment using UAV photogrammetry. *The Photogrammetric Record* 32 (160), 497–512.
- Berthier, E., Arnaud, Y., Vincent, C., Rémy, F., 2006. Biases of SRTM in high-mountain areas. Implications for the monitoring of glacier volume changes. *Geophysical Research Letters* 33 (8), 382.
- Bodin, X., Thibert, E., Fabre, D., Ribolini, A., Schoeneich, P., Francou, B., Reynaud, L., Fort, M., 2009. Two decades of responses (1986 - 2006) to climate by the Laurichard rock glacier, French Alps. *Permafrost and Periglacial Processes* 20 (4), 331–344.
- Borradaile, G., 2002. *Statistics of earth science data. Their distribution in time, space and orientation*. Springer, New York, London.
- Brasington, J., Langham, J., Rumsby, B., 2003. Methodological sensitivity of morphometric estimates of coarse fluvial sediment transport. *Geomorphology* 53 (3-4), 299–316.

- Brasington, J., Rumsby, B.T., McVey, R.A., 2000. Monitoring and modelling morphological change in a braided gravel-bed river using high resolution GPS-based survey. *Earth Surface Processes and Landforms* 25 (9), 973–990.
- Brauchli, T., Trujillo, E., Huwald, H., Lehning, M., 2017. Influence of Slope-Scale Snowmelt on Catchment Response Simulated With the Alpine3D Model. *Water Resources Research* 53 (12), 10723–10739.
- Brun, F., Wagnon, P., Berthier, E., Shea, J.M., Immerzeel, W.W., Kraaijenbrink, P.D.A., Vincent, C., Reverchon, C., Shrestha, D., Arnaud, Y., 2018. Ice cliff contribution to the tongue-wide ablation of Changri Nup Glacier, Nepal, central Himalaya. *The Cryosphere* 12 (11), 3439–3457.
- Brunier, G., Fleury, J., Anthony, E.J., Gardel, A., Dussouillez, P., 2016. Close-range airborne Structure-from-Motion Photogrammetry for high-resolution beach morphometric surveys. Examples from an embayed rotating beach. *Geomorphology* 261, 76–88.
- Bühler, Y., Adams, M.S., Bösch, R., Stoffel, A., 2016a. Mapping snow depth in alpine terrain with unmanned aerial systems (UAS). Potential and limitations. *The Cryosphere*, 1075–1088.
- Bühler, Y., Adams, M.S., Stoffel, A., Boesch, R., 2016b. Photogrammetric reconstruction of homogenous snow surfaces in alpine terrain applying near-infrared UAS imagery. *International Journal of Remote Sensing* 38 (8-10), 3135–3158.
- Bühler, Y., Christen, M., Kowalski, J., Bartelt, P., 2011. Sensitivity of snow avalanche simulations to digital elevation model quality and resolution. *Annals of Glaciology* 52 (58), 72–80.
- Bühler, Y., Marty, M., Egli, L., Veitinger, J., Jonas, T., Thee, P., Ginzler, C., 2015. Snow depth mapping in high-alpine catchments using digital photogrammetry. *The Cryosphere* 9 (1), 229–243.
- Burns, W.J., Coe, J.A., Kaya, B.S., Ma, L., 2010. Analysis of Elevation Changes Detected from Multi-Temporal LiDAR Surveys in Forested Landslide Terrain in Western Oregon. *Environmental and Engineering Geoscience* 16 (4), 315–341.
- Carbonneau, P.E., Dietrich, J.T., 2017. Cost-effective non-metric photogrammetry from consumer-grade sUAS. Implications for direct georeferencing of structure from motion photogrammetry. *Earth Surface Processes and Landforms* 42 (3), 473–486.
- Carlisle, B.H., 2005. Modelling the Spatial Distribution of DEM Error. *Transactions in GIS* 9 (4), 521–540.
- Carrivick, J., Quincey, D., Smith, M., 2016. *Structure from motion in the geosciences*. Wiley Blackwell, Chichester, West Sussex, SQ, UK, Ames, Iowa.
- Cimoli, E., Marcer, M., Vandecrux, B., Bøggild, C.E., Williams, G., Simonsen, S.B., 2017. Application of Low-Cost UASs and Digital Photogrammetry for High-Resolution Snow Depth Mapping in the Arctic. *Remote Sensing* 9 (11), 1144.
- Clapuyt, F., Vanacker, V., van Oost, K., 2016. Reproducibility of UAV-based earth topography reconstructions based on Structure-from-Motion algorithms. *Geomorphology* 260, 4–15.
- Cline, D.W., 1993. Measuring alpine snow depths by digital photogrammetry Part 1. Conjugate point identification. *Proceedings of 50th Eastern Snow Conference, Quebec City*, 265–271.
- Cline, D.W., 1994. Digital photogrammetric determination of alpine snowpack distribution for hydrologic modeling. *Proceedings of the Western Snow Conference, Colorado State University, CO, USA*.
- Colomina, I., Molina, P., 2014. Unmanned aerial systems for photogrammetry and remote sensing. A review. *ISPRS Journal of Photogrammetry and Remote Sensing* 92, 79–97.
- Csanyi, N., Toth, C.K., 2007. Improvement of Lidar Data Accuracy Using Lidar-Specific Ground Targets. *Photogrammetric Engineering & Remote Sensing* 73 (4), 385–396.
- Dandois, J., Olano, M., Ellis, E., 2015. Optimal Altitude, Overlap, and Weather Conditions for Computer Vision UAV Estimates of Forest Structure. *Remote Sensing* 7 (10), 13895–13920.
- Deems, J.S., Fassnacht, S.R., Elder, K.J., 2006. Fractal Distribution of Snow Depth from Lidar Data. *Journal of Hydrometeorology* 7 (2), 285–297.
- Deems, J.S., Painter, T.H., Finnegan, D.C., 2013. Lidar measurement of snow depth. A review. *Journal of Glaciology* 59 (215), 467–479.

- Delaloye, R., Lambiel, C., Gärtner-Roer, I., 2010. Overview of rock glacier kinematics research in the Swiss Alps. *Geographica Helvetica* 65 (2), 135–145.
- Dickscheid, T., Labe, T., Förstner, W., 2008. Benchmarking Automatic Bundle Adjustment Results. In: Chen, J., Jiang, J., Förstner, W. (Eds.), *21st Congress of the International Society for Photogrammetry and Remote Sensing (ISPRS)*, pp. 7–12.
- Elder, K., Dozier, J., Michaelsen, J., 1991. Snow accumulation and distribution in an Alpine Watershed. *Water Resources Research* 27 (7), 1541–1552.
- Favalli, M., Fornaciai, A., Isola, I., Tarquini, S., Nannipieri, L., 2012. Multiview 3D reconstruction in geosciences. *Computers & Geosciences* 44, 168–176.
- Fernandes, R., Prevost, C., Canisius, F., Leblanc, S.G., Maloley, M., Oakes, S., Holman, K., Knudby, A., 2018. Monitoring snow depth change across a range of landscapes with ephemeral snowpacks using structure from motion applied to lightweight unmanned aerial vehicle videos. *The Cryosphere* 12 (11), 3535–3550.
- Fischler, M.A., Bolles, R.C., 1981. Random sample consensus. A paradigm for model fitting with applications to image analysis and automated cartography. *Communications of the ACM* 24 (6), 381–395.
- Fisher, P., 1998. Improved Modeling of Elevation Error with Geostatistics. *GeoInformatica* 2 (3), 215–233.
- Fisher, P.F., Tate, N.J., 2006. Causes and consequences of error in digital elevation models. *Progress in Physical Geography* 30 (4), 467–489.
- Fonstad, M.A., Dietrich, J.T., Courville, B.C., Jensen, J.L., Carbonneau, P.E., 2013. Topographic structure from motion. A new development in photogrammetric measurement. *Earth Surface Processes and Landforms* 38 (4), 421–430.
- Francou, B., Reynaud, L., 1992. 10 year surficial velocities on a rock glacier (Laurichard, French Alps). *Permafrost and Periglacial Processes* 3 (3), 209–213.
- Furukawa, Y., Hernández, C., 2015. Multi-View Stereo. A Tutorial. *Foundations and Trends® in Computer Graphics and Vision* 9 (1-2), 1–148.
- Gindraux, S., Boesch, R., Farinotti, D., 2017. Accuracy Assessment of Digital Surface Models from Unmanned Aerial Vehicles' Imagery on Glaciers. *Remote Sensing* 9 (2), 186.
- Goetz, J., Brenning, A., Marcer, M., Bodin, X., 2018. Modeling the precision of structure-from-motion multi-view stereo digital elevation models from repeated close-range aerial surveys. *Remote Sensing of Environment* 210, 208–216.
- Goetz, J., Marcer, M., Brenning, A., Bodin, X., 2019. UAV imagery and in-situ measurements for structure-from-motion snow depth mapping over the Laurichard rock glacier, France - surveyed in 2017. *Mendeley Data*, V1.
- Granshaw, S.I., 1980. Bundle adjustment methods in engineering photogrammetry. *The Photogrammetric Record* 10 (56), 181–207.
- Grünwald, T., Bühler, Y., Lehning, M., 2014. Elevation dependency of mountain snow depth. *The Cryosphere* 8 (6), 2381–2394.
- Guo, Q., Li, W., Yu, H., Alvarez, O., 2010. Effects of Topographic Variability and Lidar Sampling Density on Several DEM Interpolation Methods. *Photogrammetric Engineering & Remote Sensing* 76 (6), 701–712.
- Haberkorn, A., Phillips, M., Kenner, R., Rhyner, H., Bavay, M., Galos, S.P., Hoelzle, M., 2016. Thermal regime of rock and its relation to snow cover in steep alpine rock walls. *Gemsstock, central swiss alps. Geografiska Annaler: Series A, Physical Geography* 97 (3), 579–597.
- Harder, P., Schirmer, M., Pomeroy, J., Helgason, W., 2016. Accuracy of snow depth estimation in mountain and prairie environments by an unmanned aerial vehicle. *The Cryosphere* 10 (6), 2559–2571.
- Harris, C., Stephens, M., 1988. A Combined Corner and Edge Detector. In: Taylor, C.J. (Ed.), *Proceedings of the Alvey Vision Conference 1988*. Alvey Vision Club, 23.1-23.6.

- Harwin, S., Lucieer, A., 2012. Assessing the Accuracy of Georeferenced Point Clouds Produced via Multi-View Stereopsis from Unmanned Aerial Vehicle (UAV) Imagery. *Remote Sensing* 4 (12), 1573–1599.
- Harwin, S., Lucieer, A., Osborn, J., 2015. The Impact of the Calibration Method on the Accuracy of Point Clouds Derived Using Unmanned Aerial Vehicle Multi-View Stereopsis. *Remote Sensing* 7 (9), 11933–11953.
- Hastie, T.J., Tibshirani, R.J., 1990. *Generalized Additive Models*. Chapman and Hall, London, UK.
- Hedrick, A.R., Marks, D., Havens, S., Robertson, M., Johnson, M., Sandusky, M., Marshall, H.-P., Kormos, P.R., Bormann, K.J., Painter, T.H., 2018. Direct Insertion of NASA Airborne Snow Observatory-Derived Snow Depth Time Series Into the iSnobal Energy Balance Snow Model. *Water Resources Research* 18 (3), 435.
- Helfricht, K., Kuhn, M., Keuschnig, M., Heilig, A., 2014. Lidar snow cover studies on glaciers in the Ötztal Alps (Austria): comparison with snow depths calculated from GPR measurements. *The Cryosphere* 8 (1), 41–57.
- Helfricht, K., Schöber, J., Seiser, B., Fischer, A., Stötter, J., Kuhn, M., 2012. Snow accumulation of a high alpine catchment derived from LiDAR measurements. *Advances in Geosciences* 32, 31–39.
- Hendrickx, H., Vivero, S., Cock, L. de, Wit, B. de, Maeyer, P. de, Lambiel, C., Delaloye, R., Nyssen, J., Frankl, A., 2019. The reproducibility of SfM algorithms to produce detailed Digital Surface Models: the example of PhotoScan applied to a high-alpine rock glacier. *Remote Sensing Letters* 10 (1), 11–20.
- Hiemstra, C.A., Liston, G.E., Reiners, W.A., 2006. Observing, modelling, and validating snow redistribution by wind in a Wyoming upper treeline landscape. *Ecological Modelling* 197 (1–2), 35–51.
- Holmes, K.W., Chadwick, O.A., Kyriakidis, P.C., 2000. Error in a USGS 30-meter digital elevation model and its impact on terrain modeling. *Journal of Hydrology* 233 (1-4), 154–173.
- Hopkinson, C., Collins, T., Anderson, A., Pomeroy, J., Spooner, I., 2012. Spatial Snow Depth Assessment Using LiDAR Transect Samples and Public GIS Data Layers in the Elbow River Watershed, Alberta. *Canadian Water Resources Journal / Revue canadienne des ressources hydriques* 37 (2), 69–87.
- Hugenholtz, C.H., Whitehead, K., Brown, O.W., Barchyn, T.E., Moorman, B.J., LeClair, A., Riddell, K., Hamilton, T., 2013. Geomorphological mapping with a small unmanned aircraft system (sUAS). Feature detection and accuracy assessment of a photogrammetrically-derived digital terrain model. *Geomorphology* 194, 16–24.
- Ikeda, A., Matsuoka, N., Kääh, A., 2008. Fast deformation of perennially frozen debris in a warm rock glacier in the Swiss Alps. An effect of liquid water. *Journal of Geophysical Research* 113 (F1), 212.
- Immerzeel, W.W., Kraaijenbrink, P.D.A., Shea, J.M., Shrestha, A.B., Pellicciotti, F., Bierkens, M.F.P., Jong, S.M. de, 2014. High-resolution monitoring of Himalayan glacier dynamics using unmanned aerial vehicles. *Remote Sensing of Environment* 150, 93–103.
- James, M.R., Robson, S., 2012. Straightforward reconstruction of 3D surfaces and topography with a camera. Accuracy and geoscience application. *Journal of Geophysical Research: Earth Surface* 117, F03017.
- James, M.R., Robson, S., 2014. Mitigating systematic error in topographic models derived from UAV and ground-based image networks. *Earth Surface Processes and Landforms* 39 (10), 1413–1420.
- James, M.R., Robson, S., d'Oleire-Oltmanns, S., Niethammer, U., 2017a. Optimising UAV topographic surveys processed with structure-from-motion. Ground control quality, quantity and bundle adjustment. *Geomorphology* 280, 51–66.
- James, M.R., Robson, S., Smith, M.W., 2017b. 3-D uncertainty-based topographic change detection with structure-from-motion photogrammetry: Precision maps for ground control and directly georeferenced surveys. *Earth Surface Processes and Landforms* 42, 1769–1788.
- Javernick, L., Brasington, J., Caruso, B., 2014. Modeling the topography of shallow braided rivers using Structure-from-Motion photogrammetry. *Geomorphology* 213, 166–182.

- Jonas, T., Rixen, C., Sturm, M., Stoeckli, V., 2008. How alpine plant growth is linked to snow cover and climate variability. *Journal of Geophysical Research* 113 (G3), 377.
- Kazhdan, M., Bolitho, M., Hoppe, H., 2006. Poisson surface reconstruction. In: Polthier, K., Sheffer, A. (Eds.), *Eurographics Symposium on Geometry and Processes*.
- Kirchner, P.B., Bales, R.C., Molotch, N.P., Flanagan, J., Guo, Q., 2014. LiDAR measurement of seasonal snow accumulation along an elevation gradient in the southern Sierra Nevada, California. *Hydrology and Earth System Sciences* 18 (10), 4261–4275.
- Kyriakidis, P.C., Shortridge, A.M., Goodchild, M.F., 1999. Geostatistics for conflation and accuracy assessment of digital elevation models. *International Journal of Geographical Information Science* 13 (7), 677–707.
- Lague, D., Brodu, N., Leroux, J., 2013. Accurate 3D comparison of complex topography with terrestrial laser scanner. Application to the Rangitikei canyon (N-Z). *ISPRS Journal of Photogrammetry and Remote Sensing* 82, 10–26.
- Lancaster, G.A., Dodd, S., Williamson, P.R., 2004. Design and analysis of pilot studies: recommendations for good practice. *Journal of evaluation in clinical practice* 10 (2), 307–312.
- Lane, S.N., Westaway, R.M., Murray Hicks, D., 2003. Estimation of erosion and deposition volumes in a large, gravel-bed, braided river using synoptic remote sensing. *Earth Surface Processes and Landforms* 28 (3), 249–271.
- Lemke, P., Ren, J., Alley, R.B., Allison, I., Carrasco, J., Flato, G., Fujii, Y., Kaser, G., Mote, P., Thomas, R.H., Zhang, T., 2007. Observations: Changes in Snow, Ice and Frozen Ground. In: Parry, M.L. (Ed.), *Climate change 2007: The physical science basis; summary for policymakers, technical summary and frequently asked questions. Part of the Working Group I contribution to the Fourth Assessment Report of the Intergovernmental Panel on Climate Change*.
- Leutenegger, S., Chli, M., Siegwart, R.Y., 2011. BRISK: Binary Robust invariant scalable keypoints. *ICCV 2011. 13th International Conference on Computer Vision : 6-13 November 2011, Barcelona, Spain. [IEEE], [Piscataway, N.J.]*, pp. 2548–2555.
- Li, J., Li, E., Chen, Y., Xu, L., Zhang, Y., 2010. Bundled depth-map merging for multi-view stereo. *IEEE Conference on Computer Vision and Pattern Recognition (CVPR)*, pp. 2769–2776.
- Litaor, M.I., Williams, M., Seastedt, T.R., 2008. Topographic controls on snow distribution, soil moisture, and species diversity of herbaceous alpine vegetation, Niwot Ridge, Colorado. *Journal of Geophysical Research* 113 (G2), n/a-n/a.
- Liu, X., Zhang, Z., Peterson, J., Chandra, S., 2007. LiDAR-Derived High Quality Ground Control Information and DEM for Image Orthorectification. *GeoInformatica* 11 (1), 37–53.
- López-Moreno, J.I., Fassnacht, S.R., Beguería, S., Latron, J.B.P., 2011. Variability of snow depth at the plot scale. Implications for mean depth estimation and sampling strategies. *The Cryosphere* 5 (3), 617–629.
- López-Moreno, J.I., Revuelto, J., Fassnacht, S.R., Azorín-Molina, C., Vicente-Serrano, S.M., Morán-Tejeda, E., Sexstone, G.A., 2015. Snowpack variability across various spatio-temporal resolutions. *Hydrological Processes* 29 (6), 1213–1224.
- Lowe, D.G., 2004. Distinctive Image Features from Scale-Invariant Keypoints. *International Journal of Computer Vision* 60 (2), 91–110.
- Luetschg, M., Haeberli, W., 2007. Permafrost evolution in the Swiss Alps in a changing climate and the role of the snow cover. *Norsk Geografisk Tidsskrift - Norwegian Journal of Geography* 59 (2), 78–83.
- Magri, L., Toldo, R., 2017. Bending the doming effect in structure from motion reconstructions through bundle adjustment. *ISPRS - International Archives of the Photogrammetry, Remote Sensing and Spatial Information Sciences XLII-2/W6*, 235–241.
- Marti, R., Gascoin, S., Berthier, E., Pinel, M. de, Houet, T., Laffly, D., 2016. Mapping snow depth in open alpine terrain from stereo satellite imagery. *The Cryosphere* 10 (4), 1361–1380.
- Matsuura, S., Asano, S., Okamoto, T., Takeuchi, Y., 2003. Characteristics of the displacement of a landslide with shallow sliding surface in a heavy snow district of Japan. *Engineering Geology* 69 (1-2), 15–35.

- Michele, C. de, Avanzi, F., Passoni, D., Barzaghi, R., Pinto, L., Dosso, P., Ghezzi, A., Gianatti, R., Della Vedova, G., 2016. Using a fixed-wing UAS to map snow depth distribution. An evaluation at peak accumulation. *The Cryosphere* 10 (2), 511–522.
- Micheletti, N., Chandler, J.H., Lane, S.N., 2015a. Investigating the geomorphological potential of freely available and accessible structure-from-motion photogrammetry using a smartphone. *Earth Surface Processes and Landforms* 40 (4), 473–486.
- Micheletti, N., Chandler, J.H., Lane, S.N., 2015b. Structure from motion (SfM) photogrammetry. In: Clark, L.E., Nield, J.M. (Eds.), *Geomorphological Techniques*, Online Edition. British Society for Geomorphology, London.
- Middelkoop, H., Daamen, K., Gellens, D., Grabs, W., Kwadijk, J.C.J., Lang, H., Parmet, B.W.A.H., Schädler, B., Schulla, J., Wilke, K., 2001. Impact of Climate Change on Hydrological Regimes and Water Resources Management in the Rhine Basin. *Climatic Change* 49 (1/2), 105–128.
- Moreels, P., Perona, P., 2007. Evaluation of Features Detectors and Descriptors based on 3D Objects. *International Journal of Computer Vision* 73 (3), 263–284.
- Mote, P.W., Hamlet, A.F., Clark, M.P., Lettenmaier, D.P., 2005. Declining mountain snowpack in western North America. *Bulletin of the American Meteorological Society* 86 (1), 39–49.
- Niederheiser, R., Mokroš, M., Lange, J., Petschko, H., Prasicek, G., Elberink, S.O., 2016. Deriving 3D point clouds from terrestrial photographs - comparison of different sensors and software. *ISPRS - International Archives of the Photogrammetry, Remote Sensing and Spatial Information Sciences* XLI-B5, 685–692.
- Nolan, M., Larsen, C., Sturm, M., 2015. Mapping snow depth from manned aircraft on landscape scales at centimeter resolution using structure-from-motion photogrammetry. *The Cryosphere* 9 (4), 1445–1463.
- Nuth, C., Kääb, A., 2011. Co-registration and bias corrections of satellite elevation data sets for quantifying glacier thickness change. *The Cryosphere* 5 (1), 271–290.
- Okamoto, T., Matsuura, S., Larsen, J.O., Asano, S., Abe, K., 2018. The response of pore water pressure to snow accumulation on a low-permeability clay landslide. *Engineering Geology* 242, 130–141.
- Oliensis, J., 2000. A Critique of Structure-from-Motion Algorithms. *Computer Vision and Image Understanding* 80 (2), 172–214.
- Ouédraogo, M.M., Degré, A., Debouche, C., Lisein, J., 2014. The evaluation of unmanned aerial system-based photogrammetry and terrestrial laser scanning to generate DEMs of agricultural watersheds. *Geomorphology* 214, 339–355.
- Painter, T.H., Berisford, D.F., Boardman, J.W., Bormann, K.J., Deems, J.S., Gehrke, F., Hedrick, A., Joyce, M., Laidlaw, R., Marks, D., Mattmann, C., McGurk, B., Ramirez, P., Richardson, M., Skiles, S.M., Seidel, F.C., Winstral, A., 2016. The Airborne Snow Observatory. Fusion of scanning lidar, imaging spectrometer, and physically-based modeling for mapping snow water equivalent and snow albedo. *Remote Sensing of Environment* 184, 139–152.
- Palacios, D., Sánchez-Colomer, M.G., 1997. The distribution of high mountain vegetation in relation to snow cover: Peñalara Spain. *CATENA* 30 (1), 1–40.
- Passalacqua, P., Belmont, P., Staley, D.M., Simley, J.D., Arrowsmith, J.R., Bode, C.A., Crosby, C., DeLong, S.B., Glenn, N.F., Kelly, S.A., Lague, D., Sangireddy, H., Schaffrath, K., Tarboton, D.G., Wasklewicz, T., Wheaton, J.M., 2015. Analyzing high resolution topography for advancing the understanding of mass and energy transfer through landscapes. A review. *Earth-Science Reviews* 148, 174–193.
- Piermattei, L., Carturan, L., Blasi, F. de, Tarolli, P., Dalla Fontana, G., Vettore, A., Pfeifer, N., 2016. Suitability of ground-based SfM? MVS for monitoring glacial and periglacial processes. *Earth Surface Dynamics* 4 (2), 425–443.
- Prokop, A., 2008. Assessing the applicability of terrestrial laser scanning for spatial snow depth measurements. *Cold Regions Science and Technology* 54 (3), 155–163.
- Rabatel, A., Sanchez, O., Vincent, C., Six, D., 2018. Estimation of glacier thickness from surface mass balance and ice flow velocities: a case study on Argentière Glacier, France. *Frontiers in Earth Science*, 6, 112.

- Revuelto, J., Vionnet, V., López-Moreno, J.-I., Lafaysse, M., Morin, S., 2016. Combining snowpack modeling and terrestrial laser scanner observations improves the simulation of small scale snow dynamics. *Journal of Hydrology* 533, 291–307.
- Robertson, D.P., Cipolla, R., 2009. Structure from motion. In: Varga, M. (Ed.), *Practical Image Processing and Computer Vision*. John Wiley & Sons, Ltd, New York.
- Rosnell, T., Honkavaara, E., 2012. Point cloud generation from aerial image data acquired by a quadcopter type micro unmanned aerial vehicle and a digital still camera. *Sensors (Basel, Switzerland)* 12 (1), 453–480.
- Rossini, M., Di Mauro, B., Garzonio, R., Baccolo, G., Cavallini, G., Mattavelli, M., Amicis, M. de, Colombo, R., 2018. Rapid melting dynamics of an alpine glacier with repeated UAV photogrammetry. *Geomorphology* 304, 159–172.
- Rosten, E., Drummond, T., 2006. Machine Learning for High-Speed Corner Detection. In: Leonardis, A., Bischof, H., Pinz, A. (Eds.), *Computer vision - ECCV 2006. 9th European Conference on Computer Vision, Graz, Austria, May 7-13, 2006 : proceedings / Aleš Leonardis, Horst Bischof, Axel Pinz (eds.)*. Springer, Berlin, pp. 430–443.
- Rublee, E., Vincent, R., Konolige, K., Bradski, G., 2011. ORB: An efficient alternative to SIFT or SURF. *Proceedings of the IEEE International Conference on Computer Vision (ICCV), Barcelona, Spain, 2564–2571*.
- Rupnik, E., Daakir, M., Pierrot Deseilligny, M., 2017. MicMac – a free, open-source solution for photogrammetry. *Open Geospatial Data, Software and Standards* 2 (1), 1-9.
- Sailer, R., Rutzinger, M., Rieg, L., Wichmann, V., 2014. Digital elevation models derived from airborne laser scanning point clouds. Appropriate spatial resolutions for multi-temporal characterization and quantification of geomorphological processes. *Earth Surface Processes and Landforms* 39 (2), 272–284.
- Schaffhauser, A., Adams, M., Fromm, R., Jörg, P., Luzi, G., Noferini, L., Sailer, R., 2008. Remote sensing based retrieval of snow cover properties. *Cold Regions Science and Technology* 54 (3), 164–175.
- Schaffrath, K.R., Belmont, P., Wheaton, J.M., 2015. Landscape-scale geomorphic change detection. Quantifying spatially variable uncertainty and circumventing legacy data issues. *Geomorphology* 250, 334–348.
- Schirmer, M., Lehning, M., 2011. Persistence in intra-annual snow depth distribution: 2. Fractal analysis of snow depth development. *Water Resources Research* 47 (9), 2373.
- Schöber, J., Schneider, K., Helfricht, K., Schattan, P., Achleitner, S., Schöberl, F., Kirnbauer, R., 2014. Snow cover characteristics in a glacierized catchment in the Tyrolean Alps - Improved spatially distributed modelling by usage of Lidar data. *Journal of Hydrology* 519, 3492–3510.
- Seitz, S. M., Curless, B., Diebel, J., Scharstein, D., Szeliski, R., 2006. A comparison and evaluation of multi-view stereo reconstruction algorithms. In 2006 IEEE computer society conference on computer vision and pattern recognition (CVPR'06) (Vol. 1, pp. 519-528). IEEE.
- Seitz, S.M., Dyer, C.R., 1999. Photorealistic Scene Reconstruction by Voxel Coloring. *International Journal of Computer Vision* 35 (2), 151–173.
- Smith, M.W., Carrivick, J.L., Quincey, D.J., 2015. Structure from motion photogrammetry in physical geography. *Progress in Physical Geography* 40 (2), 247–275.
- Smith, M.W., Vericat, D., 2015. From experimental plots to experimental landscapes. Topography, erosion and deposition in sub-humid badlands from Structure-from-Motion photogrammetry. *Earth Surface Processes and Landforms* 40 (12), 1656–1671.
- Snively, N., 2008. Scene reconstruction and visualization from Internet photo collections. Unpublished PhD Thesis, USA.
- Snively, N., Seitz, S.M., Szeliski, R., 2006. Photo tourism: exploring photo collections in 3D. *ACM Transactions on Graphics* 25 (3), 835.
- Snively, N., Seitz, S.M., Szeliski, R., 2008. Modeling the World from Internet Photo Collections. *International Journal of Computer Vision* 80 (2), 189–210.

- Sold, L., Huss, M., Hoelzle, M., Anderegg, H., Joerg, P.C., Zemp, M., 2013. Methodological approaches to infer end-of-winter snow distribution on alpine glaciers. *Journal of Glaciology* 59 (218), 1047–1059.
- Stumpf, A., Malet, J.-P., Allemand, P., Pierrot-Deseilligny, M., Skupinski, G., 2015. Ground-based multi-view photogrammetry for the monitoring of landslide deformation and erosion. *Geomorphology* 231, 130–145.
- Sturm, M., 2015. White water. Fifty years of snow research in WRR and the outlook for the future. *Water Resources Research* 51 (7), 4948–4965.
- Swift, D.A., Cook, S., Heckmann, T., Moore, J., Gärtner-Roer, I., Korup, O., 2015. Chapter 6 - Ice and Snow as Land-Forming Agents. In: Shroder, J.F., Haeberli, W., Whiteman, C. (Eds.), *Snow and Ice-Related Hazards, Risks and Disasters*. Academic Press, Boston, pp. 167–199.
- Szeliski, R., 1999. A multi-view approach to motion and stereo. *Proceedings. 1999 IEEE Computer Society Conference on Computer Vision and Pattern Recognition*, pp. 157–163.
- Tagliasacchi, A., Olson, M., Zhang, H., Hamarneh, G., Cohen-Or, D., 2011. VASE. Volume-Aware Surface Evolution for Surface Reconstruction from Incomplete Point Clouds. *Computer Graphics Forum* 30 (5), 1563–1571.
- Tedesco, M., Derksen, C., Deems, J.S., Foster, J.L., 2015. Remote sensing of snow depth and snow water equivalent. In: Tedesco, M. (Ed.), *Remote sensing of the cryosphere*. John Wiley & Sons, Ltd, New York.
- Tinkham, W.T., Smith, A.M.S., Marshall, H.-P., Link, T.E., Falkowski, M.J., Winstral, A.H., 2014. Quantifying spatial distribution of snow depth errors from LiDAR using Random Forest. *Remote Sensing of Environment* 141, 105–115.
- Tonkin, T., Midgley, N., 2016. Ground-Control Networks for Image Based Surface Reconstruction. An Investigation of Optimum Survey Designs Using UAV Derived Imagery and Structure-from-Motion Photogrammetry. *Remote Sensing* 8 (9), 786.
- Tonkin, T.N., Midgley, N.G., Graham, D.J., Labadz, J.C., 2014. The potential of small unmanned aircraft systems and structure-from-motion for topographic surveys. A test of emerging integrated approaches at Cwm Idwal, North Wales. *Geomorphology* 226, 35–43.
- Triggs, B., McLauchlan, P.F., Hartley, R.I., Fitzgibbon, A.W., 2000. Bundle Adjustment - a modern synthesis. In: Triggs, B., Zisserman, A., Szeliski, R. (Eds.), *Vision algorithms '99. Lecture notes in computer science*. Springer-Verlag, Berlin, Heidelberg., pp. 298–372.
- Turner, D., Lucieer, A., Wallace, L., 2014. Direct Georeferencing of Ultrahigh-Resolution UAV Imagery. *IEEE Transactions on Geoscience and Remote Sensing* 52 (5), 2738–2745.
- Vander Jagt, B., Lucieer, A., Wallace, L., Turner, D., Durand, M., 2015. Snow Depth Retrieval with UAS Using Photogrammetric Techniques. *Geosciences* 5 (3), 264–285.
- Verhoeven, G., 2011. Taking computer vision aloft - archaeological three-dimensional reconstructions from aerial photographs with photoscan. *Archaeological Prospection* 18 (1), 67–73.
- Walker, J.P., Willgoose, G.R., 1999. On the effect of digital elevation model accuracy on hydrology and geomorphology. *Water Resources Research* 35 (7), 2259–2268.
- Wallace, L., Lucieer, A., Malenovský, Z., Turner, D., Vopěnka, P., 2016. Assessment of Forest Structure Using Two UAV Techniques: A Comparison of Airborne Laser Scanning and Structure from Motion (SfM) Point Clouds. *Forests* 7 (12), 62.
- Wechsler, S.P., Kroll, C.N., 2006. Quantifying DEM Uncertainty and its Effect on Topographic Parameters. *Photogrammetric Engineering & Remote Sensing* 72 (9), 1081–1090.
- Westoby, M.J., Brasington, J., Glasser, N.F., Hambrey, M.J., Reynolds, J.M., 2012. 'Structure-from-Motion' photogrammetry. A low-cost, effective tool for geoscience applications. *Geomorphology* 179, 300–314.
- Wheaton, J.M., Brasington, J., Darby, S.E., Sear, D.A., 2010. Accounting for uncertainty in DEMs from repeat topographic surveys. Improved sediment budgets. *Earth Surface Processes and Landforms* 35, 136–156.
- Wilson, J.P., 2010. Digital terrain modeling. *Geomorphology* 137 (1), 107–121.

- Wyrick, J.R., Pasternack, G.B., 2016. Revealing the natural complexity of topographic change processes through repeat surveys and decision-tree classification. *Earth Surface Processes and Landforms* 41 (6), 723–737.
- Zhang, J., Boutin, M., Aliaga, D.G., 2006. Robust Bundle Adjustment for Structure from Motion. 2006 IEEE International Conference on Image Processing. IEEE, pp. 2185–2188.

Appendix

Detailed UAV flight and SFM-MVS processing information

Table 10. Summary of Agisoft PhotoScan processing settings

Image Processing Settings in Agisoft Photoscan (version 1.4.2)
Align photos
Accuracy: High
Key point limit: 40 000
Tie point limit: 4 000
Selected generic preselection, reference preselection, and adaptive camera model fitting
Reference settings
Coordinate system RGF93/Labert-93 + NGF-IGN69 height (EPSG::5698)
Camera accuracy: 10 m
Marker accuracy: 0.02 m
Markers
14-19 GCPs (RTK GNSS with positional accuracy ≤ 2 cm at 1σ)
Sparse point cloud filtering (using the General Selection tool)
Reconstruction uncertainty level: 10
Reprojection error: 0.5
Projection accuracy: 3.0
Optimize camera alignment
Selected Fit f, Fit cx, Fit cy, Fit k1, Fit k2, Fit b1, Fit b2, Fit p1, Fit p2
Build dense point cloud
Quality: High
Depth filtering: Mild

Table 11. Summary of survey details for October 5, 2017 (13 GCPs) and PhotoScan processing results

Scene	Time of acquisition	No. images	Average flying height (m)	Ground resolution (cm/pixel)	Coverage area (km²)	RMS reproj. error (pixels)	Vertical error from GCPs (cm)
Oct-1356	13:56	108	66.3	2.58	0.084	0.476	2.37
Oct-1407	14:07	92	67.9	2.64	0.078	0.472	3.22
Oct-1435	14:35	121	69.5	2.72	0.090	0.494	2.66
Oct-1446	14:46	111	66.2	2.59	0.085	0.458	2.82
Oct-1456	14:56	108	62.4	2.41	0.081	0.458	1.93
Oct-1525	15:25	114	65.3	2.55	0.085	0.442	3.87
Oct-1535	15:35	108	66.9	2.57	0.083	0.507	2.06

Table 12. Summary of survey details for June 2, 2017 (19 GCPs) and PhotoScan processing results

Scene	Time of acquisition	No. images	Average flying height (m)	Ground resolution (cm/pixel)	Coverage area (km²)	RMS reproj. error (pixels)	Vertical error from GCPs (cm)
Jun-1006	10:06	70	59.1	2.26	0.057	0.573	1.76
Jun-1015	10:15	74	59.6	2.23	0.058	0.527	2.48
Jun-1023	10:23	67	60.6	2.31	0.056	0.547	2.45
Jun-1038	10:38	77	59.5	2.26	0.061	0.558	2.08
Jun-1053	10:53	70	60.8	2.32	0.056	0.480	2.10
Jun-1104	11:04	76	61.6	2.34	0.061	0.699	1.97

Table 13. Summary of survey details for Feb 22, 2017 (15 GCPs) and PhotoScan processing results

Scene	Time of acquisition	No. images	Average flying height (m)	Ground resolution (cm/pixel)	Coverage area (km²)	RMS reproj. error (pixels)	Vertical error from GCPs (cm)
Feb-1357	13:57	68	60.2	2.33	0.056	0.446	0.49
Feb-1405	14:05	66	61.9	2.32	0.053	0.768	0.47
Feb-1411	14:11	68	63.4	2.41	0.057	0.737	0.69
Feb-1420	14:20	66	57.8	2.28	0.053	0.402	0.88
Feb-1428	14:28	68	59.7	2.27	0.053	0.801	0.54

Table 14. Summary of UAV survey conditions

February 22, 2017 conditions

- Cloud free
- Predominantly snow covered, some areas of exposed boulders and rock debris
- Strong texture in the snow, some of the scene marked by ski-tracks
- A couple of weeks since previous snowfall
- Air temperature from -1 to 6 C°.

June 2, 2017 conditions

- Partial snow cover
- Rainfall in the previous week leading up to the survey (1 + 6 + 11.8 + 7.2 + 4 + 8.6 mm on June 31, 30, 29, 28, 27, 26, 24), avg. daily temperature between 5 and 15 C°
- Air temperature from 2 to 10 C°
- Suncups present on snow surface

October 5, 2017 conditions

- Mainly sunny, sometimes with partial cloud cover
- Scene entirely snow free
- Air temperature from 7 to 16 C°
- Little precipitation in the previous week (< 5 mm)

Overview of digital elevation model registration settings

Table 15. Summary of bUnwarpJ processing settings using ImageJ for image registration

bUnwarpJ Plugin Processing Settings (version 2.6.8) – ImageJ (version 1.51u)

Source image: mean DEM 5-Oct-2017 from SFM-MVS using imagery from a UAV survey
Target image: resampled DEM 16-Aug 2012 from airborne lidar
Registration mode: Accurate

Advanced Options

- Initial Deformation: Fine
- Final Deformation: Super Fine
- Divergence Weight: 0.0
- Curl Weight: 0.0
- Landmark Weight: 1.0
- Image Weight: 1.0
- Consistency Weight: 10.0
- Stop Threshold: 0.01
